2016

Conjugate Heat Transfer Analysis of Combined Regenerative and Discrete Film Cooling in a Rocket Nozzle

Charlotte M. Pearce
University of Central Florida

Conjugate Heat Transfer Analysis of Combined Regenerative and Discrete Film Cooling in a Rocket Nozzle

by

Charlotte Mary Pearce

A thesis submitted in partial fulfillment of the requirements
for the Honors in the Major Program in Aerospace Engineering
in the College of Engineering and Computer Science
and in The Burnett Honors College
at the University of Central Florida
Orlando, Florida

Fall Term, 2016

Thesis Chair: Jayanta Kapat, Sc.D.

ABSTRACT

Conjugate heat transfer analysis has been carried out on an 89kN thrust chamber in order to evaluate whether combined discrete film cooling and regenerative cooling in a rocket nozzle is feasible. Several cooling configurations were tested against a baseline design of regenerative cooling only. New designs include combined cooling channels with one row of discrete film cooling holes near the throat of the nozzle, and turbulated cooling channels combined with a row of discrete film cooling holes. Blowing ratio and channel mass flow rate were both varied for each design. The effectiveness of each configuration was measured via the maximum hot gas-side nozzle wall temperature, which can be correlated to number of cycles to failure. A target maximum temperature of 613K was chosen. Combined film and regenerative cooling, when compared to the baseline regenerative cooling, reduced the hot gas side wall temperature from 667K to 638K. After adding turbulators to the cooling channels, combined film and regenerative cooling reduced the temperature to 592K. Analysis shows that combined regenerative and film cooling is feasible with significant consequences, however further improvements are possible with the use of turbulators in the regenerative cooling channels.

ACKNOWLEDGMENTS

I would like to thank my thesis chair, Dr. Jayanta Kapat, for enabling me to complete this thesis, as well as my committee members Dr. Kareem Ahmed, Dr. Ali Gordon, and Dr. Arvind Singh for their useful input during my defense.

Special thanks to Lucky Tran, a fantastic mentor who provided invaluable advice, good spirits, and constant encouragement to the process. I could not have succeeded without it.

Thank you to my parents for supporting me throughout my life, during my studies at university, and now. Finally, thank you to my partner, Steven Erickson, for his unfaltering support and encouragement throughout my years at university and during my experience researching and writing this thesis. Thank you.

TABLE OF CONTENTS

LIST OF FIGURES

LIST OF TABLES

INTRODUCTION

Rocketry in its modern form has its roots in the late 1800s and early 1900s. Since then, "rocket science" has grown tremendously. Since the 1950s, rocketry has allowed humankind to venture into space to explore, establish satellite technology, and facilitate impactful effects of orbital technology. From the International Space Station to the most recent ventures into satellite internet, rockets are an integral part of future technology, both within the Earth's atmosphere and beyond. Virtually all artificial satellites (and humans) have been placed into orbit via rockets. Without the abundant amount of thrust provided by extreme reactions contained within a rocket and rocket nozzle, orbital and deep space travel would not be feasible. Rockets have been, are, and will retain an integral role in space exploration.

In order to maintain the International Space Station, inject satellites into orbit, and explore further into space, increasing amounts of cargo-bearing rockets must launch every year. It is averaged that 90 missions are carried out into orbit throughout the world every year. One of the larger impacts to the cost of space travel is the lack of reusability of the rockets themselves. It is projected that the cost of each launch could be reduced by about 60 million USD with reusable rockets. Another important factor is America's need for self-sufficiency in orbital endeavors. Currently the USA has to spend a large amount of money on Russian crew vehicle seats for astronauts to get to the International Space Station. If this service was domesticated again via reusable US-based rockets, this cost could be drastically reduced. Another important factor impacting cost of missions out of Earth's atmosphere is engine

efficiency. Improving the efficiency of spacecraft would reduce the amount of fuel needed, thereby considerably reducing the cost and increasing the payload capacity.

Rockets generate an enormous amount of thrust through a nozzle in order to propel several thousand pounds of the vehicle with payload through and above the atmosphere. This thrust is generated using specified high-energy reactions that use fuel (such as rocket propellant or hydrogen) and an oxidizer (such as oxygen). Solid-fuel rocketry is used throughout the aerospace industry in ballistic missiles and orbital rockets such as the Atlas V and Delta IV boosters. The fuel and oxidizer are combined in a solid fuel and burn continuously for thrust, which means that the rocket is monopropellant. Liquid-propellant rocket engines have also been highly prevalent throughout the history of rocketry, from the first liquid propellant rocket designed by Goddard in 1921 and launched in 1926 [1], to the latest SpaceX Falcon 9 rocket in use today. Liquid-propellant rocket engines (LRPEs) may have separate fuel and oxidizer that are mixed in the thrust chamber inlet and burned, which means that they are bipropellant. The thrust chamber is the converging-diverging nozzle where the fuel is burned and thrust is produced from the combustion and acceleration of the flow through the converging-diverging nozzle. LPREs are favored for their versatility, increased control. Liquid fuels also may be cryogenic, which generate higher specific thrust.

LPREs can be divided into several groups depending on their engine cycle. Common engine cycles include the expander cycle and gas generator cycle. In an expander cycle, fuel and oxidizer are run through pumps to their respective destinations. All of the cryogenic fuel is routed through cooling channels that extend from the nozzle exhaust to the inlet of the nozzle,

which preheats the fuel and cools the thrust chamber. The fuel is then expanded through a turbine that powers the oxidizer and fuel pumps. This fuel is finally routed into the thrust chamber to be mixed with the oxidizer and burned. This particular type of expander cycle is called the closed expander cycle, since all of the fuel and oxidizer are used for thrust within the thrust chamber. The gas generator cycle is similar to the expander cycle in that fuel is used to both cool the nozzle and power the engine's pumps. However, there are a few differences. The gas generator cycle uses part of the fuel and oxidizer to burn in a pre-burner. This pre-burner is used to power the turbine that powers the fuel and oxidizer pumps. The resulting burnt fuel and oxidizer are then exhausted out of the turbine down the side of the nozzle. Since this exhaust is expelled and not used for combustion in the nozzle, this cycle is known as an open cycle. This exhaust from open cycles is potentially exhausted gas that could be used for film cooling.

The environment rocket nozzles are exposed to is harsh and extreme. In order to achieve optimal efficiency with the rocket engine, fuel combustion must be completed at the highest temperatures possible (at or near the stoichiometric fuel-to-oxidizer ratio). During combustion, a rocket nozzle can be exposed to temperatures over 3700K, and pressures averaging up to 20MPa. In order to maintain the structural integrity of the nozzle, the structures themselves must be protected from the abundant amount of stresses they are exposed to during launch and reentry. Thermal strain is a significant factor in determining the life of the nozzle. Thermal stresses are caused by the overall change in temperature over a length—in this case, a nozzle wall—and are characterized by expansion and contraction across

the material due to changes in nozzle temperature from operating conditions. If thermal stresses are too great, the nozzle can fracture and fail. In order to alleviate these severe thermal stresses and strains on the rocket nozzle structure, increasingly high-performance materials must be utilized to withstand the extreme temperatures. However, the most commonly used materials for rocket thrust chambers (copper & nickel alloys) have melting points that are well below the combustion temperature. Since materials alone cannot compensate for the extreme conditions, internal and external cooling methods must be utilized. Cooling the nozzle will prevent the nozzle melting, which is critical during the high temperatures and pressures of launch: if the nozzle fails, catastrophic results follow that can involve lives as well as payloads. If the nozzle is significantly damaged, it will hinder the efforts of supplying reusable rocket nozzles.

Internal cooling was first demonstrated in the United States in 1938 by James H. Wyld, an amateur rocketeer and one of the founders of ReactionMotors, Inc. (RMI) [1]. Currently, most rocket nozzles are still cooled using internal regenerative cooling, where coolant is run through channels that span the circumference of the nozzle, cooling the nozzle from the "backside". This type of internal cooling is called regenerative cooling since the coolant is eventually used in the pre-burner or thrust chamber. For example, the Space Shuttle Program used internal cooling to cool the nozzles on the reusable shuttle spacecraft component.

One of the other solutions to cool a surface but maintain a high chamber temperature is film cooling. Film cooling through discrete holes is rare in the thrust chamber of a rocket nozzle: most rockets, if using film cooling, will utilize slot film cooling at the injector, not discrete film

holes further downstream of the flow. Slot film cooling uses slots tangential to the flow to inject coolant (normally fuel or oxidizer such as hydrogen or oxygen in rocket engines) tangent to the flow. With discrete film cooling, small holes feed coolant through the nozzle wall and inject it into the hot gas at a specified angle with the wall. This creates a thermal and species boundary layer between the hot gases and the nozzle wall, shielding the wall surface while maintaining the heat within the freestream flow.

Internal cooling can cause a large thermal gradient from the hot gas side wall to the outer wall of the nozzle. This large change in temperature causes the materials to expand nearer the hot gas and contract nearer the top of internal cooling channels and the outer nozzle wall. This phenomenon can be characterized by thermal stress, which can impact the integrity and life of the nozzle itself. Minimizing thermal strain while also maximizing cooling effectiveness is a constant battle with nozzle optimization. Film cooling can help relieve some thermal strain while still providing optimal cooling.

Combining both internal and film cooling has been a subject of investigation since early on in this research field [2]. However, there has been little research analysis into the effect of combining these cooling methods in a rocket nozzle and how the thrust chamber environment affects the cooling effectiveness. Both internal and film cooling have proved its worth in rocket nozzle cooling, but further verification of currently accepted trends for a combination of the two is needed, particularly numerical verification of experimental results.

Literature Review

A comprehensive analysis of the current state of the industry of rocket nozzle geometry and film cooling is needed in order to better understand the system itself, as well as the problem it is solving.

Rocket Nozzle Contour

Rocket nozzle design has evolved over the past 100 years. Originally, most nozzles used in the military and on sounding rockets were conical, meaning that their rate of wall divergence was linear. The divergent cone half angle was normally set between 12° and 18 °, with the most common angle being 15°. This configuration was relatively simple to manufacture, provided a good balance of performance and weight, and so was suitable for the early stages of rocketry. As research progressed, nozzle designs increased in complexity. Contour, or bell, nozzles were designed in order to better direct flow axially through the nozzle exit. Bell nozzles consist of two sections with different diverging angles: large near the throat, and small near the nozzle exit [3]. Original designs based solely on optimization, however were too long for practical use due to the weight and difficulty in making a structurally sound long nozzle. Rocket engineers opted for shorter bell nozzles instead, the contour and length of which was optimized by Rao in 1958 [4]. After development in the 1960s, bell nozzles have become one of the most popular nozzle designs to use [5].

As a rocket gains altitude, the optimum nozzle design changes due to changes in ambient pressure. Today, multistage rockets and nozzle extensions are the methods of "altitude-compensation." There are also several conceptual designs of rocket nozzles in

development that are altitude-compensating via their geometry alone. Annular nozzles, such as the aerospike nozzle and plug nozzle, maintain the same thrust results as conventional nozzles, but do not require the throat flow to be parallel to the axis of the rocket's thrust and velocity. Annular nozzles are currently under research and prototyping.

It addition to their long lengths, it is difficult to optimize a nozzle for all altitudes because flow separation generally occurs at one of the extremes in a conventional bell nozzle. That is, bell nozzles optimized for high altitude flight incur flow separation at low altitudes and vice-versa. Even more critical however, is the transient startup and shutdown process where, inevitably all rocket nozzles will incur flow separation in the supersonic part of the nozzle [6]. Unsteady flow separation can lead to nozzle side loads, which are detrimental to flight stability.

Dual-bell nozzles are another conceptual design for an altitude-compensating nozzle, using a complex geometry to allow for optimal thrust at both low and high altitudes. The dual-bell nozzle concept is actively being pursued in European space agencies, notably DLR [7-15]. In a conventional bell nozzle with a nozzle extension, there is an abrupt wall inflection angle at the connection. The design of the dual-bell nozzle aims to optimize the inflection such that flow separation can be carefully controlled without needing any moving parts (the nozzle extension is a moving part because it is deployed during flight). At low altitudes, flow separation reduces the effective area of the nozzle so that it behaves as a nozzle with a lower expansion ratio, increasing the low-altitude thrust (compared to nozzles with that have too large an area ratio). At high altitudes, the flow attaches to the nozzle, entering the high altitude mode of operation. The flow reattachment allows the full area ratio to be used, allowing the thrust to be optimized

for high altitude while maintaining operability at low altitudes [14]. These types of nozzle designs eliminate thrust losses at low altitudes, however they require much more sophisticated cooling, and are difficult to manufacture due to their complexity [4]. This added complexity (and associated cost) can be compensated for with the resulting increased reusability.

Fuel Injector Dynamics

Most liquid propellant rocket engines use a fuel injector in order to inject the fuel and oxidizer into the combustion chamber so that they are well mixed in a uniform manner. An injector normally uses a porous baseplate. In rockets using hydrogen and oxygen, gaseous hydrogen flows through the porous baseplate in order to cool the baseplate via transpiration cooling and protect it from the hot combustion gases. The RL10 specifically uses a conical shaped injector for mixing hydrogen and oxygen. The injector used by Wadel et al. [16] had 91 LOX posts, while the injector used by Quentmeyer in his experimental low-cycle fatigue investigations had 70 LOX posts [17]. The RL10 itself has 614 [18]. The injector atomizes the gaseous fuel and liquid oxidizer, and allows for mixing of both [19]. Some numerical studies will assume that the injector dynamics can be predicted based on empirical calculations, thereby simplifying the simulation and calculations [16]. However, this assumption is an oversimplification [20]. In their analysis of liquid propellant injectors, Bazarov and Yang [21] surmised that injectors produce mixtures that can be highly varied both radially and from use to use. Therefore, it is imperative to model a nozzle with and without an injector in a three-dimensional environment in order to determine how much of the combustion process is affected by this variation.

Complex Chemistry

Additionally, in order to correctly model the combustion process in a rocket nozzle so that accurate hot gas temperatures are present, it is imperative to model the complex chemistry associated with the combustion process. Burke et al. [22] published an updated model for H_2/O_2 reactions that takes into account both experimental data and numerical simulations. The kinetic model is an updated version of the analysis completed by Li et al. in 2004 [23]. Burke's model contains 19 reactions in the process and 11 species. The kinetic mechanism and coefficients are tabulated in Table 1 and thermodynamic properties in Table 2.

Table 1: H_2/O_2 Reaction Model [22]

			A	*n*	E_a
(1)	$H + O_2 = O + OH$		1.04E+14	0.00	1.5286E+04
(2)	$O + H_2 = H + OH$	Duplicate	3.818E+12	0.00	7.948E+03
		Duplicate	8.792E+14	0.00	1.917E+04
(3)	$H_2 + OH = H_2O + H$		0.216E+09	1.51	0.343E+04
(4)	$OH + OH = O + H_2O$		3.34E+04	2.42	-1.93E+03
(5)	$H_2 + M = H + H + M$		4.577E+19	-1.40	1.0438E+05
	$\varepsilon_{H_2} = 2.5, \varepsilon_{H_2O} = 12$			-1.10	
(6)	$O + O + M = O_2 + M$		6.165E+15	-0.50	0.000E+00
	$\varepsilon_{H_2} = 2.5, \varepsilon_{H_2O} = 12$				
(7)	$O + H + M = OH + M$		4.714E+18	-1.00	0.000E+00
	$\varepsilon_{H_2} = 2.5, \varepsilon_{H_2O} = 12$				
(8)	$H_2O + M = H + OH + M$		6.064E+27	-3.32	1.2079E+05
	$\varepsilon_{H_2} = 3.0, \varepsilon_{H_2O} = 0, \varepsilon_{O_2} = 1.5$				
	$H_2O + H_2O = H + OH + H_2O$		1.006E+26	-2.44	1.2018E+05
(9)	$H + O_2 (+M) = HO_2 + M$	k_∞	4.65084E+12	0.44	0.000E+00
		k_0	6.366E+20	-1.72	5.248E+02
	$F_c = 0.50, T^{***}$ =1.0E-30, T^* =1.0E+30				
	$\varepsilon_{H_2} = 2, \varepsilon_{H_2O} = 14$				
(10)	$HO_2 + H = H_2 + O_2$		2.750E+06	2.09	-1.451E+03
(11)	$HO_2 + H = OH + OH$		7.079E+13	0.00	2.950E+02
(12)	$HO_2 + O = O_2 + OH$		2.850E+10	1.00	-7.2393E+02
(13)	$HO_2 + OH = H_2O + O_2$		2.890E+13	0.00	-4.970E+02
(14)	$HO_2 + HO_2 = H_2O_2 + O_2$	Duplicate	4.200E+14	0.00	1.1982E+04
	$HO_2 + HO_2 = H_2O_2 + O_2$	Duplicate	1.300E+11	0.00	-1.6293E+03
(15)	$H_2O_2 + M = OH + OH + M$	k_∞		0.90	
		k_0		-2.30	
	$F_c = 0.42, T^{***}$ =1.0E-30, T^* =1.0E+30				
	$\varepsilon_{H_2O} = 7.5, \varepsilon_{H_2O_2} = 7.7, \varepsilon_{O_2} = 1.2,$ $\varepsilon_{H_2} = 3.7$				
(16)	$H_2O_2 + H = H_2O + OH$		2.410E+13	0.00	3.970E+03
(17)	$H_2O_2 + H = HO_2 + H_2$		4.820E+13	000	7.95E+03
(18)	$H_2O_2 + O = OH + HO_2$		9.55E+06	2.00	3.970E+03
(19)	$H_2O_2 + OH = HO_2 + H_2O$	Duplicate	1.740E+12	0.00	3.180E+02
		Duplicate	7.590E+13	0.00	7.270E+03
	Units are cm^3 mol s cal K;				
	$k = AT^n exp(-E_a/RT)$				

Table 2: ΔH_f and C_p (T) for Species in the H_2/O_2 Reaction [22]

Species	ΔH_f	S(298.15)	C_p(300)	C_p(5400)	C_p(800)	C_p(1000)	C_p(1500)	C_p(2000)
H	52.10	27.39	4.97	4.97	4.97	4.97	4.97	4.97
O	59.56	38.47	5.23	5.08	5.02	5.00	4.98	4.98
OH	8.91	43.91	7.16	7.05	7.15	7.34	7.87	8.28
H_2	0.00	31.21	6.90	7.00	7.07	7.21	7.73	8.18
O_2	0.00	49.01	7.01	7.44	8.07	8.35	8.72	9.03
H_2O	-57.80	45.10	8.00	8.45	9.22	9.87	11.26	12.22
HO_2	3.00	54.76	8.35	9.47	10.77	11.38	12.48	13.32
H_2O_2	-32.53	55.66	10.42	12.35	14.29	15.21	16.85	17.88
N_2	0.00	45.77	6.95	7.08	7.50	7.83	8.32	8.60
Ar	0.00	36.98	4.97	4.97	4.97	4.97	4.97	4.97
He	0.00	30.12	4.97	4.97	4.97	4.97	4.97	4.97

For computational time preservation, some authors simplify this reaction by omitting some of the species with near-negligible mass fractions from the inlet. In their analysis of slot film cooling in a rocket nozzle, Amato et al. [24] used a kinetic model that included H, H_2, OH, O_2, and H_2O as the stagnation inlet specifications, omitting O, HO_2, H_2O_2, N_2, Ar, and He. Each species requires additional computational time: up to seven equations have to be solved per species.

Internal Cooling

Internal cooling, also known as regenerative cooling, is regarded as the conventional method of cooling a rocket nozzle. Developed in the early 1900s and used by both Goddard and Wyld, regenerative cooling has a longstanding history with liquid-propellant rocket engines [1]. Internal cooling is advantageous because of the negligible combustion efficiency loss due to cooling, lightweight rocket structure, and the capability of long run times [25]. Internal cooling is the process of running cryogenic fuel through thin-walled tubes within the nozzle itself in order to cool the nozzle. The flow enters the channels at the exit of the nozzle. The fuel is then redirected back into the combustion process and used for combustion. Prediction equations for the heat-transfer coefficients in internal cooling channels have been verified, using existing data and deemed acceptable [26]. It is accepted that using liquid oxygen or hydrogen as the coolant achieves the best heat transfer coefficient results [27].

Wadel et al. [1998] investigated the effects of high-aspect ratio cooling channels (HARCC) in a rocket nozzle. They tested 7 designs for HARCC and compared it with a baseline design that does not use HARCC. One of these designs uses bifurcated channels at the throat. Bifurcated channels are designed by splitting the previous channel into two thinner channels in order to better distribute and increase heat transfer. Two of the designs use stepped channels, which increase heat transfer effectiveness using the fin effect. The aspect ratio (AR) and number/type of channels were varied for each design. These designs were compared in order to find an optimized HARCC configuration. The baseline geometry included an aspect ratio of 2.5 and a cooling channel configuration of 100 channels with no bifurcation. Each design was

created with two versions: one that accounts for fabrication and one that does not. The designs that account for fabrication normally have a slightly lower aspect ratio than the designs that do not account for fabrication due to manufacturing constraints. The designs were proposed for an 89kN thrust rocket combustion chamber, the contour of which originated at NASA Lewis Research Center. This contour is the basis of the RL10 rocket engine. The seven designs studied by Wadel et al. are given in Table 3. Note that the shaded cells indicate HARCC designs.

Table 3: Wadel et al. Cooling Channel Design Configurations

Channel Shape	Number of Coolant Channels			Design Number
	Chamber Region	Throat Region	Nozzle Region	
Continuous	100	100	100	1
	200	200	200	2
	100	100	100	3
	200	200	200	4
Bifurcated	100	200	100	5
Stepped	100	100	100	6
	200	200	200	7

The performance of the designs was evaluated by measuring the hot gas side wall temperature and finding the maximum hot gas side wall temperature (Tgw) in the nozzle. Pressure drop was also taken into account. Wadel et al. referenced Quentmeyer and his correlation for low-cycle fatigue and maximum Tgw, which will be discussed in detail later on.

Their aim was to reduce the Tgw from 778 to 667K, or by 200°R. It was asserted that this temperature reduction could double the life of the nozzle.

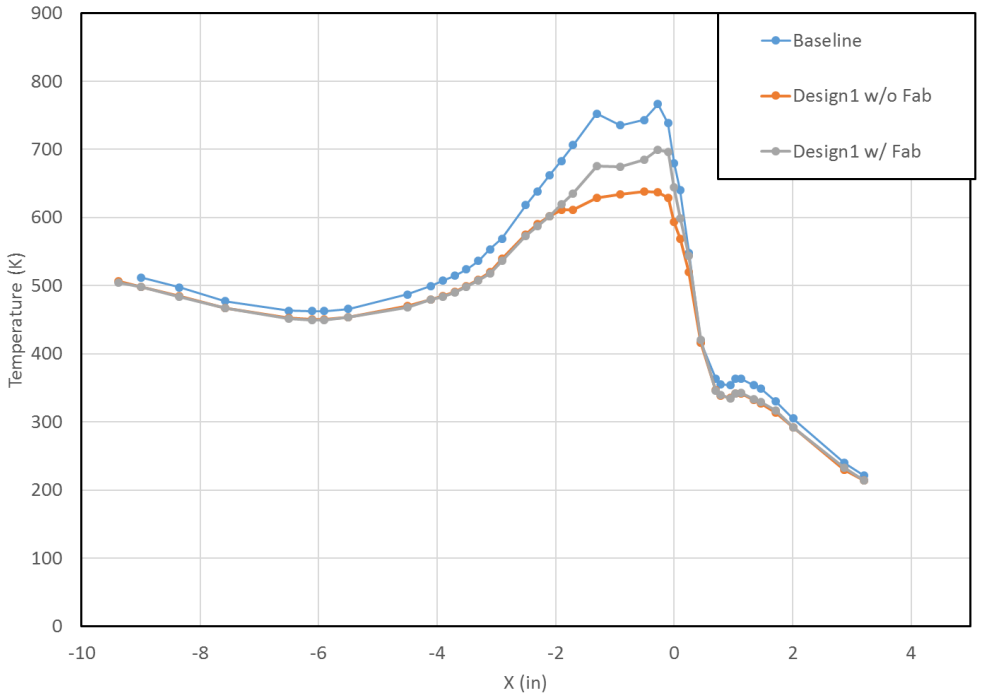

Figure 1: Temperature distribution of Baseline and Design 1 both with and without Fabrication – Wadel et al. [16]

Coolant flowed in the channels at an inlet temperature of 44.4K with a mass flow rate that was varied from 2.3 to 1.15kg/s. The baseline mass flow rate was 2.3kg/s. The propellant entered the thrust chamber with a GH_2 temperature of 300K and a LOX temperature of 91.7K.

It was found that an aspect ratio of 5 with a 100 to 200 to 100 bifurcated channel configuration (Design 5) reduced the hot gas side temperature by 18%. Using high aspect-ratio channels only in the throat region had a negligible difference in hot gas-side wall temperature compared to high-AR channels throughout, however a lower pressure-drop was observed for the former [16], [28].

While internal cooling can adequately cool a nozzle, there are limitations to the technology that can be improved upon. Internal cooling performance relies on the power of the pump that is supplying the coolant. The cooling effectiveness is heavily dependent on mass flow rate of the coolant. However, pumping power increases drastically with mass flow rate: the relationship between pumping power and mass flow rate is cubic in nature. Therefore, it is important to be able to optimize cooling so that pumping power is not excessive. Film cooling can alleviate this issue by diverting some of the cooling to an external manifold powered separately.

Thermal Barrier Coatings

In order to better withstand the intense temperatures experienced in the rocket thrust chamber, the nozzle wall itself can be modified. Materials can be improved by applying various coatings. Applying certain coatings to the nozzle hot gas-side wall can improve the material's resilience to high temperatures. For example, ceramic coatings such as zirconium-oxide can be plasma sprayed onto combustion side of cooled nozzle. The coatings can withstand much higher temperatures than common nozzle wall materials, such as copper. These coatings are normally called thermal barrier coatings (TBC), since their primary use is for protection against high temperatures. Coatings are thin and normally similar in thickness to the diameter of film holes, or from 0.5mm to 2mm thick [29]. Thermal barrier coatings are used in both turbomachinery and rocketry. Quentmeyer et al. [30] assessed the effects of thermal barrier coatings on the life of rocket nozzles. They found that, with a thermal barrier coating applied,

the hot gas-side wall temperature was reduced significantly. Maximum hot gas-side wall temperature can be correlated with nozzle life, and will be discussed in depth later.

The effects of thermal barrier coatings are not included in this work. Numerically modelling thermal barrier coatings is generally straightforward and reduced-order models are generally well suited to capturing their effects. They can be modelled analytically as surface contact resistances or by reducing the effective heat transfer coefficient. They can also be modelled as a thin solid shell on the surface. Lateral heat conduction effects may even be included in the shell conduction, and more accurate temperature distributions along the thickness of the coating can be obtained by increasing the number of shells. TBC's can also be included explicitly in the model and treated in the same way as other solid, although this approach is rare since the TBC is usually thin compared to the geometry where it is applied.

For uncooled nozzles, coatings are also used to improve ablative cooling performance by applying a coating that absorbs a significant amount of heat as it vaporizes.

Transpiration Cooling

Transpiration cooling is a cooling method that uses a porous material to inject coolant. For a rocket nozzle, the porous material would be the nozzle liner acting as the hot gas-side wall. Transpiration cooling creates a film along the wall from the coolant itself, while the interaction between the coolant and the porous material also increases heat transfer effectiveness by transferring heat into the coolant from the material. Transpiration cooling, if implemented appropriately, could require a smaller pump to inject the coolant when compared to regenerative cooling, thereby reducing the weight of the engine. This combination of effects

make transpiration cooling especially useful. Bucchi et al. [31] investigated the effects of transpiration cooling in a LPRE that uses liquid oxygen and methane. In varying liner porosity, conductivity, and coolant temperature, Bucchi et al. modelled a transpiration cooling configuration and found that, when using transpiration cooling in a rocket nozzle, hot gas-side wall temperature can be reduced significantly while maintaining a low pressure drop since high-speed coolant flow is not needed. It is important to note that a rocket nozzle design using transpiration cooling would require an entirely new nozzle liner that is manufactured using a porous material. The porous material could be concentrated at areas of high hot gas-side wall temperature, such as the throat of the nozzle.

Film Cooling

Film cooling has been a subject of research since the 1960s, and is regarded as one of the more effective and proven methods of cooling. It was originally used in nozzles that were for military purposes. The first film-cooled rocket used in a large capacity was the V-2 rocket, fired in World War II by Germany [1]. Later, film cooling in rocketry extended into the space industry. There are several ways one can configure film cooling, including altering the number of film cooling holes, injection angle, flow direction, and flow speed.

With discrete film cooling, coolant is fed through holes and injected into the mainstream flow. This film creates a thermal and species boundary layer along the surface of the wall exposed to the hot mainstream flow. The coolant can be injected at a number of angles with respect to the wall. Film cooling can be characterized by the following equation for momentum flux, Eqn. (1):

$$I = \frac{\rho u^2}{\rho_\infty u_\infty^2} \quad (1)$$

Where ρ and u are the density and velocity of the film, respectively, and ρ_∞ and u_∞ are the density and velocity of the mainstream flow, respectively. This equation helps to characterize how the film will inject into the freestream flow as well as the ratio between the flow rates of the film relative to the flow rate of the mainstream flow. This equation can also be written using both blowing ratio, Eqn. (2), and density ratio, Eqn. (3).

$$BR = \frac{\rho u}{\rho_\infty u_\infty} \quad (2)$$

$$DR = \frac{\rho}{\rho_\infty} \quad (3)$$

In order to achieve maximum effectiveness, it is important to be able to achieve the highest momentum flux ratio possible without flow separation from the wall.

Distributed film cooling is the utilization of multiple injection holes for cooling, and is beneficial because it prevents crossflow (which can reduce cooling effectiveness), it is possible to use within a wide range of materials, its effectiveness is similar to transpiration cooling, and has a structurally superior configuration [32].

Injection angle affects the direction of the flow. Injection angles are most commonly between 90 degrees (normal to the wall) and 30 degrees (inclined towards the exit of the mainstream flow). A foundational study in 1968 looked at the differences between a normal injection angle vs an injection angle of 35 degrees at varying mass flow ratios [33]. It was found that both the injection methods created the same spreading angle in the mainstream flow for

the lowest mass flow ratio, but at higher mass flow ratios, the normal injection spreading increases. This shows that an injection angle of 90 degrees covers a larger lateral area in high mass flow rates as opposed to the 35 degree injection angle[2], potentially increasing film cooling effectiveness, but also decreasing engine efficiency due to mixing phenomena.

It is possible to angle the film cooling holes toward the flow entrance rather than toward the exit, called backward or reverse injection, although it is not particularly common. A study by Park et al. [2015] showed that, using backward injection, both film cooling effectiveness and lateral cooling uniformity could be enhanced. An arrangement of film cooling holes both backward and forward in alternating rows was shown to be the best configuration. However, with reverse film cooling holes, there is evidence of reduced engine efficiency due to the coolant mixing with the mainstream flow [34]. Most film cooling arrays use forward-direction film cooling holes due to this factor.

There are numerous studies on film cooling by itself, both in subsonic and supersonic environments. Taylor [1968] illustrated that the correct correlation equations to use in order to calculate heat transfer coefficients in nozzle cooling are the same as the equations used to calculate this in straight and curved tubes [26]. Goldstein et al. [1968] conducted several experiments with film cooling, including studies regarding supersonic film cooling. They found that low speed film cooling characteristics could be applied to high speed, or supersonic, film cooling performance. This meant that the reference state for compressible flow was in agreement with the results found with incompressible flow, simplifying the correlations in high speed flow [35].

Film Cooling in a Nozzle

Within rocket nozzles, film cooling has been regarded as one of the more popular methods of cooling, apart from internal cooling, which is regenerative cooling channels along the circumference of the nozzle. However, subsonic film injected into the supersonic crossflow of rocket nozzles is a more modern field. Supersonic flow occurs after the nozzle throat in the nozzle extension. While rockets have been achieving supersonic speeds for some time, research into the environment and effects is more limited. Recently an empirical correlation of film cooling efficiency was calculated by Hombsch and Olivier [2013] for supersonic film cooling in a rocket nozzle [36]. This can be very useful, as it depicts the performance and behavior of film cooling in this environment, which allows engineers to more accurately design nozzle cooling configurations for maximum efficiency. These correlations need to be repeatedly tested both numerically and experimentally, however, in order to verify their accuracy. In this thesis, however, there is no supersonic flow present near the proposed film cooling location. There is little to no research on film cooling the thrust chamber itself with film cooling rather than the nozzle extension, and so this needs to be investigated further.

Film cooling correlations normally assume that velocity is constant/flow acceleration is zero. However, there was some skepticism that this assumption is applicable in a combustion chamber due to the dynamic effects observed. Arnold et al. [2009] studied the accuracy of film cooling effectiveness in a rocket nozzle using correlations for both constant flow and accelerating flow. Arnold et al. measured effectiveness with an effectiveness correlation for both non-accelerating and accelerating flow and compared the results. It was found that, while

close to the film hole, effectiveness for both types of flow matched up quite well. The effectiveness difference increased far downstream from the film hole, in that the accelerated flow model showed higher effectiveness past x/d≈100 [37].

When modelling film cooling numerically, the effects of chemically reacting flow in a nozzle are often overlooked. Amato et al. [24] included reacting flow in a quasi-2-D simulation of slot film cooling in a bipropellant nozzle. The nozzle contour used was used for the Space Shuttle Main Engine, which is similar to this thesis' configuration but at a larger scale. The film was injected at flow rates up to 50lb/s, or about 22.7kg/s, or 4.4% of the freestream flow rate. This flow rate is similar to the flow rate used in this thesis (which is about 5.9% of the freestream flow rate). It was found that chemically reacting flow affects heat flux quantitatively from 10% to upwards of 20% depending on wall temperature. Heat flux remains the same qualitatively, as heat flux profiles were virtually unchanged. This shows that reacting flow should be considered when numerically modelling a film cooling nozzle in order to account for the effects on heat transfer. However, axisymmetric 2-D simulations are limited as they assume that all phenomena occurring in the simulation is constant in the 3rd dimension, and so further work is needed to ensure the accuracy of the results found. Also, since this numerical investigation was based on slot film, it does not capture the effects of discrete film cooling, which is the subject of this thesis. This author proposes more localized cooling with the use of discrete film holes at a lower coolant flow than used by Amato.

Amato et al. also suggested methods of improvement in this numerical simulation. Including a wall solid around the hot gas simulation would increase accuracy instead of

establishing an adiabatic temperature profile for the outer wall. It also would be beneficial to include a more in-depth kinetic model for simulating reacting flow, as well as including an injector at the entrance of the thrust chamber in order to capture the mixing and burning of the fuel and oxidizer. Furthermore, Amato et al. suggested looking into 3-dimensional simulations, as well as adding cooling channels to the nozzle wall to investigate the interaction between the two. These suggested improvements were included in this thesis.

In order to increase internal cooling effectiveness in a rocket nozzle, either the nozzle liner must be reduced in thickness or the mass flow rate of the coolant must be increased. However, it is not feasible to shrink the liner thickness due to manufacturing and material limits. Also, increasing the mass flow rate of the coolant flow in the internal channels requires a significant increase in pumping power in order to compensate for the increased pressure drop, which requires a larger turbo pump. Arnold et al. [2009] investigated the effects of modifying injector flow to produce a liquid oxygen film along the nozzle wall. It was relatively effective, however because of the variations produced by injector dynamics, the film had significant circumferential variation [38].

Thermal Strain and Thermal Stress

Rocket nozzles undergo intense stress and strain during operation. A significant portion of this stress and strain is thermal-related. Thermal stress is caused by temperature gradients existing within a body: for a rocket nozzle, the greatest temperature gradient exists between the hot gas-side wall and the backside outer wall. As explained previously, heated material expands, and cooled material contracts. Since one side of the nozzle is subject to intense heat

and the other side subject to the environment, there exists both expansion and contraction, which gives way to thermal strain. Thermal strain is related to the eventual failure of rocket nozzles after repeated cycles. Thermal strain can be represented with Eqn. (4)

$$\varepsilon = \alpha \Delta T \tag{4}$$

ε is the thermal strain and α is the linear thermal expansion coefficient.

Low-Cycle Fatigue

In order to properly convey cooling effectiveness, it was important to make a connection between increased nozzle performance and cooling effectiveness. In his investigation on nozzle low-cycle fatigue, Quentmeyer [17] correlated the number of cycles to failure (Nf) with both the maximum hot gas wall temperature and the maximum ΔT between the hot gas wall and the outer nozzle wall. Using these correlations with the material OFHC, it is possible to calculate the predicted Nf using the max hot gas wall temperature of each simulation. The correlations are as follows: the first set in terms of Kelvin, Eqn. (5) & Eqn. (6); and the second set in terms of Rankine, Eqn. (6) & Eqn. (8).

$$T_{gw} = \frac{5}{9} 4520 N_f^{-0.205} \tag{5}$$

$$\Delta T = \frac{5}{9} 3920 N_f^{-0.178} \tag{6}$$

$$T_{gw} = 4520 N_f^{-0.205} \tag{7}$$

$$\Delta T = 3920 N_f^{-0.178} \tag{8}$$

Rearranging these equations, we arrive at the correlations for the number of cycles to failure, based on T_{gw}, Eqn. (9), and ΔT, Eqn. (10), in Rankine; and similarly in Kelvin for T_{gw}, Eqn. (11), and ΔT, Eqn. (12).

$$N_f = \left(\frac{T_{gw}}{4520}\right)^{-4.87805} \tag{9}$$

$$N_f = \left(\frac{\Delta T}{3920}\right)^{-5.61798} \tag{10}$$

$$N_f = \left(\frac{\frac{9}{5}T_{gw}}{4520}\right)^{-4.87805} \tag{11}$$

$$N_f = \left(\frac{\frac{9}{5}\Delta T}{3920}\right)^{-5.61798} \tag{12}$$

The correlation based on the maximum ΔT is actually based on the maximum range of ΔT and is used when being able to measure transient thermal strain. This relation is not attainable in this steady-state simulation. However, the correlation based on maximum hot gas-side wall temperature is attainable in a steady state simulation, and so this correlation will be used in order to determine the effectiveness of each cooling configuration. While the N_f calculated may not be exact, it shows a good example of representing cooling effectiveness in relation to rocket nozzle longevity and performance. Quentmeyer plotted this correlation on a log-log graph, which has been reproduced in Figure 2:

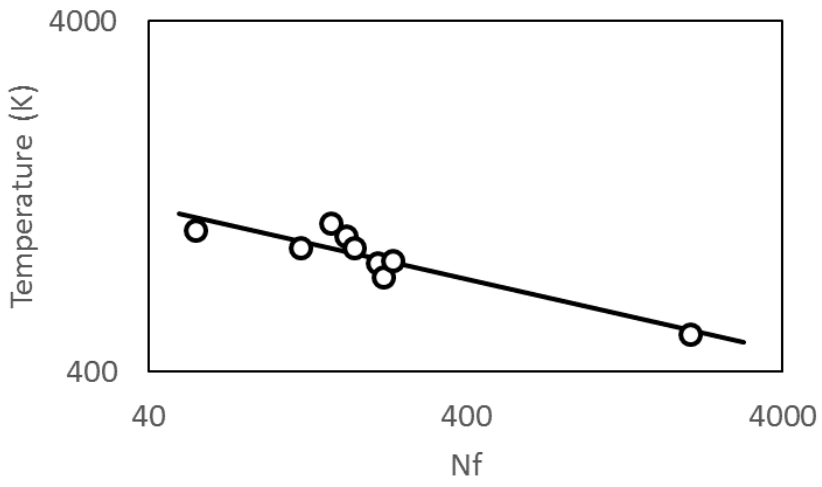

Figure 2: Nf vs Temperature in log/log format for OFHC Copper

These correlations show that the effectiveness of the cooling configuration can be characterized well by assessing the peak hot gas-side wall temperature. The cooling target in this study is to reduce the max hot gas wall temperature down 613K, which translates to an Nf of 971 cycles to failure.

Turbulators and Cooling Methods

Turbulating coolant has been the subject of research for some time. Coolant can be turbulated in either internal cooling configurations or film cooling configurations. Some studies in film cooling highlight that turbulating the flow prior to or after its injection can increase film cooling effectiveness. The most commonly-researched method is placement of turbulators in the channel that the coolant flows into. Bunker and Bailey observed experimentally that, depending on turbulator placement and flow orientation, discharge coefficients can both increase or decrease between 5 and 20 percent. The discharge coefficient helps determine the effectiveness of the film cooling method, where a high discharge coefficient yields higher film

cooling effectiveness. When cooling holes are placed just aft of the turbulator, a decrease in discharge coefficient is observed. However, placing the cooling holes just prior to the turbulator allow for an increase in discharge coefficient. The effect on the discharge coefficient is highly dependent on turbulator placement relative to the film cooling hole [39].

Turbulating the coolant is a technique that is found mostly in gas turbine cooling, where coolant used for internal cooling is eventually bled out along the surface of the turbine blade for additional cooling. This method of cooling, while similar to rocket thrust chamber liner cooling, does not produce useful work and so is not considered a form of regenerative cooling. On the contrary, rocket nozzle internal coolant is expanded through a turbine that runs a turbo pump, and is then burned in the thrust chamber to provide thrust. This thesis does not address turbulating the film, but focuses on conventional regenerative cooling techniques augmented with discrete hole film cooling that is separate from the regenerative cooling channels. Turbulating the coolant flow within the channels, however, is investigated to measure if there is further improvement in cooling effectiveness. The design is a combination of gas turbine cooling techniques and conventional rocket nozzle cooling techniques.

While turbulating the coolant in cooling channels is popular in gas turbomachinery research, there has been little to no research on turbulating the flow in regenerative cooling channels. Turbulated coolant flow is non-existent in current rocket nozzles and thrust chambers. Turbulating the flow allows for the cooler fluid near the cold side of the channel to mix with the coolant at the hot size of the channel, increasing heat transfer throughout the coolant. Before looking at ribs for turbulating flow, the effects of sand grain roughness on heat

transfer coefficient was investigated and correlated by Dipprey and Sabersky [40]. One of the earliest works on applying rib turbulators to rectangular channels was presented by Han et al. in 1978 [41] which was preceded by works investigating turbulators in circular pipes, namely by Webb et al. [42-44]. Webb et al. performed a number of experiments and developed a general correlation to predict heat transfer coefficients for ribs in cooling channels. Furthering this work, Chandra et al. extended these correlations to channels with multiple ribbed walls [45]. Rallabandi et al. [46] extended the roughness function approach to square channels with ribs oriented 45° to the flow, and also studied the effects of sharp-edged versus rounded-edged ribs. These works [40, 42, 43, 45-47] were notable in their application of the law-of-the-wall similarity, used earlier by Nikuradse to correlate friction in rough pipes [48].These works [40, 42, 43, 45-47] were notable in their application of the law-of-the-wall similarity, used earlier by Nikuradse to correlate friction in rough pipes [48].

When determining the effects of the geometry of the turbulator ribs, Rallabandi et al. [46] found that sharp edge and rounded edge ribs have similar heat transfer performance. There is concern that sharp-edged ribs have low life due to the stress concentrations at edges. Since the performance is similar between both sharp and round-edge ribs, this concern can be easily addressed with rounded ribs.

While there is extensive research on turbulated internal cooling, this research has not been applied to internal cooling research in rocket nozzles. Hossain et al. [49] numerically investigated the effects of rib turbulators in internal cooling channels representative of high-aspect ratio cooling channels. The longitudinal ribs in the channels caused a temperature

reduction of 32K, with a less than 1% pressure rise compared to conventional, non-turbulated designs. Apart from this sole publication, there is lack of research into this configuration specifically for cooling thrust chambers. Essentially, the effect of the turbulators is to locally enhance the heat transfer coefficient and it is fairly straightforward to design cooling channels with turbulators if the heat transfer coefficient is known beforehand.

Expected Contributions

The focus of this thesis is to investigate feasibility of introducing discrete film cooling to a regeneratively-cooled nozzle by investigating heat transfer effects. Normally, regenerative cooling is seen on its own in the thrust chamber, and film cooling is seen in the nozzle extension or as slot film cooling at the injector of the thrust chamber. This author proposes to combine both regenerative and discrete film cooling in the thrust chamber. This is necessary as there is limited research on how discrete film cooling behaves inside a combustion chamber when combined with regenerative cooling methods. This design will come with consequences that will require explanation and solutions. This design is a significant change applied to the original HARCC cooling configuration, and will be investigated three-dimensionally and numerically, a combination which has previously been determined impossible. If this analysis indicates that cooling effectiveness increases overall and max hot gas wall temperature decreases, then overall engine life can also increase since the engine can run at a high combustion temperature with cooler walls. This will prove feasibility of such a design and make way for further improvements of the design through optimization.

NOZZLE GEOMETRY

The nozzle is similar to contours used for modern-day rocket nozzles. Conical nozzles were suitable for earlier rocket designs, and are cheap and easy to manufacture. Conical nozzles may be acceptable for studying the regenerative cooling performance [50], but do not accurately represent the flow field in a contoured nozzle which is needed to study interaction of the film jet with the hot gas. Annular nozzles exceed in performance due to their altitude-compensating characteristics, however there are several disadvantages associated with this design that make a bell nozzle the better choice for analysis. Annular nozzles are difficult to manufacture due to their complexity, and require much more sophisticated cooling methods because of their unique geometry. The heat fluxes are higher, and the surface areas needing to be cooled are much larger [3]. Furthermore, there are no annular nozzle rockets flying today, and so it is more useful to explore new cooling configurations within nozzles that are currently in use.

The nozzle contour selected is based on an 89kN thrust chamber used for testing at NASA Lewis Research Center, a contour which was used for experimentation by Wadel [51]. This contour will be used as a base that will be modified according to each cooling configuration tested. A CAD model of the nozzle using this contour is displayed in Figure 3:

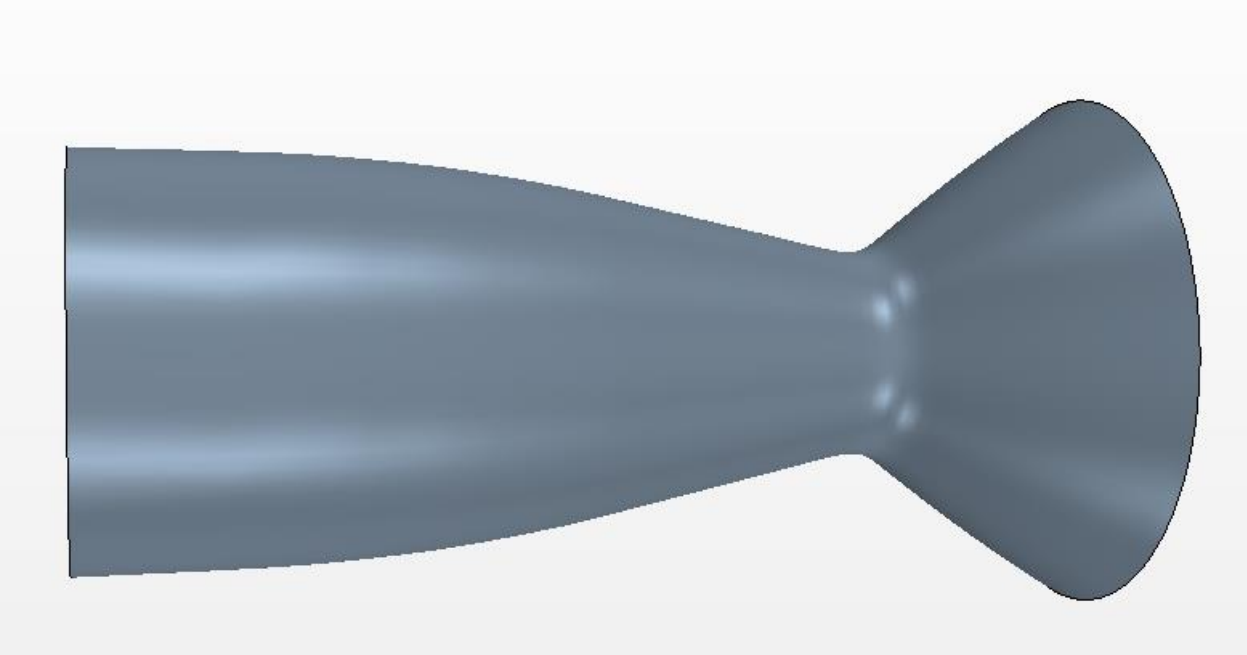

Figure 3: CAD Model of Rocket Nozzle Contour

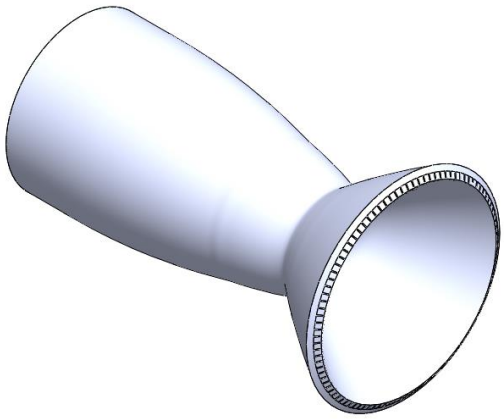

Figure 4: CAD Model of Thrust Chamber with Regenerative Cooling Channels, Isometric View

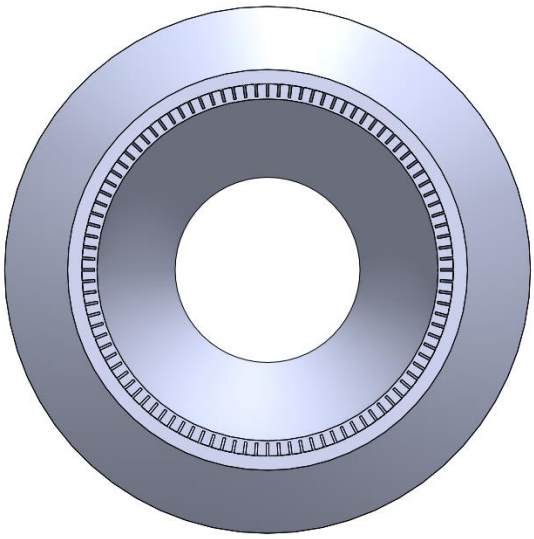

Figure 5: Axial View of Thrust Chamber With Channels, Liner, & Jacket

The contour shows a truncated nozzle, as the existing nozzle using this contour was tested at sea-level, and so could be truncated where the internal pressure reaches atmospheric conditions. Figure 6 shows the nozzle contour graphically, tabulated in Table 4. Table 4 also includes the local channel width and height of the regenerative cooling channels used in this thesis, which is Design 1 w/ fabrication constraints (see Table A-VIII) in Wadel's thesis [16]. Figure 4 is an isometric view of design with 100 regenerative cooling channels. Figure 5 is a view of the thrust chamber along the axis of the nozzle. The inlet diameter of the nozzle is 4.8 inches and the throat is 2.6 inches in diameter. The thickness of the liner wall between the hot-gas and nearest surface of the cooling channels is taken to be a constant thickness, 0.035in. The liner is made of oxygen-free high conductivity (OFHC) copper. The structural closeout jacket, made of electrodeposited nickel, 0.200in thick.

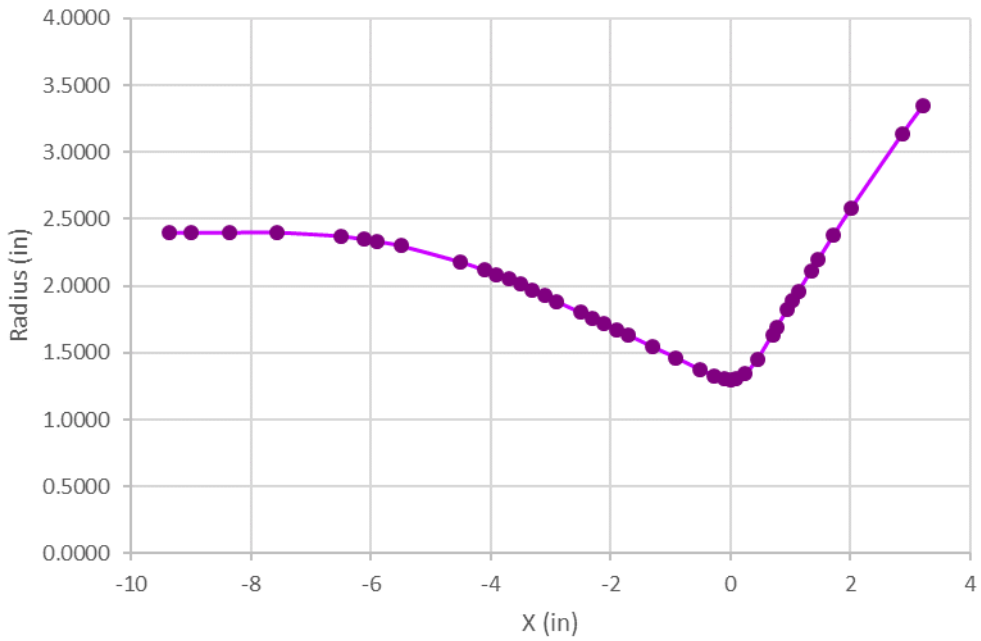

Figure 6: Nozzle Contour

Table 4: Nozzle and Coolant Channel Geometry

X (in)	Diameter (in)	Channel Width (in)	Channel Height (in)
-9.375	4.8	0.035	0.179
-9	4.8	0.035	0.179
-8.35	4.8	0.035	0.179
-7.572	4.8	0.035	0.179
-6.506	4.744	0.035	0.179
-6.106	4.694	0.035	0.179
-5.906	4.666	0.035	0.179
-5.5	4.6	0.035	0.179
-4.506	4.358	0.035	0.179
-4.106	4.236	0.035	0.179
-3.906	4.17	0.035	0.179
-3.706	4.1	0.035	0.179
-3.506	4.022	0.035	0.179
-3.306	3.94	0.035	0.179
-3.106	3.86	0.035	0.179
-2.906	3.77	0.035	0.179
-2.506	3.602	0.035	0.179
-2.306	3.516	0.035	0.179
-2.106	3.432	0.032	0.195
-1.906	3.344	0.032	0.195
-1.706	3.264	0.03	0.2
-1.306	3.092	0.029	0.198
-0.906	2.924	0.027	0.194
-0.506	2.746	0.023	0.174
-0.274	2.656	0.023	0.174
-0.100	2.608	0.023	0.174
0.000	2.6	0.023	0.174
0.1	2.613	0.023	0.174
0.25	2.686	0.023	0.174
0.452	2.902	0.023	0.174
0.701	3.272	0.023	0.174
0.778	3.388	0.023	0.174
0.947	3.64	0.023	0.174
1.038	3.776	0.029	0.181
1.135	3.916	0.03	0.183
1.347	4.226	0.031	0.185
1.464	4.392	0.033	0.182
1.719	4.754	0.035	0.179
2.009	5.154	0.035	0.179
2.872	6.28	0.035	0.179

The RL10 Rocket Engine

This contour is the same contour used for the RL10 engine. The RL10 is a robust engine developed in the late 1950s-1960s by Pratt & Whitney and Aerojet Rocketdyne. It was originally used as an upper stage booster, but was then modified for use in the Space Shuttle program as a booster engine. It is still being used today in the Boeing Delta III rocket and the upper stage of the Centaur Atlas V rocket. Its 100% mission success rate makes the RL10 a popular engine for modern rocketry even after 50+ years [52].

The RL10 uses regenerative cooling to cool the nozzle, using supercritical hydrogen as the coolant, which is later fed into the combustion chamber as fuel [52]. This engine also uses the closed expander cycle for operation. The closed expander cycle allows for the elimination of a pre-burner or gas generator, which is useful for rocket engine design due to a reduction in both engine complexity and weight [1]. However, it is important to note that the relation between the size of the nozzle and thrust is limited by the square-cube rule. This rule asserts that, since the surface area of the nozzle increases with the square of the radius, the volume of fuel heated increases with the cube of the radius. Therefore, there is a limit to the thrust at approximately 300kN for any engine using the expander cycle. However, this limitation could be mitigated by replacing some internal cooling with film cooling, since film cooling is not limited in this manner. The presence of surplus hydrogen is more prevalent with increased size of the nozzle, and so film cooling in a nozzle is increasingly applicable for larger nozzles. Other rocket nozzles use the open expander cycle or gas generator cycle, which can also utilize discrete film

cooling since the exhaust flow from the turbine is not used, and could be repurposed for cooling.

The cooling channels in the nozzle used for this analysis can be machined in two ways: milling the channels and closing out the channels with the nickel outer wall or brazing the channels. In the specific nozzle used for this investigation, the channels were machined. While there are nozzle geometries that can produce better results with complex channel and nozzle designs, it is useful to analyze current robust designs, especially considering manufacturing cost differences with current technology.

NUMERICAL SETUP

Computational Fluid Dynamics was performed using STAR-CCM+ software, version 11.02.009. Each configuration uses the same general nozzle geometry, however the cooling designs, such as the inclusion of regenerative cooling channels and addition of film holes, make each nozzle design different. CAD Geometry was created in SolidWorks version 2015-2016 and 2016-2017.

Many numerical simulations use 2-dimensional models to predict outcomes [24, 53, 54]. However, it has been proven that the environment in a rocket nozzle varies in 3-dimensional ways [21]. Furthermore, combining internal and film cooling requires at least a minimum thickness to the geometry due to the juxtaposition of the cooling channels and film holes.

While 3-dimensional simulations increase accuracy by modelling the complex 3-dimensional phenomena present in the turbulent environment of a rocket thrust chamber, they also come with their own problems. Cell skewness is the cause of many divergent solutions. Skewness angle is the angle between the face normal vector of a cell and the vector connecting an adjacent cell centroid and the original cell centroid. If a cell has a high skewness angle, that means that the nature of the cell does not permit diffusion of properties and quantities, which can lead to solution divergence. STAR-CCM+ developers recommend maintaining a maximum skewness angle of under 85°. Refining a mesh so that skewness angle remains under 85° can take an extensive amount of time depending on the quality of the mesh. Finer meshes generally contain less skewed cells; however, a finer mesh means that the simulation is computationally expensive. Computational fluid dynamics is a constant battle with optimization of simulation

accuracy and computational complexity. However, the inherent need of 3-dimensional analysis for a rocket nozzle with a complex cooling configuration justifies the extra time and effort it takes to develop such a simulation.

Configuration 1 illustrates the complications associated with a thin wedge and assuming radial symmetry with such a small sector of 1.8°. Configurations 2 through 5 illustrate a nozzle section of 36° that takes into account both accuracy and computational expense.

Methodology

Each simulation uses the same general governing equations. All the simulations are run as steady-state, 3-dimensional, with the fluids modelled as compressible fluids and the solids modelled as constant density. The flow and energy equations are explained further.

Turbulence and Flow Governing Equations

The fluid is modelled with the assumption of no heat generation, or no viscous dissipation. This is because, due to the nature of the mesh and its cell density, the mesh does not completely resolve the near-wall velocity profile where heat generation takes place. The simulations use steady state Reynolds-Averaged Reacting Navier Stokes (RANS) equations, or Favre-Averaged Navier-Stokes (FANS) for variable density flows, coupled with the realizable k-ε turbulence model. FANS can be characterized by the three equations: continuity, Eqn. (13); momentum, Eqn. (14); and energy conservation, Eqn.

(19).One can derive these RANS/FANS equations by starting with the instantaneous Navier-Stokes equations, performing a Reynolds decomposition or Favre decomposition (splitting the

instantaneous flow into a mean part and fluctuating part), and then simplifying the equations to arrive at an equation for the mean velocity. When density varies, Reynolds decomposition results in high-order correlated terms; Favre-averaging however, recovers equations that do not have high-order correlated terms and have equivalent form to the RANS.

Continuity:

$$\frac{\partial \bar{\rho}\widetilde{u_i}}{\partial x_i} = 0 \tag{13}$$

Momentum conservation:

$$\frac{\partial}{\partial x_j}\left[\bar{\rho}\widetilde{u_i}\widetilde{u_j}\right] = \frac{\partial}{\partial x_j}\left[-\bar{p}\delta_{ij} + \overline{\tau_{ji}} - \overline{\rho u_i'' u_j''}\right] \tag{14}$$

For a Newtonian fluid, the viscous stresses are given by Eqn. (15). The laminar stresses are therefore given by Eqn. (16).

$$\tau_{ij} \equiv \mu\left[\left(\frac{\partial u_i}{\partial x_j} + \frac{\partial u_j}{\partial x_i}\right) - \frac{2}{3}\frac{\partial u_k}{\partial x_k}\delta_{ij}\right] \tag{15}$$

$$\overline{\tau_{ij}} \equiv \mu\left[\left(\frac{\partial \widetilde{u_i}}{\partial x_j} + \frac{\partial \widetilde{u_j}}{\partial x_i}\right) - \frac{2}{3}\frac{\partial \widetilde{u_k}}{\partial x_k}\delta_{ij}\right] \tag{16}$$

The turbulent stresses are modelled by invoking the Boussinesq hypothesis and assuming that the turbulent stresses are similar to the laminar stresses except with a turbulent viscosity instead of a molecular viscosity, as given by Eqn. (17). Note that the turbulent viscosity is a property of the flow; unlike the molecular viscosity, the turbulent viscosity is not a material property. The calculation of the turbulent viscosity is embedded in the turbulence model. The

advective term of the equations is discretized in STAR-CCM+ by 2nd-order upwind method. The diffusion term of the equations is discretized by 2nd-order central differencing.

$$-\overline{\rho u_i'' u_j''} \approx \mu_t \left[\left(\frac{\partial \widetilde{u_i}}{\partial x_j} + \frac{\partial \widetilde{u_j}}{\partial x_i} \right) - \frac{2}{3} \frac{\partial \widetilde{u_k}}{\partial x_k} \delta_{ij} \right] - \frac{2}{3} \bar{\rho} \tilde{k} \delta_{ij} \tag{17}$$

The turbulent kinetic energy is defined per Eqn. (18).

$$\frac{1}{2} \overline{\rho u_i'' u_i''} = \bar{\rho} \tilde{k} \tag{18}$$

Energy conservation:

$$\frac{\partial}{\partial x_j} \left[\bar{\rho} \widetilde{u_j} \left(\tilde{h} + \frac{1}{2} \widetilde{u_i} \widetilde{u_i} \right) + \frac{1}{2} \widetilde{u_j} \overline{\rho u_i'' u_j''} \right]$$

$$= \frac{\partial}{\partial x_j} \left[\left(\overline{\tau_{ij}} - \overline{\rho u_i'' u_j''} \right) \widetilde{u_i} - \overline{q_j} - \overline{\rho u_j'' h''} - \overline{u_i \tau_{ij}} \right] + S \tag{19}$$

S is a source term which is not present in many fluid flow problems; however, with chemical reactions there is a heat source (the heat released via the reaction).

The heat diffusion term is usually taken to follow Fourier's law of heat conduction, Eqn. (20), which gives Eqn. (21) for the laminar time-averaged component. The turbulent transport of heat ($\overline{\rho u_j'' h''}$) is usually modelled using an effective conductivity (or turbulent Prandtl number) according to Eqn. (18).

$$q_j = -c_p \frac{\mu}{Pr} \frac{\partial T}{\partial x_j} \tag{20}$$

$$\overline{q_j} = -c_p \frac{\mu_t}{Pr_t} \frac{\partial \tilde{T}}{\partial x_j} \tag{21}$$

$$\overline{\rho u_j'' h''} \approx -c_p \frac{\mu_t}{Pr_t} \frac{\partial \tilde{T}}{\partial x_j} \tag{22}$$

The turbulent Prandtl number is a modeled parameter, and is usually taken to be a constant 0.9. The turbulent heat flux is often overlooked by CFD users. Most users are actively aware of the prevailing presence of the turbulent viscosity, Eqn. (17); however, many users are not aware that the energy equation also needs additional models to close the equations. Users are quick to place blame on the inadequacy of turbulence models for when CFD results are not in agreement with experimental observations. Users continuously question, "Why does the pressure drop match but not the heat transfer?" These users fail to recognize that even if the turbulence model predicts the correct flow field, an incorrect turbulent Prandtl number can still predict the transport of heat incorrectly. The development of better models for the turbulent Prandtl number (with more fidelity than assuming a simple constant) has been mostly ignored by the modelling community. However, reasonable progress and success has recently been made by Weihing et al. [55], for turbulated channels. A major influence and driver in the development of better turbulence closure models has taken root in applications with turbulated channels, where the Boussinesq hypothesis is generally not valid.

The realizable k-ε turbulence model can be described in the following two transport model equations: the transport equation for k, Eqn. (23), and transport equation for the turbulent dissipation rate, Eqn. (24).

Transport Equation for the Turbulent Kinetic Energy:

$$\frac{\partial}{\partial t}(\bar{\rho}\tilde{k}) + \frac{\partial}{\partial x_j}\left(\bar{\rho}\tilde{k}\widetilde{u_j} - \left(\mu + \frac{\mu_t}{\sigma_k}\right)\frac{\partial \tilde{k}}{\partial x_j}\right) = P_k - \bar{\rho}\tilde{\varepsilon} \tag{23}$$

$$\frac{\partial}{\partial t}(\bar{\rho}\tilde{\epsilon}) + \frac{\partial}{\partial x_j}\left[\bar{\rho}\tilde{\epsilon}\widetilde{u_j} - \left(\mu + \frac{\mu_t}{\sigma_\varepsilon}\right)\frac{\partial \tilde{\epsilon}}{\partial x_j}\right] = \bar{\rho}C_{\epsilon 1}S\tilde{\epsilon} - \bar{\rho}C_{\epsilon 2}\frac{\tilde{\epsilon}^2}{\tilde{k} + \sqrt{\nu\tilde{\epsilon}}} \tag{24}$$

where the production term (P_k) is modelled and C_ε are additional model constants. Various model constants are involved that are omitted here for the sake of brevity; eventually the turbulent viscosity is computed using Eqn. (32), which finally closes the equations.

$$\mu_t = \bar{\rho}C_\mu \frac{\tilde{k}^2}{\tilde{\epsilon}} \tag{25}$$

The need for two additional transport equations should be apparent in Eqn. (25), but this approach is specific to the realizable k-epsilon model. Other turbulence models may use different approaches to compute or even correlate the turbulent viscosity.

Chemistry and Species Transport Model

Complex Chemistry

Detailed chemistry, identified as complex chemistry within STAR-CCM+, models the combustion mechanisms within the simulation. The H_2/O_2 reaction can be set up in a number of ways based on type of combustion specified.

Burke's documentation of the reaction [22] was inputted into STAR-CCM+, however Argon, Nitrogen, and Helium were omitted from the reaction since they are not present in the nozzle. Including the three additional species requires transport equations for each species to be solved, which would be a computational waste since they are unnecessary. Complex

chemistry is solved using STAR-CCM+ CVODE solver. The turbulence-chemistry interaction is modelled using the eddy-dissipation concept.

Species Transport

A species transport model defines mass fractions in order to solve for concentration as a function of space. Species transport is based on the general transport equation while also taking into account mass fractions of each species present. Mass fractions are derived from a simplified version of Burke's 11-species version. Since each species requires its own set of segregated energy equations, each species will require the CFD solver to work with several ODEs and PDEs, which are all extremely complex. It is best to improve both accuracy and computational time by including the most common mass fractions in the hydrogen/oxygen chemical reaction.

Configuration 0, the hot gas model that includes the injector, used all 11 species save for Argon, Nitrogen, and Helium for species transport in order to measure the effects of including all mass fractions present. Argon, Nitrogen, and Helium are not present in the thrust chamber, and so were disregarded.

The steady state species transport equations can be written as follows, Eqn. (26).

$$\frac{\partial}{\partial x_j}(\rho \vec{u} Y_i) = -\frac{\partial}{\partial x_j}\left[\vec{J_\iota} + \frac{\mu_t}{\sigma_t}\frac{\partial Y_i}{\partial x_j}\right] + R_i \tag{26}$$

Y_i is the local mass fraction of the i-th species, J is the diffusive flux, and R is the rate of production of species in a chemical reaction which is calculated by solving the kinetic model.

Each species uses a version of this equation related to the specific mass fraction, and so adding species becomes increasingly computationally expensive.

The full multi-component diffusion approach was not used in this thesis, and Fick's law for the diffusive flux is given by, Eqn. (27). Soret effects were also not included (no thermal diffusion). The Schmidt number was assumed to be unity ($\sigma = 1$) so that the mass diffusivity was equal to the kinematic viscosity. The turbulent Schmidt number was also left at the default value ($\sigma_t = 0.9$).

$$J_i = \rho D_i \nabla Y_i \tag{27}$$

In a real rocket nozzle, fuel is injected and mixed within the thrust chamber. The mixing involves fuel and oxidizer droplet breakup, a complex process that has not been successfully simulated at this time. Because of this, true inlet mass fractions cannot be found. The other alternative is to run an experiment using the nozzle itself and measure the mass fractions experimentally, which is outside the scope of this thesis. This means that the fluid behavior soon after injection cannot be properly simulated with CFD, and so it is important to determine when the effects of the injector and mixing are nonexistent, as this is the point where the results are accurate and comparable.

Boundary Conditions

Boundary conditions were set in order to maintain similarity to Wadel's Design 1 configuration. Coolant flowed through the channels with an inlet static temperature of 44K, which corresponds to a total temperature of 44.4K. The nominal mass flow rate for the channels is 2.3kg/s total, or 0.023kg/s per channel (if 100 channels are used). Outlet static

pressure of each cooling channel is specified as 11MPa in accordance with Wadel's constraints. The pressure of the coolant at the channel exit should be greater than the pressure of the propellants at the injector inlet. The turbulent length scale is based on the hydraulic diameter of the channel, which is 0.004m. The turbulence intensity is left at the default of 0.01. These are calculated using the following equations: the turbulent intensity, Eqn. (28), and turbulent length scale, Eqn. (29).

$$I = Re^{-1/8} \tag{28}$$

$$l = 0.07D_h \tag{29}$$

The hot gas inlet temperature is dependent on the species transport model and complex chemistry model. Outlet pressure of the nozzle is atmospheric, or 101,325Pa. The inlet turbulent length scale is set to 0.005m, and the outlet turbulent length scale, which is only needed if there is backflow, is 0.15in, or approximately 0.004m.

Apart from the surface of the meshed channel, the jacket surfaces that come into contact with each channel in configurations 2 through 5 use surface temperatures that are mapped from the meshed channel. The jacket outer surface is modelled as adiabatic, in congruence with the negligible effects of radiation and natural convection; the validity of this modelling assumption is studied further on.

Mechanical and Thermophysical properties

The mechanical and thermophysical properties of all the materials remain the same through every configuration. No material is changed in any of the simulations, and so the following information will articulate the material properties of each simulation in its entirety.

Channel

Various researchers mistake the physical state of hydrogen in the cooling channels as a conventional liquid because LPRE's imply that the fuel and oxidizer are liquids. The critical temperature and pressure of hydrogen are 33.15K and 1.296MPa, respectively. Since the temperature of the hydrogen when it enters the cooling channel is 44K and pressure at the inlet is greater than 11MPa, the hydrogen is actually in a supercritical state. For ease of visualization, the phase diagram of hydrogen is depicted in Figure 7. In the supercritical state, distinct boundaries between the liquid and gas phase do not exist and it is improper to declare the fluid either liquid or gas.

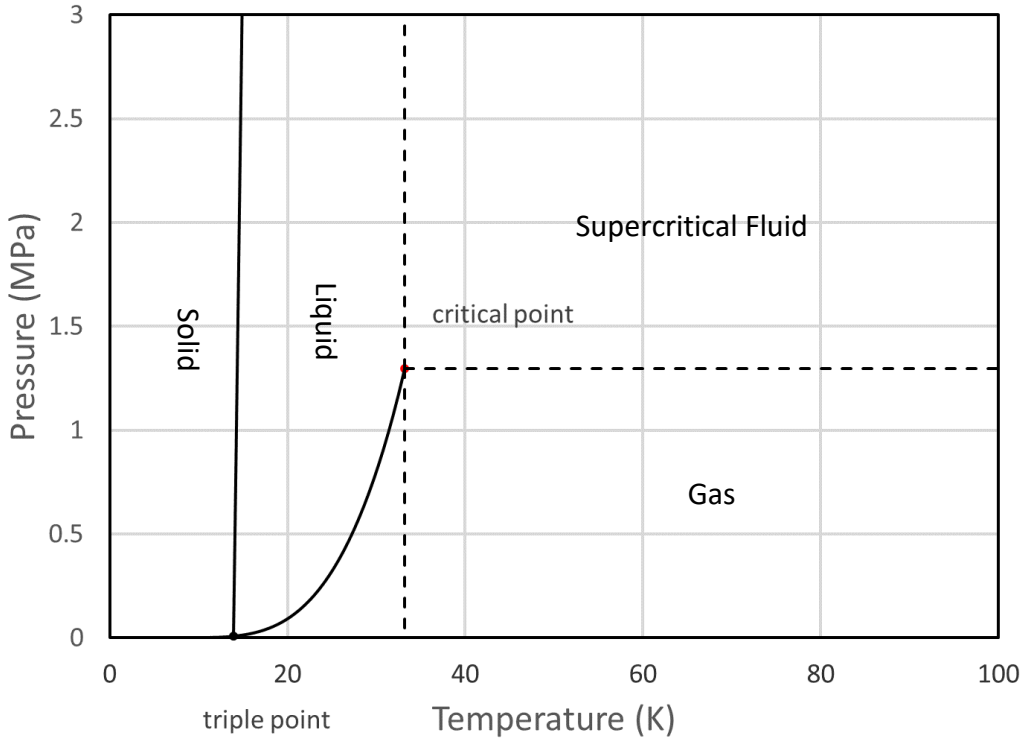

Figure 7: Phase Diagram of Hydrogen. Note that at 44K and 11MPa, hydrogen is supercritical

Near the critical point, thermophysical properties of a fluid can change wildly (between liquid-like and gas-like). It should be apparent that a supercritical fluid cannot be modelled as either a constant density liquid or an ideal gas. Hence, the coolant within the channel is modelled using a user-defined equation of state using tabulated properties from REFPROP. Thermophysical properties of hydrogen with respect to both temperature and pressure were imported based on values from REFPROP. REFPROP is a reputable source from a nationally-recognized organization, National Institute of Standards and Technology (NIST). Fluid properties were varied with temperature and pressure due to the inherent compressibility of hydrogen as a fluid and the large temperature changes within the channel itself. The properties were varied from 33.15K to 1500K, and 11MPa to 13MPa. The temperature of the coolant never reached 1500K in the converged solution; however, during iterations the temperature can exceed this number. Hence, when generating these property tables, it is recommended to generate them over an even broader range than the expected conditions.

Density was tabulated with only temperature variations at the nominal pressure of 11MPa. This is because the CFD solver, when confronted with a compressible density, cannot converge easily to the solution. The speed of sound in hydrogen is plotted against pressure and temperature in Figure 8 over typical conditions encountered in the simulations. The slowest sound speed is approximately 900 m/s. The maximum velocity encountered in the cooling channel is 333m/s. Hence, the greatest Mach number was 0.37, indicating that the flow is fairly incompressible. This is also a sufficient assumption since the pressure variation is small (a few MPa) compared to the nominal pressure (11MPa). Therefore, tabulating the density against

only temperature variations is reasonably adequate, although the accuracy of the results would be enhanced if the properties were tabulated against both temperature and pressure. The remaining properties, enthalpy, thermal conductivity, and viscosity were tabulated against both temperature and pressure.

To verify that the flow is indeed turbulent, the channel Reynolds number, Eqn. (30), must be calculated. The hydraulic diameter is defined according to Eqn. (31). Using the definition of the bulk average channel velocity, Eqn. (32), channel cross-sectional area, Eqn. (33), and wetted perimeter, Eqn. (34), the channel Reynolds number from Eqn. (30) can be re-written as in Eqn. (35).

$$Re = \frac{\rho \bar{u} D}{\mu} \tag{30}$$

$$D_h = \frac{4Ac}{P_{wet}} \tag{31}$$

$$\bar{u} = \frac{\dot{m}}{\rho A_c} \tag{32}$$

$$A_c = H \cdot W \tag{33}$$

$$P_{wet} = 2(H + W) \tag{34}$$

$$Re = \frac{4\dot{m}}{\mu P_{wet}} \tag{35}$$

Using a temperature of 44.4K, a viscosity of μ=8.3415e-6Pa·s, and a mass flow rate of 0.023kg/s per channel, the channel inlet Reynolds number is calculated to be 1 million. At the throat, the Reynolds number of the channel is even higher due to the shrinking P_{wet}. The Reynolds number increases or decreases relative to the change in channel flow rate. The lowest

mass flow rate used at 0.0115kg/s still results in a Reynolds number of half a million, which is still turbulent.

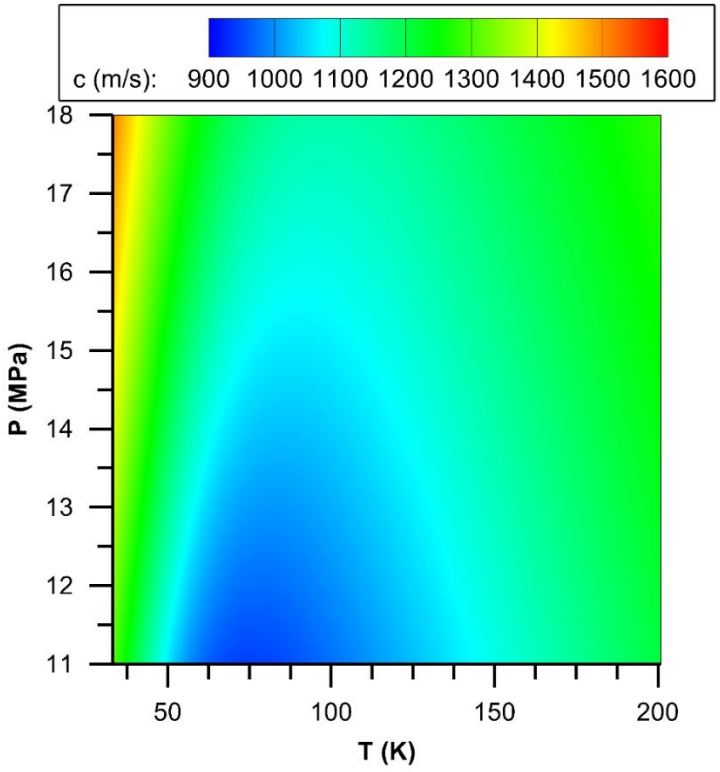

Figure 8: Speed of Sound as a Function of Temperature and Pressure

The coolant was modelled in 3-dimensional space, in congruence with the rest of the simulation. The energy equation was defined using segregated fluid temperature in earlier simulations, and segregated fluid enthalpy in later simulations.

Jacket

The outer shell of the nozzle, or the structural closeout jacket, is made of electroformed nickel due to its resilience in high temperatures and resistance to erosion and corrosion [3]. Mechanical properties for electro-formed nickel have been recorded by NIST in its cryogenic states, and are widely recorded by several sources at room temperature [56]. After research

into this other literature, it was determined that the STAR-CCM+ values for all properties including density, thermal conductivity, Young's modulus, etc. were comparable enough to use the defaults in Star-CCM. Furthermore, one might argue that it is important to look into varying the properties with respect to temperature, however the properties did not change drastically with temperature. Properties at 300K were chosen since 300K is approximately the median temperature for the entire jacket, and properties at room temperature are readily available in very specific and accurate measurements.

The jacket is modelled as steady-state, three-dimensional, constant density with finite volume solid stress, with segregated solid energy modelling the heat transfer. This is the only energy equation needed since the volume is fixed and this analysis is not based on a transient model. The effects of gravity on the simulation are negligible, and so are not factored into this analysis.

Liner

The liner is machined out of oxygen-free high conductivity copper (OFHC). OFHC is a common material used in rocket nozzles due to its purity that yields excellent thermal conductivity, ease of manufacturing, and high melting point. High thermal conductivity allows the cooling properties of the channels to reach the hot gas wall efficiently and effectively, and also lowers temperature gradient which helps to alleviate thermal strain. Like the jacket material, STAR-CCM+ properties were sufficient for this analysis due to the little variation between different temperatures and the fact that properties at 300K lay between the two temperature extremes seen in this simulation. Governing equations are identical to the jacket.

Equations of State

Each region of the nozzle is characterized by a different equation of state (EOS); however, each region maintains this equation of state throughout all cases. As previously stated, both the liner and jacket of the nozzle are modelled as constant density entities, and the coolant is modelled with a user-defined EOS. The hot gas is modelled as an ideal gas in order to be able to model the complex chemistry and species transport. The separate species themselves are characterized using either constant values or NASA thermodynamic polynomials. The thermal conductivity and dynamic viscosity are constant, whereas the specific heat, enthalpy, and entropy are all characterized by NASA thermodynamic polynomials.

General Mesh Properties

The mesh for each configuration using a 36° section includes virtually the same mesh properties. This includes configuration 0, 2, 3, 4, 5, and 6. The base size is 0.2in for all configurations, apart from configuration 0, where it is 0.15 in order to better test the accuracy of including the injector. Prism layers are included in the hot gas, film holes, and channel in order to accurately capture boundary layer interactions in the fluid volumes. The number of prism layers varies between channel and hot gas, where the channel normally contains 9 layers, and the hot gas contains 12 layers. The prism layer thickness is based on the computed boundary layer thickness. The boundary layer thickness was estimated to be 0.001m, or 0.04in. The reference values were kept relative to the base size for easy alteration. The prism layer thickness was set to 25% of the base size, or approximately 0.05in. Prism layer stretching was set to 1.3. Surface size was set to a minimum of 10% with a target size of 100% in order to

properly model the smaller surfaces present in the simulations, with a growth rate of 1.3. Further refining of the mesh was done in custom mesh value alterations in the region boundaries themselves, as well as interfaces.

The channel specifications were altered in order to avoid skewness in cells and maintain an ultra-fine mesh to accurately model heat transfer in the channel. The number of prism layers was specified as 8 layers with a growth rate of 1.3, and a thickness of 5% the base size, or 0.01in, which is computed the same way as the general boundary layer thickness, only using the channel dimensions instead of overall dimensions. Surface size in the interface between the channel and jacket was specified to be between 1% and 5% of the base size due to the high aspect ratio of the channels. The same trend is applicable to the interface between the bottom channel wall and the liner. Between the liner and the longer sides of the channel, or the “left” and “right” sides had a surface size specified between 2.5% and 50%. All other factors were left at general specifications.

Apart from the custom values articulated above, the liner and hot gas interface also used a custom surface size with a minimum of 10% to 100% in order to maintain the default values for this surface. Variations in mesh parameters depending on the cooling design are specified in their respective sections.

General Solution Strategy

After generating the mesh, selecting the desired physics models, assigning the proper boundary conditions, and establishing the initial conditions/guesses, the simulation could be run and iterated until convergence. However, obtaining a well-converged result is not a straightforward task. Some of the lessons learned during this process are recorded in this section.

With initial conditions assigned and running a new configuration for the first time, if all the under-relaxation factors were left at their default values, and all the solvers were activated, the solution usually diverged. After resolving poor cells in the generated mesh, the reason for the divergence can eventually be narrowed down to poor initial conditions. Many types of initial conditions were attempted, such as using estimates from one-dimensional isentropic relations to assigning local temperature and pressure initial conditions. Solutions from converged coarser meshes were also mapped onto new grids. However, divergence issues were still frequent. Eventually it was learned that having consistent initial conditions was the most important. That is, the initial condition for the velocities and pressures should be consistent with the initial conditions for the temperature; otherwise the solver has a tendency to diverge as it attempts to resolve these inconsistencies.

Lessons Learned

The most reliable procedure developed, was to first deactivate the segregated energy solver for the earliest iterations but keeping all other solvers active. Disabling the Bi Conjugate Gradient Stabilized accelerator in the AMG solver for pressure was also necessary. The

accelerator nearly always diverged in the early iterations and in many cases was the reason for the divergence as the solver was too aggressive in applying multi-grid methods. In this thesis, the segregated flow solver was applied using the SIMPLE scheme for the pressure-velocity coupling. Therefore, the accelerator is specific to the current work and it is possible that if another coupling scheme is used, that issue with the multi-grid accelerator may be avoided. Regardless, freezing the energy equation will still be necessary regardless of which pressure-velocity coupling scheme is used.

With the pressure accelerator and energy solver disabled, the simulation may begin. In this stage, many warnings are present for limiters on pressure corrections and temperature corrections. The iteration was allowed to continue until the pressure correction warnings no longer occurred. Essentially, the solver has calculated a reasonable flow-field given the temperature field established. In general, the pressure correction warnings stopped after approximately 30-100 iterations. The segregated energy solver could then be activated again. The AMG accelerator was kept disabled. However, a new problem arises since now the temperature field is inconsistent with the flow field.

After enabling the energy equation, the under-relaxation factors for the energy equation were ramped linearly from extremely small values (0.01) to the eventual desired values (0.9 for example). It was found that it was usually only necessary to ramp the under-relaxation factor for the fluid energy; the under-relaxation factor for the solid energy could be left at the default value of 0.99. However, in some cases it was also necessary to ramp the solid energy URF. Aggressive ramps over a period of 100 iterations had reasonable success, with

longer periods less likely to diverge. Whenever the user could monitor the solution progress (during normal business hours), aggressive ramps could be applied. If the simulation was run overnight however, conservative ramps over 500 iterations or 1000 iterations were used.

Most of the under-relaxation factors were left at their default (most aggressive settings). However, it was observed in general that stability was improved for some cases when the targeted under-relaxation factor for the fluid energy was reduced from 0.9 to 0.8. The under-relaxation factor for the turbulence solver was also reduced from 0.8 to 0.6.

After completing the ramp, they were disabled and the solution was monitored for another 500 iterations to ensure the solution was well behaved and converged to a steady result. After disabling the ramps, the Bi Conjugate Gradient Stabilized accelerator could be activated again to speed up the convergence.

Changing the boundary conditions (such as the coolant flow-rate or the film flow-rate) was generally done with an already converged result for a different case. After changing the boundary condition, the solution once again had a tendency to diverge. Various schemes of disabling solvers, ramping under-relaxation factors were attempted, with various degrees of success.

The most reliable method to solve for a different flow-rate however was to keep all the under-relaxation factors are their maximum values and instead ramp the flow-rate. For many cases, ramping the boundary condition over 100 iterations was sufficient to prevent divergence errors. Spending 100 iterations to ramp the boundary condition was much faster than repeating the procedure used with the initial conditions to obtain the first successfully converged

simulation. If 100 iterations were not enough, then it could easily be increased to 200, 500, 1000, or 2000. For the most complex configurations, this ramp had to be done over 2000 iterations. Ramping the under-relaxation factors was also experimented on, but it generally did not provide any significant improvement. Hence, it is recommended to use the maximum URFs that the user is comfortable with and to ramp the boundary condition to solve for successive cases using the same mesh.

NEGLECTED FACTORS

Free Convection

When taking into account gravity, free convection exists between a hot gas and a cool plate: in this case, the hot gas is the gas in the thrust chamber, and the cool plate is the hot gas-side wall. Free convection is driven by buoyancy forces due to density changes (where the density changes are a result of the temperature distribution in the flow problem). In order to justify not taking them into account, calculations were performed after obtaining results from the baseline configuration. Nusselt number based on free convection was calculated at the throat using Rayleigh number, which is calculated using Grashof number and Prandtl number. The Prandtl number (Pr) is a dimensionless number defined as the ratio of momentum diffusivity over thermal diffusivity, Eqn. (36).

$$Pr = \frac{\nu}{\alpha} \tag{36}$$

where v is kinematic viscosity and α is thermal diffusivity. Since the Prandtl number is a ratio of two (transport), it is a (derived) material property and does not need to be specified explicitly. All temperatures and properties were extracted from the baseline simulation. The Grashof number, Gr, is calculated using Eqn. (37).

$$Gr = \frac{g\beta(T_s - T_\infty)L^3}{\nu^2} \tag{37}$$

where g is gravity, β is the volumetric thermal expansion coefficient, T_s is the surface temperature (which for this purpose is T_{gw}), T_∞ is the freestream temperature, and L is the diameter of the nozzle throat. At the throat, Gr equates to 6.6×10^8, and Pr equates to 1.44.

After calculating the Rayleigh number from Eqn. (38), one can use a correlation for the upper surface of a hot plate or lower surface of a cold plate, Eqn. (39), to estimate the Nusselt number for this configuration.

$$Ra = GrPr \tag{38}$$

$$\overline{Nu}_L = 0.15Ra^{\frac{1}{3}} \tag{39}$$

Nu at the throat from free convection equates to 147. This corresponds with a heat transfer coefficient of 81.3 using Eqn. (40).

$$Nu = \frac{hL}{k} \tag{40}$$

When Gr/Re^2 is << 1, the effect of free convection versus forced convection is negligible. At the throat, Gr/Re^2 is much less than 1, and so the free convection can be disregarded.

From the baseline configuration simulation, the boundary wall heat flux at X=0, or at the throat, is found to be 66 MW/m^2. Heat transfer coefficient at X=0 is also extracted from the simulation and found to be 23 500 W/m^2K. Using equation 24, Nu from forced convection is calculated to be 43,000. When comparing the effects of free convection and forced convection, it is apparent that free convection is negligible. In order to obtain free convection accurately, one needs to analyze a 180° or 360° sector, which is significantly more computation for a number that is 0.5% of the final result. Therefore, using the reduced sector and neglecting free convection is a justifiable assumption.

Back-side Radiation

Radiation of heat from the nozzle backside wall into the atmosphere is another factor of rocket nozzle heat transfer that is neglected in this thesis. In order to justify that this is a correct assumption, the effects of radiation at the throat were compared to the nozzle heat flux inside the thrust chamber at the throat. Radiation heat flux for this environment can be characterized by Eqn.(41).

$$q'' \approx \varepsilon\sigma {T_s}^4 \tag{41}$$

Where sigma is the Stefan-Boltzmann constant equal to 5.67×10^{-8}. This is the Stefan-Boltzmann law that takes into account emissivity for non-blackbodies. The radiation from the backside wall is not an enclosure problem, but if enclosure effects were taken into account, net radiation heat loss would actually be lower. The estimate used for radiation heat flux in this thesis is conservative assuming a correct surface temperature. Electrodeposited nickel can have an emissivity as low as 0.03 when manufactured. However, rocket nozzle materials are normally polished in order to increase the emissivity coefficient, where emissivity of copper and nickel for this rocket nozzle are both 0.9. Since no material emits more than a blackbody, it is not possible to have more radiation (a higher emissivity) than a blackbody, and so using 1 as the emissivity while also neglecting incoming radiation from the environment yields the maximum possible heat flux from the nozzle. Using Eqn. (41), the jacket heat flux from radiation at the throat is equal to 5.67 W/m^2, which is extremely small compared to the throat heat flux of 66.42 MW/m^2 at the hot gas side wall. Therefore, effects of back-side radiation are negligible.

Radiation of High Temperature Gas

Introduction to Chemiluminescence and Incandescence

Radiation is a form of medium-less heat transfer via photons. In reacting high-temperature gas, light is emitted through two mechanisms, incandescence and chemiluminescence. Incandescence, also known as thermal radiation, is the light emitted by a high-temperature gas. The spectral distribution can be described approximately using Planck's law. The most probable frequency and wavelength of the emitted radiation is described by Wien's displacement law. The overall radiation is described by the Stefan-Boltzmann law. The random thermal motions of matter and their collisions result in incandescence.

Chemiluminescence is the emission of light by atoms, molecules, or radicals during a chemical reaction. Some energetic chemical reactions, such as combustion reactions, can have products that are at an electronically-excited state. The product that is in this electronically-excited state then decays to ground state, which results in giving off a photon. This transition to the ground state can be through an allowed transition (which is similar to fluorescence) or a disallowed transition (which is similar to phosphorescence). Chemiluminescence, however, does not involve pre-absorption of photons to give off later on after reaching the excited state, since the atoms entered the excited state via a chemical reaction. In theory, a photon is emitted for every atom that decays from excited state to ground state; however, not all atoms transition to ground state directly via photon emission.

Chemiluminescence in combustion can be exemplified using the radicals CH* and OH*, which are products of combustion reactions. The intensity of the OH* chemiluminescence

signal is proportional to the heat release rate, or to the rate of the chemical reaction. This property is exploited in experiments by employing the measurement of the OH* or CH* intensity to perform laser-diagnostics of the local flame front. As noted by Lauer et al. [57], integrated emissions from OH* or CH* are fairly reliable measures of the integrated heat release. However, Lauer and Sattelmayer [58] demonstrated that spatially-resolved heat release rate of turbulent flames cannot be obtained from chemiluminescence.

Because of the different processes involved, the characteristics of chemiluminescence can be vastly different than incandescence. Whiles Wien's displacement law predicts a wavelength of approximately 1300nm for a 2200K gas, a 2200K hydrogen flame emits mostly in the narrow band of 305nm to 320nm (e.g. see Fig. 2 in Lauer, et al. [57]). In hydrogen flames, OH* is the only source of chemiluminescence, with narrow peaks at 285nm and 310nm. In methane flames, other sources of chemiluminescence are present, such as a narrow CH* signal at 390 and 430nm, as well as a narrow signal from C_2*; these narrow signals are overlaid on top of a broadband emission from CO_2.

Despite their importance in other fields, chemiluminescence is not considered in this thesis. The narrow emission-bands of these signals are less significant in the liner heat transfer characteristics compared to incandescence. Accurate prediction of their emissions is based on accurate modelling of the turbulence-radiation interactions, an interaction for which there is no model in Star-CCM+. The concept of chemiluminescence is introduced in this thesis simply to exemplify that accounting for all the photon emissions in a rocket nozzle is not straightforward.

Radiation Study of High Temperature Gas in a Rocket Nozzle

Thermal radiation consists of three primary effects: Radiation between surfaces, radiation from surfaces to the gas, and radiation from gases to gases. The thrust chamber is essentially a pipe with a closed end (the injector baseplate) and an open end (the thrust chamber exhaust). Since the nozzle wall is the only surface, the surface-to-surface radiation is fairly minimal in the current configuration. Surface-to-surface radiation improves heat transfer between locally hot and locally cold regions in the liner wall and effectively increases lateral heat conduction along the wall (but at longer ranges than heat conduction). The more dominant effects in the current study are the gas-to-surface and gas-to-gas radiation effects. Hence, it was necessary to consider thermal radiation with participating media and the intermediate step of considering only surface-to-surface radiation was skipped entirely.

Irradiation, or the rate at which radiation is incident upon a medium, can be divided into three factors, reflectivity, emissivity, and transmissivity which must sum to unity as in Eqn. (42).

$$\varepsilon + \rho + \tau = 1 \tag{42}$$

An absorption coefficient can be defined using Beer-Lambert law, which relates the attenuation (absorption) or light to the properties of the material through which the light is travelling. The Beer-Lambert law is given in Eqn. (43).

$$\tau = e^{-\kappa l} \tag{43}$$

Where κ is the absorption coefficient, and l is the characteristic length. The characteristic length for an arbitrary shape of volume V with radiation to a surface of area A is can be estimated by using Eqn. (44). [Table 13.4 Incropera and Dewitt]

$$l = 3.6\frac{V}{A} \tag{44}$$

The emissivity of water vapor, the fluid that is most present in the nozzle after combustion, is 0.6 (Fig 13.16 Incropera and Dewitt), yielding a transmission coefficient of 0.4. The volume of the truncated thrust chamber is 166.09in^3, and the surface area of the nozzle liner is 177.551in^2. Using this volume and area to find the characteristic length, this gives an absorption coefficient of 0.24in^{-1} (9.6 m^{-1}).

In order to determine the effects of radiation inside the nozzle, three simulations on the baseline configuration were run that included radiation effects inside the thrust chamber. Initially, an absorption coefficient of 9.5 m^{-1} was used. To test sensitivity of the problem to radiation effects, additional simulations using absorption coefficients of 0.95 m^{-1} and 95 m^{-1} were also run. An absorption coefficient of 95m^{-1} is fairly representative of an absorption coefficient in a thrust chamber where both carbon dioxide and water vapor are present (for example in a LOX/RP-1 rocket).

Star-CCM+ accounts for participating media effects by using the Discrete Ordinate Method (DOM). Hence, the model in Star-CCM is titled Participating Media Radiation (DOM). The accuracy of the DOM approach increases with increasing number of ordinate sets. In this work, the number of sets was left at the default value of 4 sets. The gray thermal radiation model was used since the specular properties are difficult to determine for these conditions (>100 bar). Star-CCM+ treats the thermal radiation effects in participating media in the bulk sense, in that Star-CCM+ accounts for it in the gas mixture, and not individual gases in the

mixture. Hence, the absorption coefficient and scattering coefficients are applied to the entire hot gas. This limitation is important because, for example, the effects of an infrared absorbing film in an otherwise transparent gas would not be captured by this approach. This effect is not a concern in the current configuration because the hot gas is primarily polar water vapor molecules, which is infrared absorbing, whereas the hydrogen film at the walls is non-polar and relatively transparent. However, Star-CCM+ would incorrectly treat the hydrogen film as an absorbing gas and is not well suited for simulations with varying species concentrations with gas components that have vastly different radiation characteristics.

Boundary Conditions

For boundary surfaces, the radiation boundary type is classified in Star-CCM+ according to Table 5.

Table 5: Boundary Classification for Radiation Model in Star-CCM+

	Boundary Type			Specify			
Boundary Condition	Closed	Open	Inactive	ε	ρ	τ	T_{rad}
Inlet: mass flow, stagnation, velocity		**X**		**X**	**X**	**X**	**X**
Outlet: pressure, flow-split		**X**		**X**	**X**	**X**	**X**
Wall	**X**			**X**	**X**	**X**	
Symmetry plane			**X**				
Cyclic			**X**				
Baffle	**X**			**X**	**X**	**X**	

Symmetry boundary conditions and cyclic boundary conditions (periodic boundaries) are non-participating and do not require any specifications. Closed and open boundaries, however, require specification of the surface emissivity, reflectivity, transmissivity, and radiation

temperature. Open and closed refers to the flow classification and not whether the boundary is open/closed to radiation flux.

The surface emissivity of the inlet was 0.5 with a radiation temperature of 800K (to represent the temperature of the baseplate). It is unclear what the appropriate value for the surface emissivity should be for the porous faceplate, although diffuse reflections are expected because of the porosity. Because of this, an emissivity of 0.5 was assumed.

The nozzle is truncated so the radiation propagating back upstream from the gases at the diverging portion of the thrust chamber is not well captured in our model. However, the exhaust gases are cooler than near the throat because of the expansion in the diverging portion of the converging-diverging nozzle. Additionally, in space-vacuum, the background radiation temperature is low. At ambient conditions, the ambient radiation is negligible compared to the radiation emitted by the hot gases in the thrust chamber.

At the pressure outlet, the radiation temperature was set to ambient 300K, but the emissivity was set to 0 and transmissivity was set to 1 so that the radiation at the pressure outlet is simply transmitted. The emissivity of the liner wall was set to 0.9 (a typical value for highly polished surfaces).

Results

The results of the liner temperature for these cases are plotted against the baseline configuration in Figure 9. These temperatures are directly underneath the cooling channel (at 0°). The wall heat fluxes at this location are compared in Figure 10. The contribution of the

radiation heat flux to the total heat flux is plotted in Figure 11. The solid lines in Figure 10 denote the total wall heat flux, whereas the broken lines denote only the radiation heat flux.

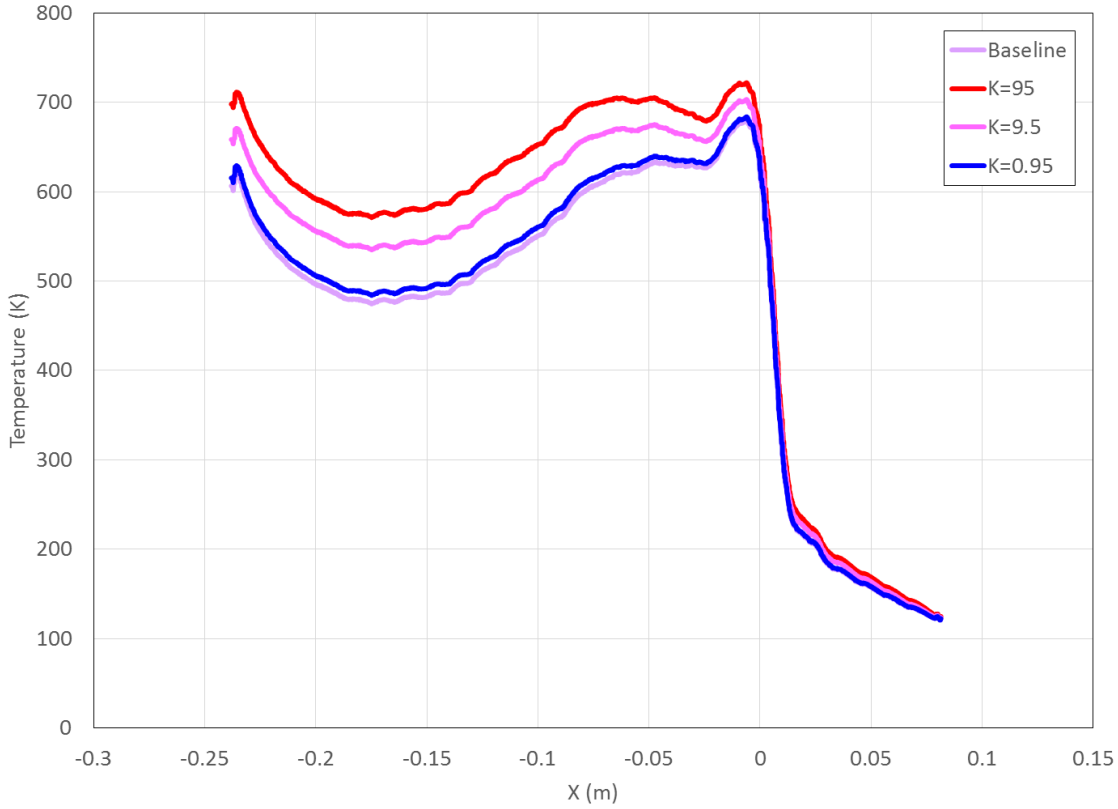

Figure 9: Comparison of Liner Wall Temperatures at 0° for Different Absorption Coefficients

With a higher absorption coefficient, the hot gas side wall temperature increases. The most pronounced differences are located in the upstream sections of the thrust chamber: this region is where the gases are hottest, as they are located immediately after combustion. After the nozzle throat, the flow is accelerated in the diverging section of the thrust chamber and the gas temperature drops rapidly. Hence, the temperature distributions are nearly the same after the throat for all cases, despite a two order of magnitude variation in the absorption coefficient.

The peak temperature near the throat increases from its value of 680K on the baseline simulation to 703K when the absorption coefficient is $9.5m^{-1}$. When the absorption coefficient is $95m^{-1}$, the peak temperature is 722K. Finally, when the absorption coefficient is $0.95m^{-1}$, the peak temperature is 684K. The change in temperature from baseline simulation without radiation is comparable to the simulation including radiation with the lowest absorption coefficient of $0.95m^{-1}$. The 4K difference is not significant and is on the order of the interpolation error in the simulation. At the nominal condition of $9.5m^{-1}$, the temperature increased by 23K, and 42K for the extreme condition with an absorption coefficient of 95 m^{-1}. The difference increased due to the inclusion of radiation effects are appreciable, however these results demonstrate that even without including radiation effects that the simulation results without including radiation effects reproduces the most important characteristics of the heat transfer in the thrust chamber. That is, the temperature profile is similar for all four cases.

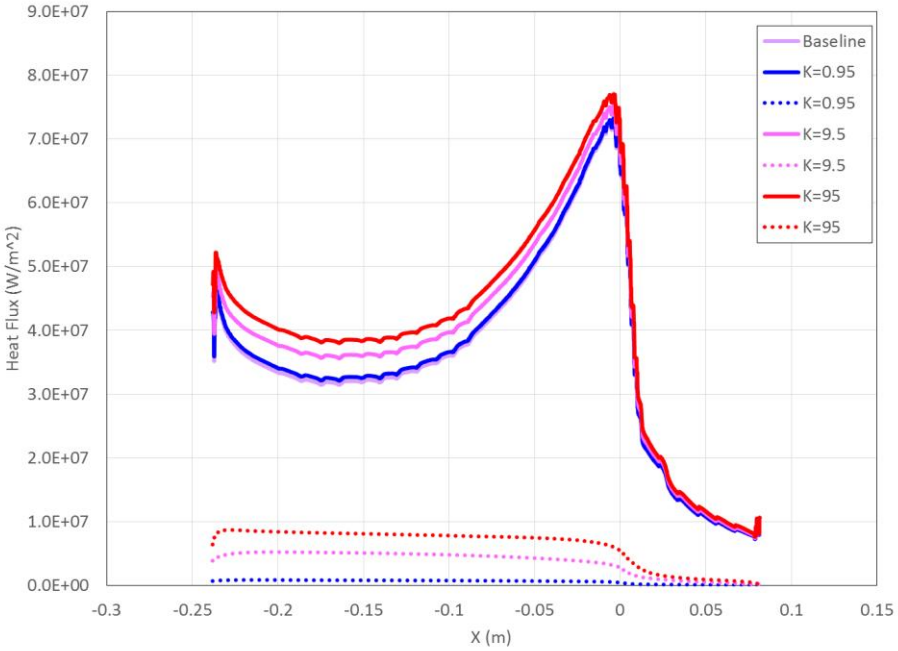

Figure 10: Comparison of Liner Heat Flux for Different Absorption Coefficients

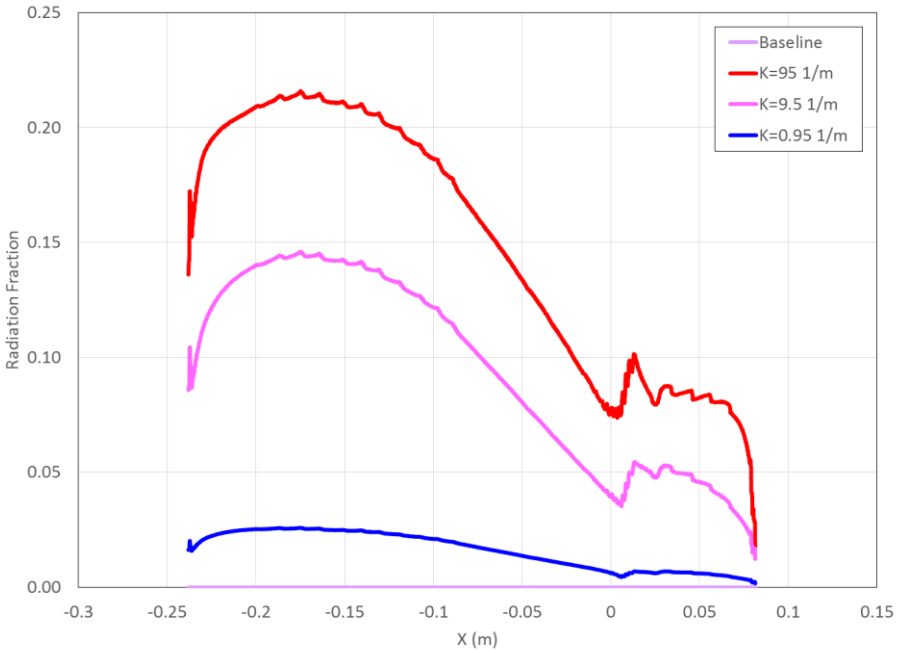

Figure 11: Comparison of Radiation Fraction for Different Absorption Coefficients

With the extremely high absorption coefficient of $95m^{-1}$, the radiation heat flux did not exceed 25% of the total heat flux. For the nominal case of $9.5m^{-1}$, the fraction did not exceed 15%. Most of the radiation occurs at the upstream end of the thrust chamber (before X=-0.1m). This region is where the combustion process occurs. Hence, the radiation heat flux in this region is over-predicted with this type of model; in reality, the hot gases are still undergoing combustion in this region and the local gas temperature can be significantly below the flame temperature. When X > -0.1m, the radiation heat flux is less than 10% of the wall heat flux. Near the throat, radiation counts for 5% of the heat flux. Since the heat transfer and temperature profile are evaluated after X = -0.1m for all designs including the baseline configuration and the film cooling design, it can be asserted that the fraction of total heat flux attributed to radiation heat flux does not exceed 15%, and does not exceed 5% at the throat of the nozzle. Despite the high gas temperatures, and even though the radiation heat flux is on the order of $5MW/m^2$, the radiation heat flux is a small contribution to the overall heat flux because it is dominated by convective heat transfer near the throat. Since these percentages are low, it is valid to neglect radiation heat flux within the nozzle for X > -0.1m. The convective heat transfer at the throat is high because of the converging contour of the nozzle; the curvature enhances the heat transfer coefficient. More importantly, the regenerative cooling channels are extremely effective and are able to cool the liner despite the immense heat flux from both radiation and convective heat flux. For an un-cooled nozzle extension, where regenerative cooling cannot exist, radiation heat flux is not cooled by regenerative cooling and so is a significant issue with un-cooled nozzles. Rajagopal [59] analyzed the effects of radiation

heat transfer on a nozzle without regenerative cooling and found that the net radiative heat transfer is low since the nozzle wall temperature reaches close to the hot gas temperature. With regenerative cooling, net radiative heat transfer increases due to the increasing temperature difference.

To illustrate the effect of radiation heat flux on the total heat flux with varying temperature differences, a surface energy balance on the liner wall can be written as Eqn. (45).

$$q"_{cooling} = q"_{convection} + q"_{radiation} \tag{45}$$

The $q"_{regen}$ is the heat flux on the liner wall driven by the regenerative cooling. This heat flux is equal to the incoming heat load from the convective and radiative heat transfer.

$$q"_{regen} \approx h_{regen}(T_{H_2} - T_{gw}) \tag{46}$$

Equation (46) posits that the regenerative cooling is proportional to the convective heat transfer coefficient and driving temperature difference. Realistically, this relationship should include the temperature difference between the coolant temperature and the wall temperature inside the regenerative cooling channel. However, this proposition neglects conduction through the liner wall, which is why the relationship is only proportional, not equal, and why the driving temperature difference is between the coolant and the hot gas-side wall temperature.

The importance of this relationship is that T_{gw} is somewhere in-between T_{H_2} and T_∞ (T_∞ being temperature of the hot gas itself); one interpretation is that T_{gw} is controlled by the regenerative side heat transfer coefficient. It actually depends on the heat loading from the liner side, but the regenerative cooling must be enough to balance the heat load to maintain

thermal equilibrium. Similarly, the convective heat load on the nozzle liner is proportional to the convective heat transfer coefficient on the inside liner and the driving temperature difference, which is the difference between T_{gw} and T_{∞}, Eqn. (47).

$$q"_{conv} \sim h_{throat}\left(T_{gw} - T_{\infty}\right) \tag{47}$$

However, the radiation heat load is proportional to the difference of temperatures to the fourth exponent, Eqn. (48).

$$q"_{conv} \sim \sigma\left(\varepsilon_{liner} T_{gw}^4 - \varepsilon_{hg} T_{\infty}^4\right) \sim T_{gw}^4 - T_{\infty}^4 \tag{48}$$

The temperature difference can be factored using the identity, Eqn. (49).

$$\begin{aligned}(a^4 - b^4) &= (a^2 - b^2)(a^2 + b^2) = (a - b)(a + b)(a^2 + b^2) \\ &= (a^3 + a^2 b + a b^2 + b^3)\end{aligned} \tag{49}$$

Equation. (49) shows that the backside cooling is linear in temperature difference, and the convective heat load is linear in temperature difference. The radiation heat load is non-linear, but with the linear component factored out $(a - b)$, there is an additional weight factor of $(a + b)(a^2 + b^2)$: as T_{gw} becomes smaller, the weight factor becomes smaller. However, the weight factor remains greater than unity since $T_{gw} > 1K$.

However, the percentage of the heat flux attributed to radiation is more strongly dependent on heat transfer coefficient than the convective heat flux. When heat transfer coefficient is very high, such as near the nozzle throat, the total heat flux is dominated by the convective effects. The fraction of heat transfer due to radiation can be estimated by

$$rad\ \% \sim \frac{\sigma(T^4 - T^4)}{h(T - T) + \sigma(T^4 - T^4)} = \frac{\sigma(T + T)(T^2 - T^2)}{h + \sigma(T + T)\left((T^2 + T^2)\right)} \tag{50}$$

Emissivity was assumed to be 1, which is a conservative estimate, or when heat transfer coefficient is bigger than $\sigma T_{\infty}^{3} = 5.67x10^{-8} * 3750^{3} = 2990\ \frac{W}{m^2K}$. The heat transfer coefficient at the throat for the baseline design at 0.023kg/s per channel mass flow rate with an absorption coefficient of 9.5m^{-1} was approximately 23 000W/m^{2}K; the heat transfer coefficient vs X is depicted in Figure 12. This paired with Figure 10 shows that when heat transfer coefficient is low, the percentage of heat flux attributed to radiation is higher, and vice-versa. Using the temperatures of 700K for $T_{gw}$and 3750K for T_{∞}, the percentage of heat flux attributed to radiation is 14%, which is higher than what was found in the simulation since for this, an emissivity of 1 was assumed. With an emissivity of 0.6, the heat flux attributed to radiation is 9%.

This calculation can be simplified further. T_{gw} is usually an order of magnitude less than T_{∞}so that T_{gw}^{4} is 4 orders of magnitude less than T_{∞}^{4}, which means that $T_{gw}^{4} \ll T_{\infty}^{4}$. Because of this, the radiation ratio is determined primarily by the emissivity of T_{∞}: if the emissivity of copper is varied from 0 to 1, it is not significant, and the same radiation heat flux attribution percentage is attained of 13.8%. It is important to note that this does not mean T_{gw} is not important.

$$rad\ \% \sim \frac{\sigma \varepsilon T^{4}}{hT + \sigma \varepsilon T^{4}} = \frac{\sigma \varepsilon T_{\infty}^{3}}{h + \sigma \varepsilon T_{\infty}^{3}} \tag{51}$$

Using this equation with an emissivity of 1, the percentage is 11%. With an emissivity of 0.6, the percentage is 7%. This estimate will under-predict the radiation rate since all other terms that were neglected were positive contributions, but it is useful for obtaining a quick order of

magnitude calculation. These equations would be useful in preliminary analysis before using numerical analysis in order to get an order of magnitude estimate to assess the importance of radiation effects.

Using a reference temperature of 3750 K for convenience, the hot gas side heat transfer coefficient for the baseline and radiative cases are given in Figure 12 for the baseline simulation (which neglected radiation effects) and the simulation with gray thermal radiation using an absorption coefficient of (9.5 m^{-1}). The curves are nearly identical for both cases, which demonstrates that the convective heat transfer coefficient is not affected by the participating media; that is, the net heat flux on the liner is a simple superposition of convective and radiative effects.

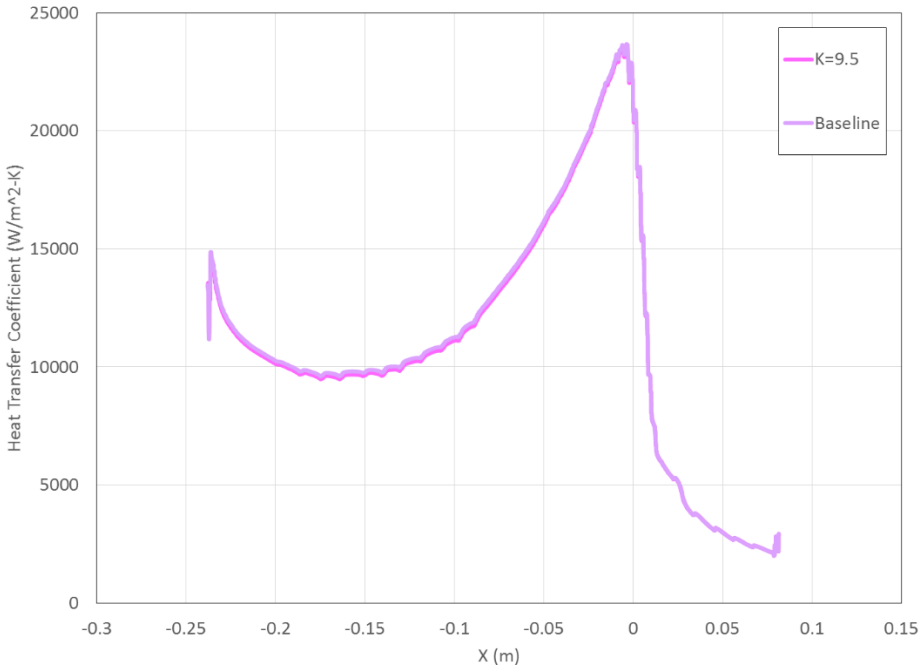

Figure 12: Hot Gas Side Heat Transfer Coefficients

The radiation fraction was calculated using Eqn. (52), which is slightly more detailed than the previously given Eqn. (49), by varying the hot gas side heat transfer coefficient and emissivity of the hot gas; the results are plotted in Figure 13. The calculation was done assuming $T_{gw}$of 700K and T_{∞} of 3750 K, and 0.9 for the emissivity of liner (varying the liner emissivity from 0 to 1 had no significant effect). One curve is calculated by keeping the hot-gas emissivity fixed at 0.6 and varying the hot-gas heat transfer coefficient. The other curve is calculated by keeping the htc fixed at 23000 W/m^2-K and varying the emissivity of the hot gas.

$$rad\ \%\sim\frac{\sigma\left(\varepsilon_{cu}{T_{gw}}^{4}-\varepsilon_{water}{T_{\infty}}^{4}\right)}{h\left(T_{gw}-T_{\infty}\right)+\sigma\left(\varepsilon_{cu}{T_{gw}}^{4}-\varepsilon_{water}{T_{\infty}}^{4}\right)} \tag{52}$$

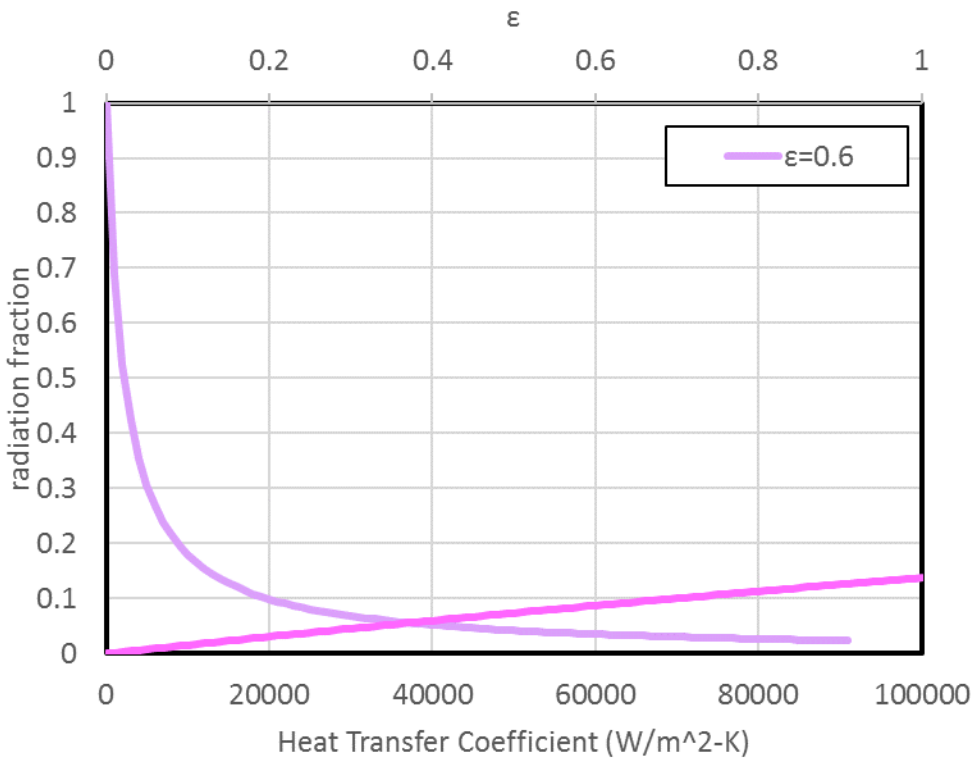

Figure 13: Radiation Fraction Sensitivity to HTC and Emissivity

Finally, all parameters were held fixed except for the liner wall temperature, which was varied from 300K to the zero crossing of the net heat flux. The result is plotted in Figure 14. Although this plot is based on the rough proportionality calculations, it demonstrates that the radiation fraction decreases with the liner wall temperature, whereas the liner wall temperature decreases only if the regenerative cooling on the backside is improved. This outcome may be counter-intuitive and non-obvious since the convective heat load increases linearly with the driving temperature difference, whereas the radiative heat load increases with the difference of temperatures raised to the fourth exponents.

On the other hand, the radiative heat load still increases with colder liner wall temperatures in addition to the convective heat load. Thus, lowering the liner wall temperature becomes increasingly difficult as both the convective and radiative heat loads increase. However, the total heat load on the nozzle becomes increasingly dominated by convective loads with colder liners and it is more justifiable to neglect radiative effects in the design when dealing with cold liners.

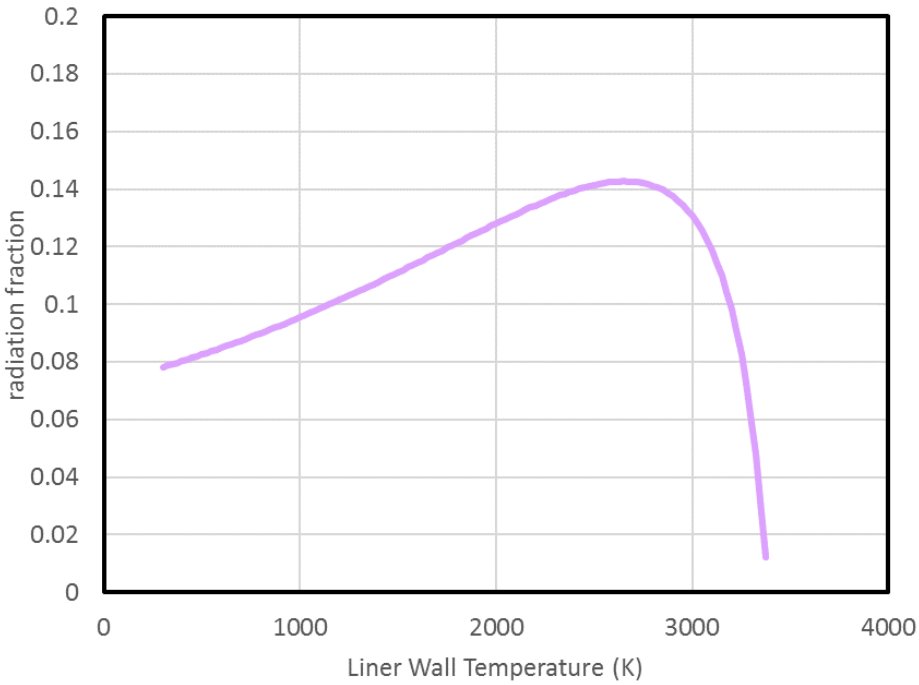

Figure 14: Radiation Fraction Sensitivity to Liner Wall Temperature

CONFIGURATION 1: 1.8° WEDGE

For this preliminary configuration, only internal cooling was considered. The configuration of the internal cooling was modelled after Wadel's experimental setup using the 89kN combustion chamber nozzle contour. As previously mentioned in the literature review, Wadel tested several High Aspect Ratio Cooling Channel (HARCC) configurations. In accordance with Wadel, the cooling channels have an aspect ratio of 5. This baseline configuration was first completed as a 1.8° wedge. The first configuration was used in order to measure the accuracy of a 1.8° sector, and used Wadel's baseline temperature distribution mapped onto the bottom wall of the liner.

Geometry

Since 3D simulations are difficult to model due to their computational complexity, it was important to attempt to make the 3-dimensional simulation as "2-dimensional" as possible. To do this, the entire nozzle including the hot gas was modelled in a 3.6° sector, which included two half channels in order to include interaction between each channel while still minimizing computational power. However, when including the hot gas in the mesh, the solver was unable to configure the wedge point at the center of the nozzle. This phenomenon is depicted in Figure 15.

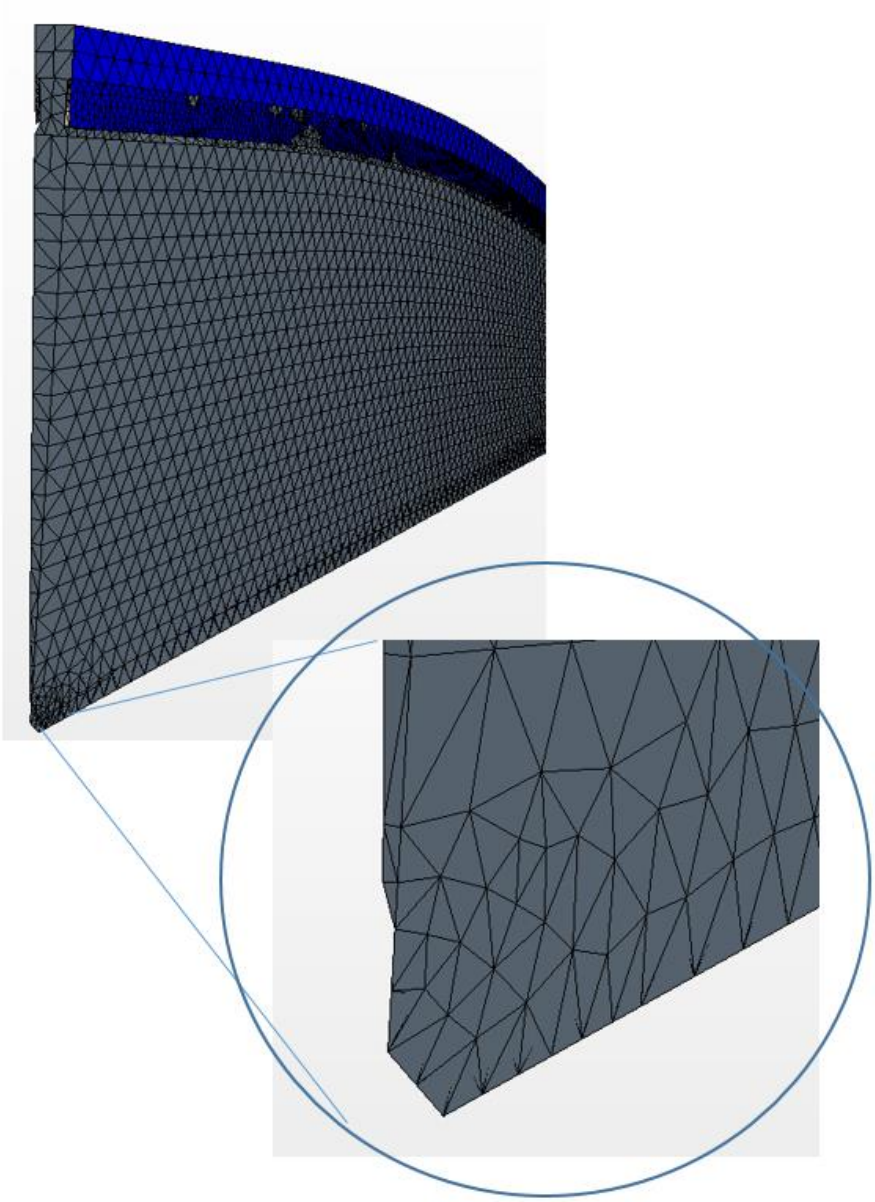

Figure 15: Wedge shows evidence of malformed mesh

This also occurred with a 1.8° wedge piece that included one half-channel. Even if the cell count was drastically increased, the wedge point could not be resolved. This is because, with a wedge, the point that coincides with the centerline of the nozzle (the apex of the wedge) requires a finite number of cells in its representation: 1, 2, 3, etc. Increasing cell count does not remediate

this issue, as increasing cell count would end up increasing skewness angle at the wedge point. If there are two cells at the point, for example, the half angle must be subtracted from 90°. For example, in Figure 16, the two cells making up the corner mesh would have inner angles of A and B respectively.

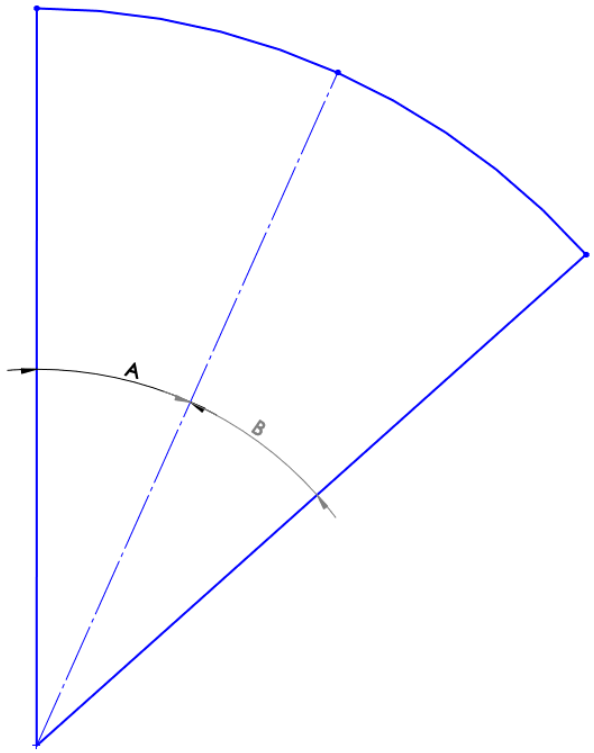

Figure 16: Schematic of Wedge Corner

Subsequently, the skewness angle for the cell associated with angle A would have a skewness angle of 90°-A (and 90°-B for the cell associated with B). As cell count increases, the angle between each cell at the wedge point will decrease, which in turn increases skewness angle. For n cells formed inside a sector of angle θ, the angle subtended by A is roughly θ/n and the skewness angle is roughly 90°-θ/n. As n increases, the skewness angle also increases,

resulting in more skewed meshes. Hence, care should be exercised with geometry containing sharp corners because these geometric features inherently will result in skewed meshes. The skewness problem cannot be alleviated by increasing the cell density. Even worse, the skewness problem restricts the simulation to only coarse meshes that do not these skewed cells, thereby limiting the resolution attainable for that geometry.

In order to solve this issue, the hot gas of the combustion chamber was modelled on its own in a larger 36° section. This angle did not produce the same meshing issues as 1.8° or 3.6°. This angle was determined by analyzing the geometry of the section with respect to its relation with skewness angle. In general, the skewness angle can be predicted by taking the angle of one cell at the wedge point and subtracting it from 90°. This method shows that skewness can be estimated from the geometry. With a 36° section, the minimum skewness angle due to the wedge point is 72°. This skewness angle was calculated by subtracting half of 36° (to account for 2 cells at the wedge point) from 90°, which amounts to 72°, which is more preferred than the skewness that would result from 1.8° sector.

For this particular configuration, however, another solution was used. Since the temperature profile and heat transfer coefficient along the liner wall are known from Wadel et al., the hot gas does not actually have to be modelled when using these known profiles. Instead of including the entire hot gas, only the channel, liner, and jacket (or outer wall) were included, shown in Figure 17. This geometry does not have the same skewness issues as a wedge shape since there is no final wedge point. The temperature and htc coefficient profiles were mapped onto the inner wall of the liner (also known as the hot gas side wall) of the 1.8° sector.

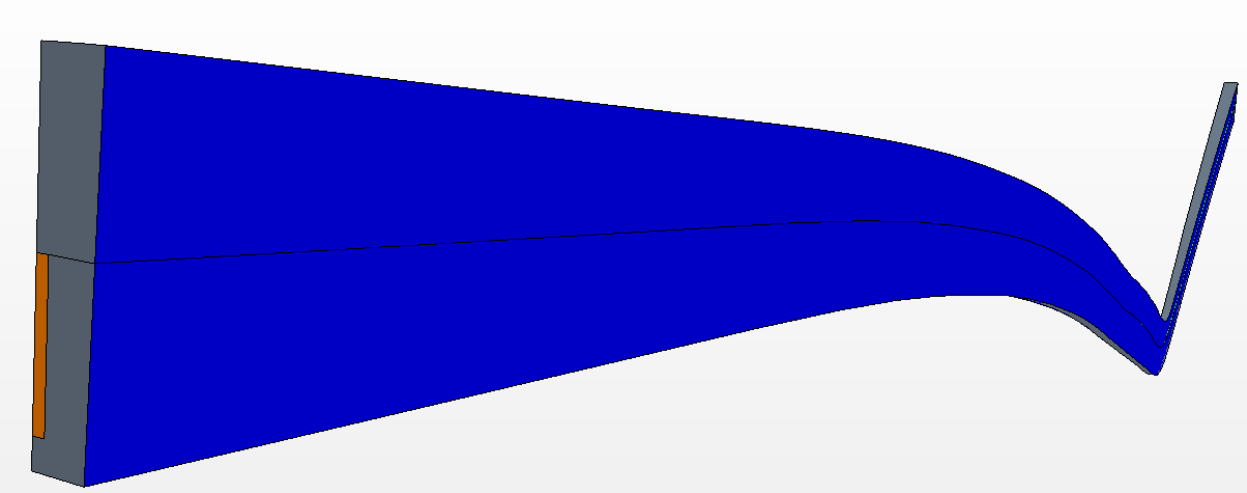

Figure 17: 1.8-degree nozzle section includes liner, channel, and jacket

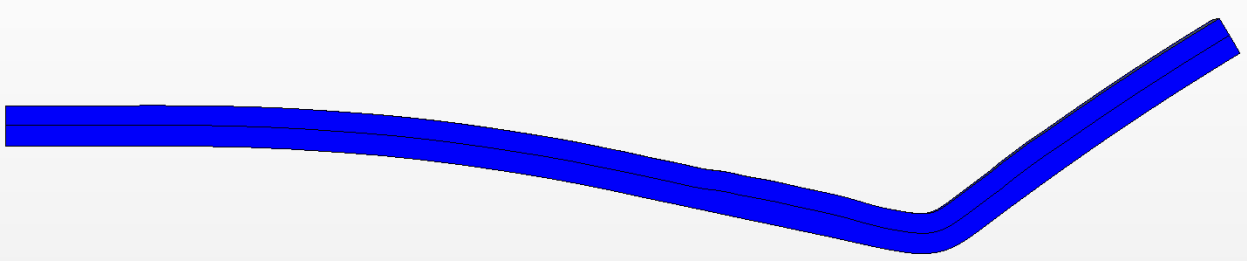

Figure 18: 1.8-degree nozzle section

Mesh

This design, since it does not include the hot gas, was meshed entirely differently from the other designs. The entire mesh remained polyhedral, with prism layers in the boundary layers of the fluid regions. The global base size was specified as 0.05in, with a surface size of minimum 15% to maximum 100%. This is finer than the 36° sectors since this configuration did not deal with the large expanse of hot gas normally present. Regional changes based on the channel, liner, and jacket were completed using volumetric controls. Total cell count is 862,438. Approximately 80% of this cell count is within the channel.

Since a vast majority of the heat transfer occurs within the cooling channels, the channels were meshed with a high cell density. The channel cell count was 708,883, with a custom base size of 0.005in, or one-tenth of the global base size. The channel used 8 prism layers at a 20% of the base size and a stretching rate of 1.3 along the surfaces of the channel.

For the jacket, the base size was customized at 0.125in, as the density of the jacket mesh did not have to be high since most of the varied heat transfer took place within the liner and channel. All other aspects of the mesh were left at the global reference values. The cell count was 30,608.

The liner had to be able to accurately depict heat transfer between the thin wall that separates the channel from the hot gas. To achieve this, the base size was reduced to 0.12in. All other reference values remained at global values. The cell count was 122,947.

Governing Equations

Since this configuration did not need to model the hot gas, a complex chemistry and species transport model was not needed. However, it was still important to include the varied thermophysical properties of hydrogen.

Results: Configuration 1

The simulation was run at two different conditions. The first condition used a temperature profile from the baseline configuration of Wadel et al., while the second used the premixed adiabatic temperature profile from the configuration 0 injector simulation. From these temperature profiles, heat transfer coefficient was calculated and also applied to this 1.8° design. The simulation was run until convergence, or until the temperature at a probe point

varied less than 0.1K per 50 iterations; the probe point was placed at the center of the nozzle throat with coordinates (X,Y,Z) = (0,0,0).

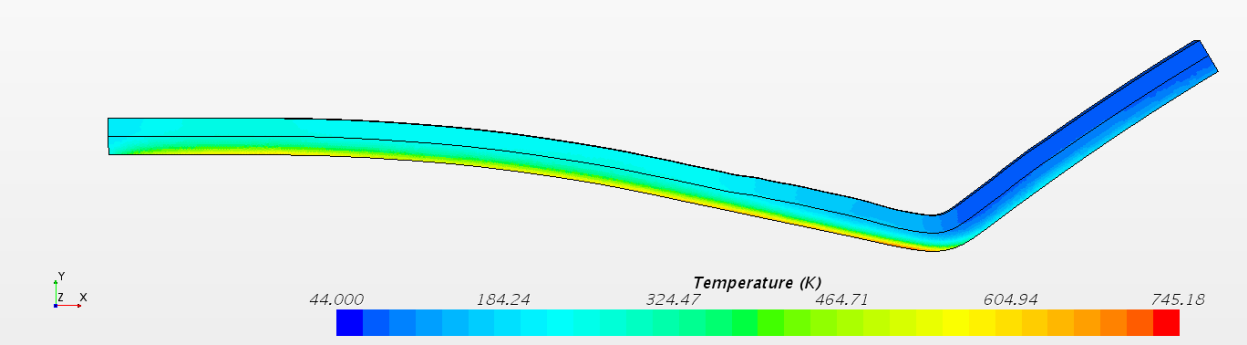

Figure 19: Temperature Distribution between Channels

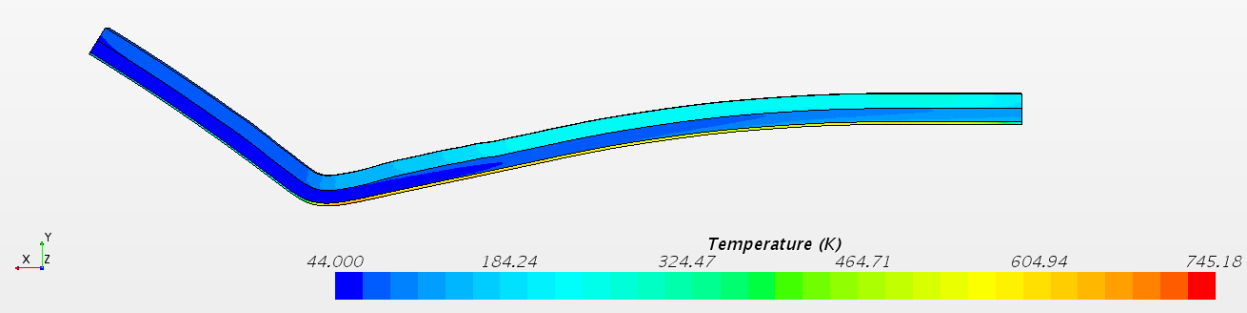

Figure 20: Temperature Distribution in Channels

The temperature profile pictured above is from the simulation that used the temperature profile of Wadel et al. that was used for their baseline configuration. This temperature profile is not the same as the benchmark temperature profile used by this author. Because of this, the quantitative temperature distribution varies compared with Wadel's Design 1. While the trends themselves are relatively similar, the actual results are not congruent with Design 1 because of the different hot gas wall temperature. However, this simulation still shows that 3-dimensional simulation of a rocket nozzle wall is possible using different methods to minimize cell count while maintaining accuracy.

This configuration is only possible with a known heat transfer coefficient at the wall. This sort of geometry will work for such cases. However, the design which includes film cooling cannot have a known heat transfer coefficient. In order to ensure that all designs including the baseline are comparable, the larger section that allows for accurate meshing of the hot gas will be used for all further simulations.

CONFIGURATION 0: INJECTOR AND HOT GAS MODEL

The combustion chamber was modelled as the hot gas only, with special consideration for incorporating the injector at the inlet of the nozzle, as well as complex chemistry models. Rocket nozzles use a fuel injector to introduce the fuel to the oxidizer, and little research has been done to determine whether or not inclusion of the injector is necessary to model the correct cooling characteristics in the nozzle. Also, injector style varies between different rocket engines, and so it is important to monitor the effects of the injector in order to ensure that the results in this thesis are comparable across different rocket engines. The combustion chamber was run separately from the liner, jacket, and channels in order to minimize computational time. A temperature profile was extracted from the results.

Geometry

The injector head was reverse-engineered based on available published information. The injector used at NASA Lewis was a flat-faced injector with 91 LOX posts. All fuel flowed through the porous baseplate, manufactured by Rigimesh. It is known however, that soon after the injector for the RL-10 was manufactured to be conical and superior to a flat faced injector. The central spark igniter was not included, and modelled using the same LOX post (all 91 LOX posts have identical dimensions). The rest of the hot gas nozzle contour is the same as the contour described previously. The arrangement of the posts is based on a published schematic by Dranovsy (pg. 56 in Combustion Instabilities in Liquid Rocket Engines). This configuration is fairly common and gives the most important geometric parameters. The missing unknown parameter is the radial spacing between rows of injectors and any extra offset for the last row

since is important in some designs to not have the LOX impinge on the walls of the nozzle. Finally, the diameter of the LOX posts is needed. This thesis opted for 8mm ID and 9.5mm OD posts. These dimensions are based on an estimate of 1.5mm as a typical pipe thickness of the LOX posts. The injector geometry and mesh are pictured in Figure 21.

Figure 21: Injector Mesh and Geometry

Mesh

The final mesh cell count for the hot gas model was 1,314,446 cells. The mesh is a polyhedral mesh with 12 prism layers. The base size of the mesh is slightly smaller than other configurations at 0.15in. In order for the cell count to become progressively denser toward the injector head, volumetric controls were incorporated at intervals: X=-6.05in, -7.5in, and -8.5in.

Each section decreased the surface size from 0.15in to 1mm, 0.75mm, and 0.5mm, respectively. This cell density was chosen in order to properly and accurately model fuel mixing at the nozzle inlet. An additional volumetric control at the throat of the nozzle was included in order to properly model the change in static properties at the throat, where surface size was reduced to half the base size.

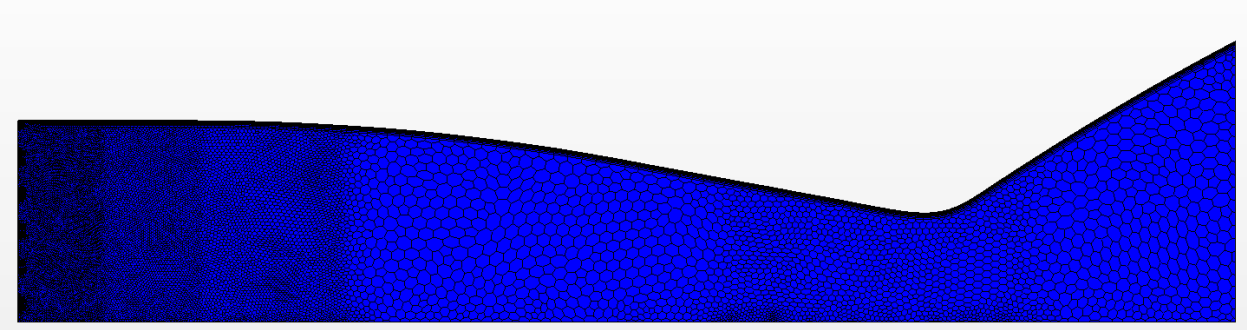

Figure 22: Final Injector Mesh

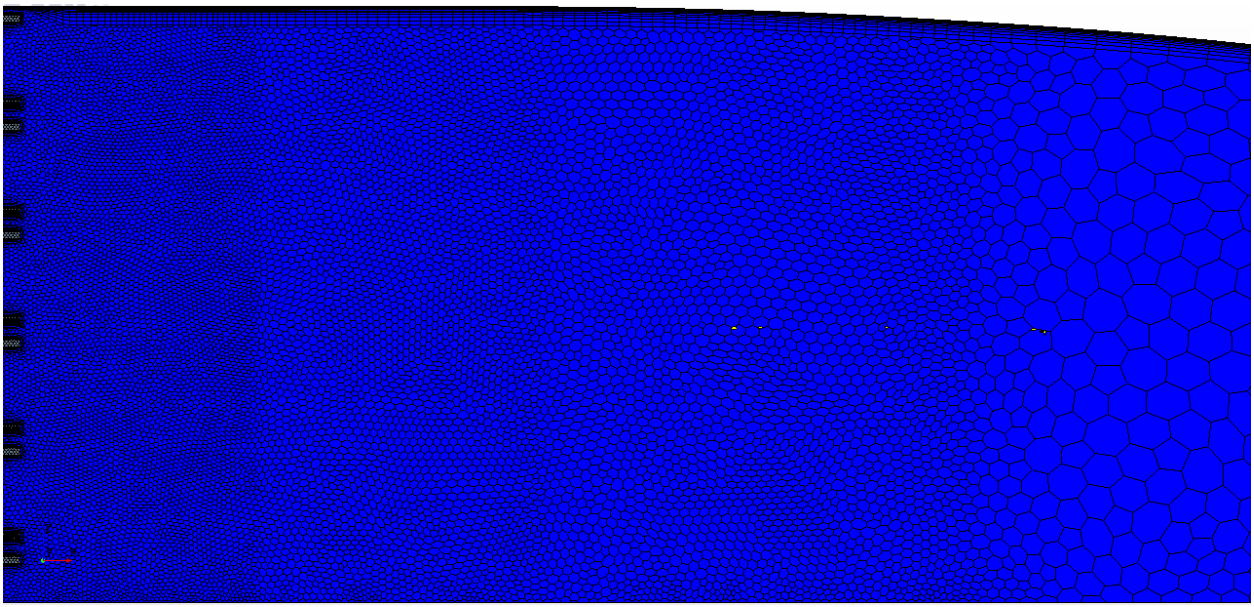

Figure 23: Mesh increases in cell density towards the injector

Results

The injector was run at four different conditions, with two factors varied. The temperature conditions were tested at both adiabatic and the wall temperature produced by Wadel. The Wadel wall temperature profile was based on their baseline configuration, which is not the benchmark temperature distribution for this thesis. Although it is not the benchmark temperature, the simulations are still valid, as they are the initial investigations into injector inclusion. These simulations are testing whether or not it is necessary to include the injector for accurate heat transfer measurements in the nozzle, and so regardless of the specified wall temperature, all the simulations used the same injector dynamics. Centerline properties were compared to analyze the congruency of each case.

The injector dynamics were also varied as either premixed or unmixed, meaning that two simulations ran combustion with a premixed flow upon injection, and two simulations ran with an unmixed flow upon injection. Each simulation was run for at least 3000 iterations in order to ensure convergence, or when temperature variation decreased below 0.5K per 50 iterations. The internal temperature distribution for each of the four cases is pictured in Figure 24, Figure 26, Figure 27, and Figure 29. Figure 28 and Figure 25 show the wall temperatures for the adiabatic conditions.

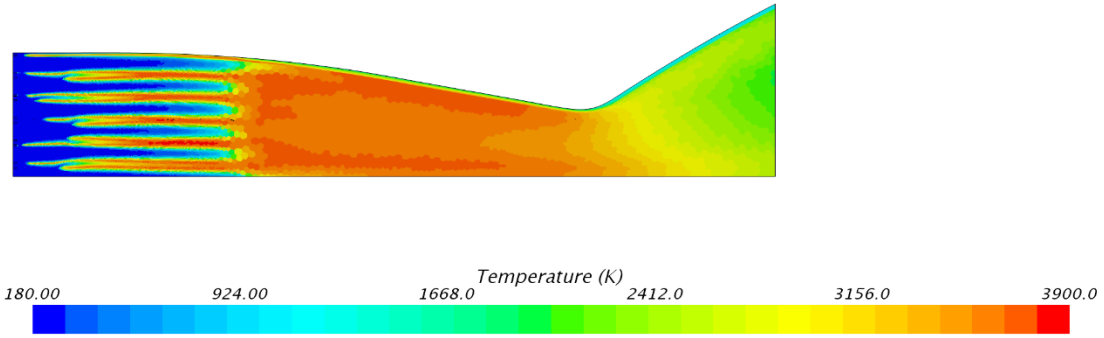

Figure

Figure 24: Injector Adiabatic Unmixed Temperature

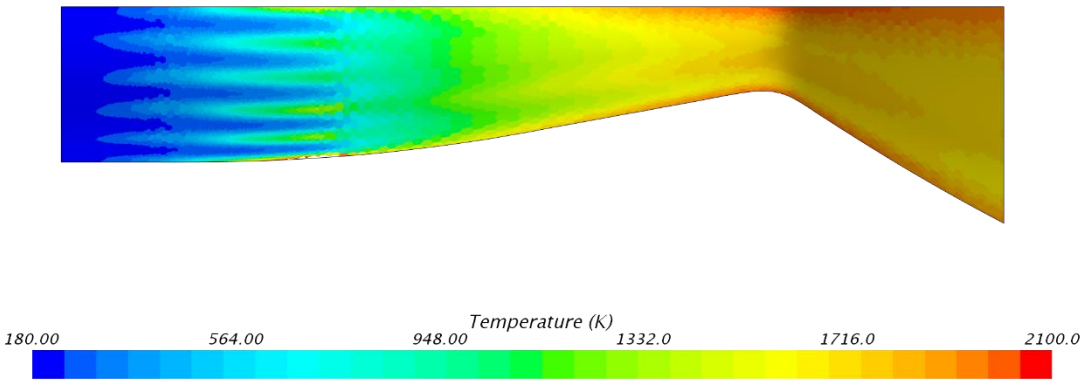

Figure 25: Injector Adiabatic Unmixed Wall Temperature

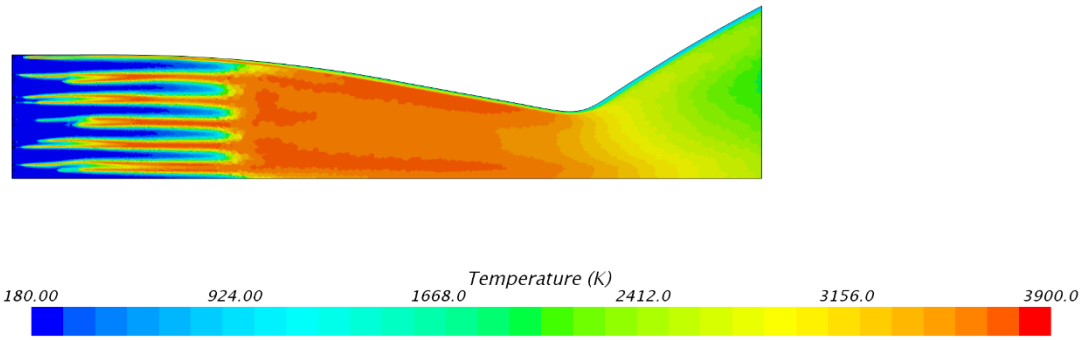

Figure 26: Injector Wadel Tw Unmixed Temperature

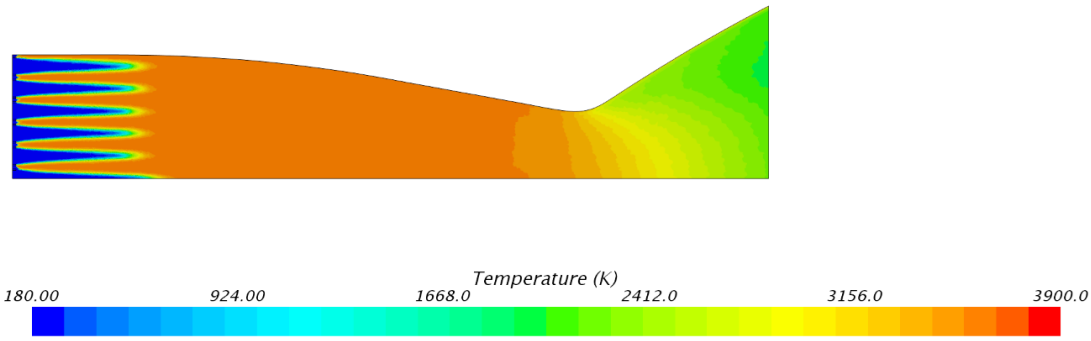

Figure 27: Injector Adiabatic Premixed Temperature

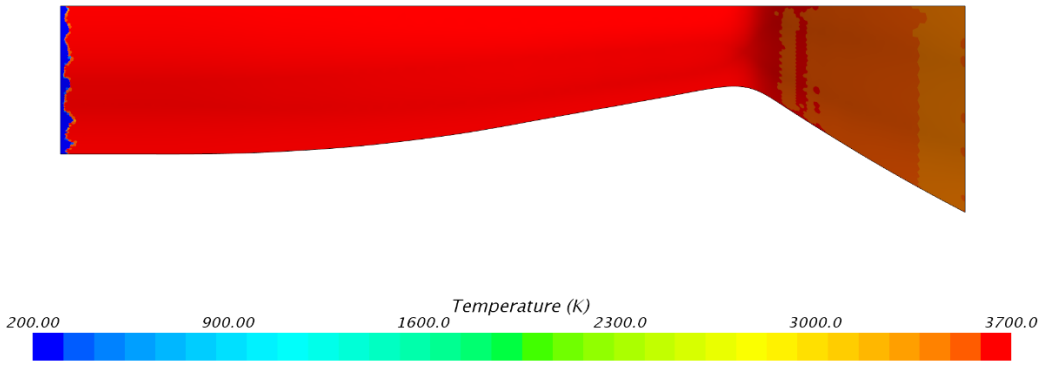

Figure 28: Injector Adiabatic Premixed Wall Temperature

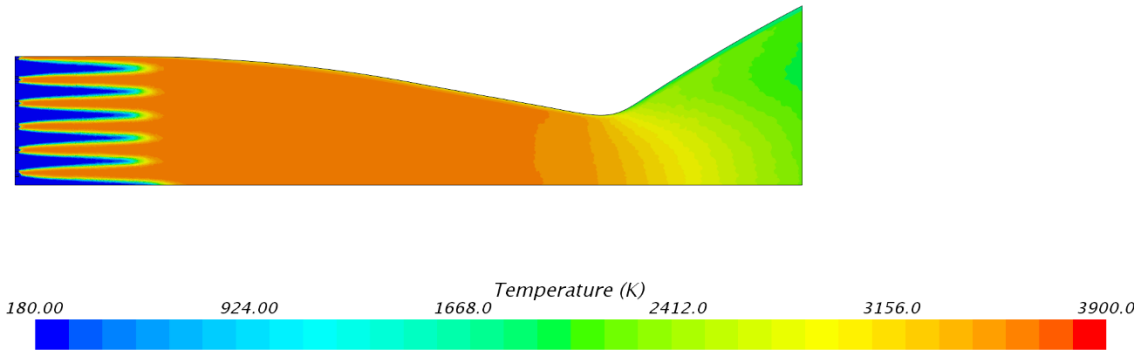

Figure 29: Injector Wadel Tw Premixed Temperature

Each condition depicts differing temperature distributions close to the injector. However, as all of the fuel burns, the temperature becomes relatively uniform across all cases. In the unmixed cases, particularly one that uses the data from Wadel for T_{gw}, a hydrogen film developed along the wall of the nozzle. This changed the wall temperatures significantly. The film is due to hydrogen not mixing well with the oxygen and attaching to the wall as a thermal boundary layer.

In order to determine where the injector and boundary conditions affect the temperature results in the hot gas, centerline properties were compared. Properties at the centerline are as far away from the wall as possible, and therefore illustrate the sensitivity of the nozzle to the inlet and boundary conditions. Static temperature (Figure 30), total temperature (Figure 31), and Mach number (Figure 32) were compared.

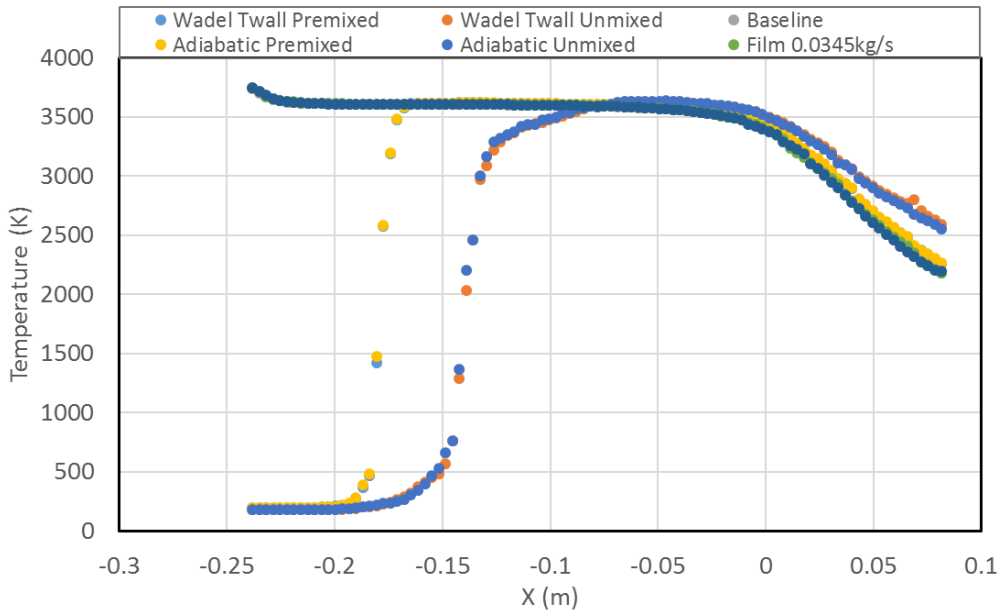

Figure 30: Centerline Static Temperature Comparison

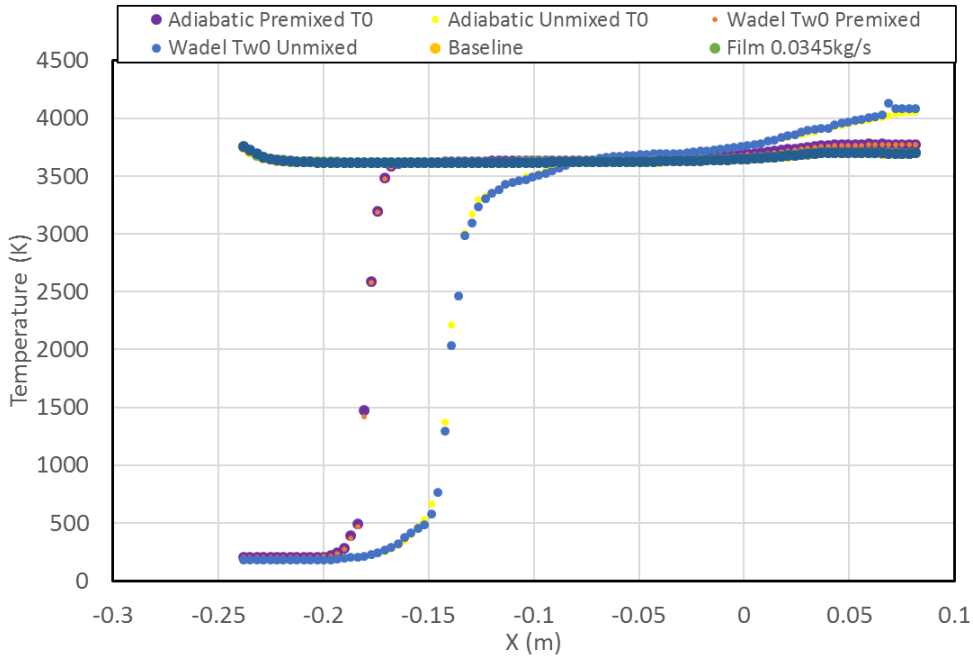

Figure 31: Centerline Total Temperature Comparison

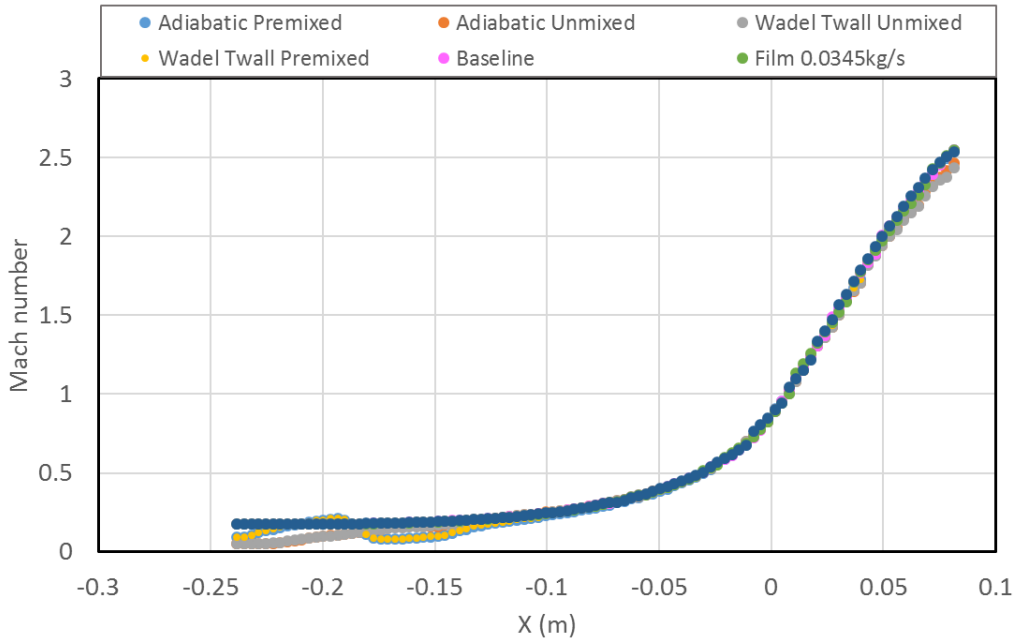

Figure 32: Centerline Mach Number Comparison

At first, the centerline properties are varied, especially temperature. The increased variation in temperature is dependent on whether or not the fuel and oxidizer were modelled as premixed or not premixed, but after combustion takes place, the temperature profiles are relatively the same. Variation in Mach number is less pronounced, but follows the same trend of becoming more similar further downstream of the nozzle. Since there is a large discrepancy in the temperature between x= -0.25m and x= -0.1m, this sector of the nozzle will not be considered in further analysis. The variation becomes virtually absent after X = -0.1m, or 0.1m upstream of the throat. All results from future simulations will be considered only after X = -0.1m so that results are comparable across engines that use different injectors.

INLET BOUNDARY CONDITIONS: ANALYSIS

Even though injector characteristics are not affecting the results beyond X=-0.1m, it is important to be able to specify the inlet boundary conditions for the simulation itself in order to model the hot gas accurately. Since the injector is not included in the domain of the baseline configuration and following configurations, the inlet boundary conditions must be able to accurately model that of the injector. This thesis uses inlet mass fractions and inlet temperature from Amato et al. However, inlet conditions can be modelled with increasing complexity, from complete oxidation to highly detailed kinetic mechanisms. Therefore, it is important to investigate the variations within each method in order to determine the validity of the assumption made by Amato et al.

Amato et al. [24] used an inlet static temperature of 3750K and mass fractions according to Table 6. Compared with the most detailed kinetic model, several species were not included in the reduced mechanism. These have been appended to the table (with zero mass fractions) for improved clarity and comparisons with other analysis following. Argon, Helium, and Nitrogen were left out of the table since they are not used in any of the designs in this thesis.

Table 6: Inlet Mass Fractions from Amato et al. [24]

Species	Mass Fraction
H	0.00246
H_2	0.05205
H_2O	0
H_2O_2	0
HO_2	0.90166
O	0
O_2	0.00313
OH	0.0407

Complete Oxidation

The simplest method of estimating the post-flame temperature is to use an assumption that is similar to complete combustion. In hydrocarbon fuels, complete combustion occurs when the reactants (fuel and air) are react completely into water vapor and carbon dioxide. The nitrogen in air is assumed to be inert and does not participate in the reactions. Since the concentrations or mass fractions of the product stream are known, an energy balance can be performed on the system and the temperature of the products can be determined (if the thermodynamic properties of the substances are known). For a reaction of only hydrogen and oxygen, complete combustion, Eq. (53), is much simpler, since all the reactants are converted into only water vapor.

$$2H_2 + O_2 \rightarrow 2H_2O \quad (53)$$

Complete combustion occurs only at stoichiometric conditions. For complete combustion of hydrogen in oxygen, exactly two moles of hydrogen must be provided for every mole of oxygen (or an oxidizer-to-fuel mass ratio of 8:1). If there is any excess fuel, there will be some leftover H_2 content in the product stream. If there is excess oxidizer, there will be remaining oxygen in the product stream. These conditions can be applied to engines that run either fuel rich or fuel lean conditions, creating similar effects. For fuel rich conditions, one can assume that complete oxidation of the fuel occurs, which is akin to assuming that all of the oxygen is consumed in the reaction and that no oxygen emerges from the product stream. Furthermore, all the consumed oxygen is combined with hydrogen in the fuel to form water vapor. Any unburned fuel is inert, it remains in the product stream and does not undergo any other reaction. In this situation, the concentrations of the species in the product stream can be determined by chemical mass balances.

LH_2/LO_2 rockets typically operate at oxidizer-to-fuel ratios of 6. Since the molecular weight of hydrogen is approximately 2 g/mol and the molecular weight of molecular oxygen is approximately 32 g/mol, the mole ratio of hydrogen is 2:0.75. The complete oxidation of hydrogen is given by:

$$2H_2 + 0.75O_2 \rightarrow 1.5H_2O + 0.5H_2 \quad (54)$$

Hence, the mole fractions of the products are 0.75 for H_2O and 0.25 for H_2. Since the mole fractions are fixed, the composition of the exhaust stream is not a variable and the only free variable is the temperature of the products. An energy balance can be used to determine the

unknown temperature. The enthalpy of formation for water is -57.8 kcal/mol, using the value provided by Burke et al. [22] Thermodynamic properties were evaluated using REFPROP.

$$\sum_{reactants} h = \sum_{products} h \tag{55}$$

For hydrogen, the maximum safe temperature where accurate properties are available is 1000K, although REFPROP permits inputs of up to 1500K (1.5x the maximum safe temperature). For oxygen and water the maximum safe temperature is 2000K and the upper limit of the range is 3000K. REFPROP extrapolates properties at the maximum safe temperature to the 1.5x upper range limit. NASA polynomials, although often provided for up to 3500K or 5000K also extrapolate properties beyond their measured ranges. These maximum temperatures limits are based on where thermodynamic properties have accurately been determined. At high temperatures, measurements of molecular compounds are more difficult because of the difficulty in controlling chemical reactions. Since the flame temperature was expected to be beyond the range, the enthalpy beyond the upper limit was calculated by using the enthalpy at the upper limit (which is extrapolated) and then assuming that the specific heat is constant in order to calculate the enthalpy at higher temperatures. The specific heat was evaluated at the upper limit.

$$h(T|T > T_{max}) = h(T_{max}) + c_p(T_{max}) \times (T - T_{max}) \tag{56}$$

At atmospheric pressure (0.101325 MPa) the calculated temperature of the products was 3786K, at 11MPa the temperature was 3744K.

NASA Chemical Equilibrium with Applications

The NASA computer program Chemical Equilibrium with Applications (or NASA CEA) is a free tool available online which calculates chemical equilibrium compositions for various mixtures.

This tool was used to calculate the composition and temperature of the products. Using NASA CEA with liquid oxygen (T=90.17 K) and gaseous hydrogen (T= 300 K) yields an adiabatic flame temperature of 3610 K and mass fractions given in Table 7.

Table 7: Inlet Mass Fractions from NASA CEA with GH_2/LO_2

Species	**Mass Fraction**
H	0.002699
H_2	0.037596
H_2O	0.883440
H_2O_2	0.000041
HO_2	0.000110
O	0.004537
O_2	0.09127
OH	0.062453

Although highly detailed, the last major update to NASA CEA was in 2004, which is earlier than when the kinetic mechanism of Li et al. [23] and Burke et al. [22] were available in 2012.

Flow Reactor

The previous methods estimate the temperature of the products post-reaction through only thermodynamic considerations without regard to the fluid mechanics. Some sort of CFD (or either computational or analytical model) should be performed in order to incorporate the fluid flow effects in a steady flow reactor, where the reactants are fed into the reactor as a continuously flowing stream. Hence, a simulation was done with an idealized flow reactor in a 1D domain with perfectly premixed inlets. The results from this pseudo-1D simulation are not expected to match the detailed flame conditions in a rocket nozzle. The objective of this simulation is to obtain the correct composition and temperature in the post-flame region, after the regions which are dominated by chemical equilibrium.

The kinetic mechanism used in this study was the updated H2/O2 model by Burke et al. which has made considerable advances since CEA. With the different tool by Cd-Adapco called the DARS package, Adapco can perform this analysis but it requires a separate license that is not integrated with Star-CCM+; the DARS license was not available during this study. Alternative tools could have been used to test the differences between kinetic mechanisms but it was straightforward to run a CFD study in a 1D flow reactor, and these alternative tools were not explored in this study.

The mesh used for this flow reactor sub-study is presented in Figure 33. The flow reactor is 0.5 mm in streamwise extent with 100 equally spaced cells. The mesh is only 1 cell in the spanwise and lateral directions.

Figure 33: Computational Mesh for Flow Reactor Simulation

Although it is possible to use a three-dimensional solver for a two-dimensional mesh (or a one-dimensional mesh) by including zero gradient boundary conditions in the other directions, the results will be inconsistent with true one-dimensional or two-dimensional solvers because of differing discretization schemes and numerical accuracy. Additionally, the three-dimensional solver has additional computational cost because the solver must still solve for the variables in the unneeded dimension, which increases computational time for no added benefit. Even though the result is trivial, fixing or constraining the variables in the extra dimensions can actually lead to numerical inconsistency and generates errors that would otherwise not be present in a two-dimensional solver. Likewise, utilizing a three-dimensional solver on a one-dimensional grid, one may encounter similar issues. For these reasons, the two-dimensional solver in Star-CCM+ was used, making this a pseudo-1D simulation; Star-CCM+ does not have a one-dimensional solver, which would have been preferred over the two-dimensional solver.

A laminar flow model was used. An inviscid flow model was also attempted and the results were essentially identical to the laminar flow model. The premixed combustion model was used in Star-CCM+, which is inconsequential because the complex chemistry model was also used. The same kinetic mechanism by Burke et al. was used and the laminar flame concept

was used for the flow-chemistry interaction. Other settings were similar to simulations carried out on the thrust chamber. The multi-component ideal gases used the same thermodynamic properties and the segregated energy solver was used, using the enthalpy based formulation. The outlet was a pressure boundary condition with a pressure of 11MPa. The inlet boundary condition was a velocity inlet with a velocity of 5m/s. The magnitude of the velocity at the inlet does not affect the resulting properties apart from a slight change in the position where the heat release of the reaction and the gradients occurs, and the outlet properties are unaffected. The mass fractions at the inlet were simply specified to 0.142857 for H2 and 0.857143 for O2 (corresponding to an O/F ratio of 6.0); the inlet mass fractions were 0 for all other species.

Since the reactants are modelled as entering the flow reactor completely premixed, different temperatures cannot be specified for the reactants. Thus, a homogenous mixed temperature must be specified. The inlet static temperature was set to 200.5K. This temperature was determined from an energy balance of the entering reactants using properties from REFPROP. Properties from REFPROP were preferred for this calculation since they extend into the supercritical and liquid range whereas the properties from the NASA polynomials do not. NASA polynomials are generally valid for temperatures greater than 300K, though some polynomial sets extend this range down to 200K. Liquid oxygen at 91.7K is well outside this range. Furthermore, the polynomials do not take into account pressure effects. Hence, the mixed temperature obtained using properties from REFPROP is superior and more accurate than the NASA polynomial approach. When 13.8kg/s of O2 at 91.7K and 11MPa is mixed with 2.3kg/s of H2 at 300K and 11MPa, the resulting mixed mean temperature was

determined to be 200.5K. No reactions are permitted to take place and the composition of the mixture is still the same, except that they are now made homogenous.

The simulation converged quickly, in less than 200 iterations and taking only a few seconds. The temperature profile in the flow reactor is given in Figure 34 and the mass fractions are in Figure 35.

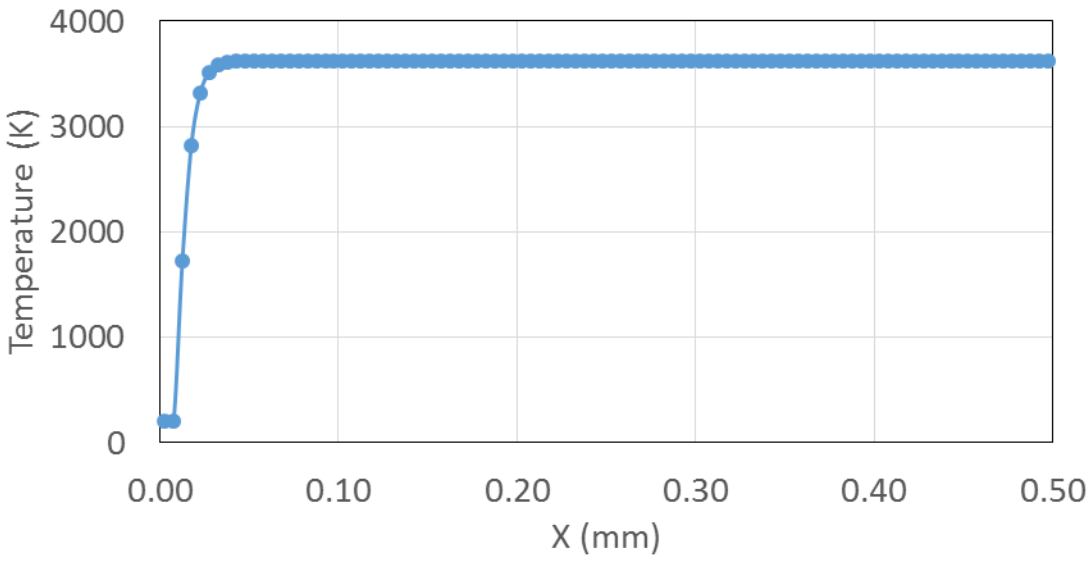

Figure 34: Temperature Distribution in Flow Reactor

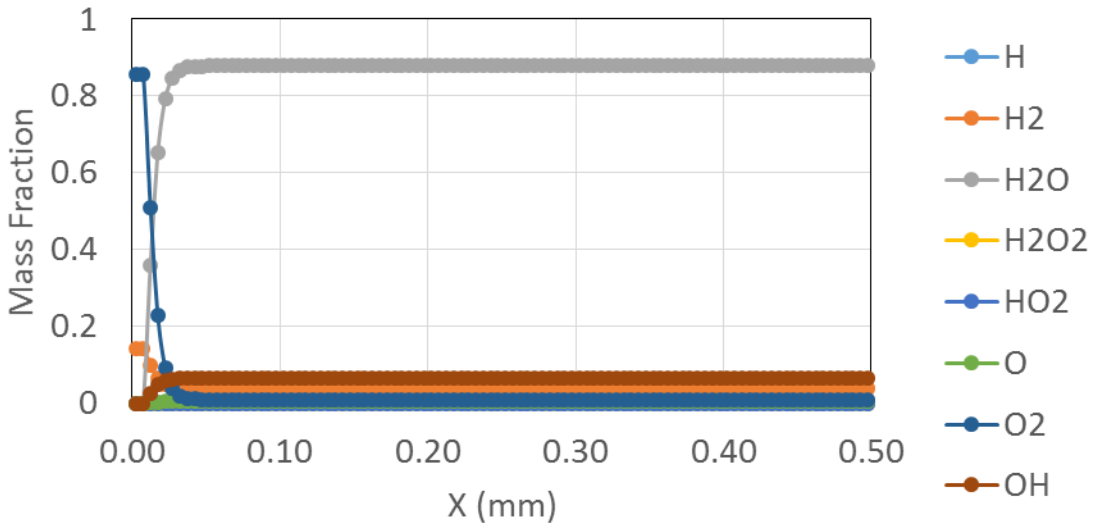

Figure 35: Mass Fraction Profile in Flow Reactor

The reactions occur immediately after the inlet. The temperature of the fluid rises rapidly as the inlet gases are heated, driven by the heat released from the combustion of hydrogen and oxygen. Molecular hydrogen (H_2) and oxygen (O_2) are rapidly depleted, generating a large amount of water (H_2O). Small amounts of other species are also present in the exhaust stream, mostly OH followed by remaining fuel H_2 and oxidizer O_2. The species present in the lowest amounts from greatest to lowest are O, H, HO_2, and H_2O_2. It is important to point out that the mass fraction of OH is greater than the remaining fuel and oxidizer. Since HO_2 and H_2O_2 were the least significant, their omission in the reduced mechanism by Amato et al. is justified. Although the concentration of H was lower than O, H was included whereas O was neglected in the reduced mechanism. In this case, the low concentrations of these products have little influence on the properties of the resulting mixture, which is composed primarily of water vapor. However, in the presence of wall cooling, the temperature

distribution in rocket nozzle will be hottest near the center and coolest near the walls. The different temperatures allow different states of chemical equilibria to exist at different locations in the nozzle.

The flow reactor simulation predicted an outlet flame temperature of 3633 K with outlet mass fractions in Table 8.

Table 8: Inlet Mass Fractions from Flow Reactor Simulation

Species	**Mass Fraction**
H	0.002788
H_2	0.037871
H_2O	0.878177
H_2O_2	4.60E-05
HO_2	0.000119
O	0.004885
O_2	0.009924
OH	0.06619

Film Simulation

The centerline mass fractions were extracted from one of the film cooling cases run and at X=-0.2m. The static temperature at X=-0.2m was 3611K and the mass fractions at this location are in Table 9. Recall that the inlet mass fractions used in this simulation were the mass fractions from Amato et al. After a distance of 0.2m, the composition of the hot gas has

changed from the specifications at the inlet to the mass fractions in Table 9. In this section of the thrust chamber, the nozzle is constant area. The cooling at the walls is also too far away to affect the centerline properties. The change in mass fractions is predominantly a result of using inlet mass fractions that were inconsistent with the current kinetic model. Hence, the flow entering the nozzle reacts (according to the current kinetic model) and adjusts to the new equilibrium. A consequence is that the temperature has decreased from the value at the inlet of 3750K to 3611K. The temperature drop decrease is also due to the production of new species (the ones neglected in reduced kinetic model by Amato et al.), which have a positive enthalpy of formation (heat must be added to generate these species).

Table 9: Inlet Mass Fractions from Film Simulation

Species	**Mass Fraction**
H	0.003255
H_2	0.052775
H_2O	0.880425
H_2O_2	3.07E-05
HO_2	6.78E-05
O	0.003368
O_2	0.004995
OH	0.055083

The mass fractions in Table 9 are the correct inlet boundary conditions that are consistent with the current kinetic model. These are the inlet mass fractions that should have been applied. However, as long as the inlet mass fractions are not too unrealistic however, the chemistry time-scale is fast so that the gas adjusts to the new equilibrium quickly and inlet mass fractions do not need to be accurately determined at the inlet. The correct mass fractions will automatically “appear” not too far from the inlet.

Summary

A summary of the mass fractions determined from various methods is provided in Table 10 and the post-flame temperatures are in Table 11.

Table 10: Summary of Inlet Mass Fractions from Various Sources

Species	Mass Fraction				
	Complete Oxidation	**Amato et al.**	**NASA CEA**	**Flow Reactor**	**Sim**
H	0	0.00246	0.002699	0.002788	0.003255
H_2	0.035958	0.05205	0.037596	0.037871	0.052775
H_2O	0.964041	0.90166	0.883440	0.878177	0.880425
H_2O_2	0	0	0.000041	4.60E-05	3.07E-05
HO_2	0	0	0.000110	0.000119	6.78E-05
O	0	0	0.004537	0.004885	0.003368
O_2	0	0.00313	0.09127	0.009924	0.004995
OH	0	0.0407	0.062453	0.06619	0.055083

Table 11: Summary of Post-Flame Temperature Calculations

Complete Oxidation	**Amato et al.**	**NASA CEA**	**Flow Reactor**	**Film Sim**
3744 K	3750 K	3610 K	3633 K	3611 K

Without preliminary investigation, the most accurate and best inlet conditions to use are either the results from the NASA CEA calculation or Flow Reactor since they include detailed kinetic mechanisms and will more accurately predict the correct mass fractions in the post-

flame region. It should be emphasized that these approaches are an attempt to generate a substitute inlet boundary condition in place of performing a more complicated simulation involving the injector dynamics. The correct inlet boundary condition should involve the actual geometry of the injector, realistic models for the physical processes occurring, accompanied with realistic material, thermodynamic, and thermophysical properties of the materials involved. This is performed in this thesis, but is not included in further simulations due to the effects of the injector being negated at a certain point.

SETUP FOR COOLING DESIGNS

Baseline 36° 100 Channel Assembly

Benchmark Study

Wadel used a design with 100 cooling channels stretching the length of the nozzle evenly spaced around the circumference of the nozzle. This design, known as “Design 1” and its results were used as the benchmark of this thesis. The baseline configuration is modelled after this design, and in order to verify that this author’s data is accurate, the baseline configuration will be verified against the temperature distribution data attained by Wadel.

Baseline: Configuration 2

The second configuration is the full assembly of the internally cooled nozzle in a 36° sector. A 36° sector was chosen since an even amount of channels could be represented, and the angle was an integer. Also, the max skewness angle resulting from the wedge point is below 75°, meaning that the results will not be affected by skewness angle. This sector includes 10 cooling channels, pictured in Figure 36.

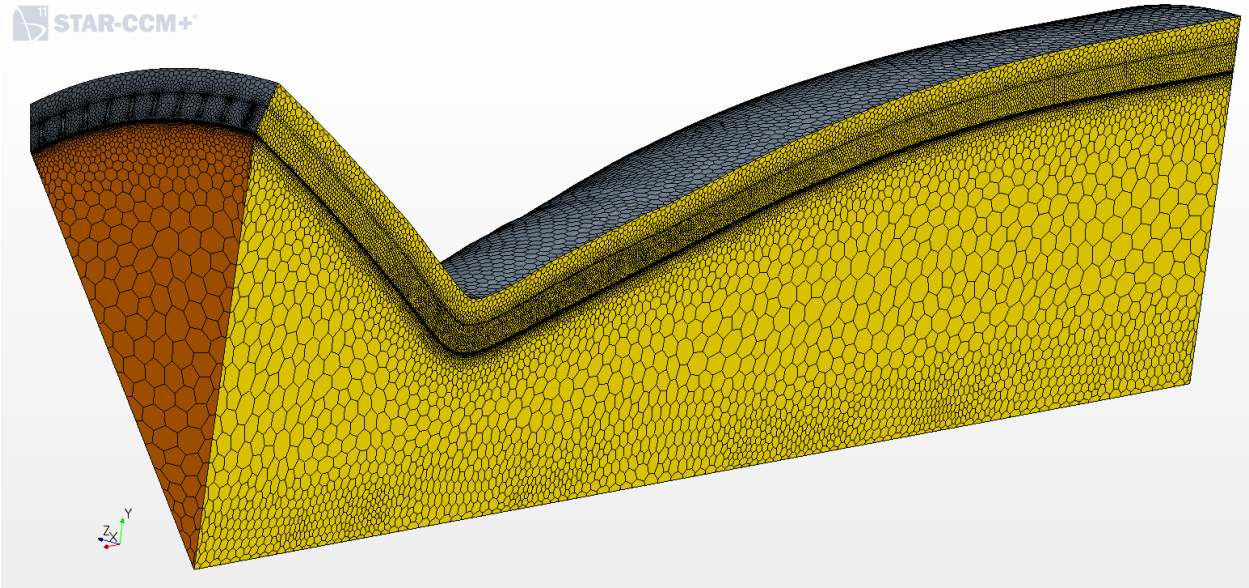

Figure 36: 10 channel full mesh

Mesh Continua

It has been stipulated that modelling multiple channels in CFD is too computationally expensive [54]. With current reference values, a complete nozzle representation would contain 61,777,780 cells. The channels alone contain 425,797 cells each. However, there are workarounds to meshing all of the channels in a 3D rocket nozzle model while using only a section of the nozzle for analysis. To minimize cell count, only one channel was meshed. The heat transfer data, specifically temperature, from this channel was mapped onto the walls of the other nine channels, thereby mimicking the effects of 10 channels due to radial symmetry while reducing cell count significantly. This sort of technique can be used in several different situations, and not just to map heat transfer data. This technique can decrease computational complexity for many 3-dimensional simulations.

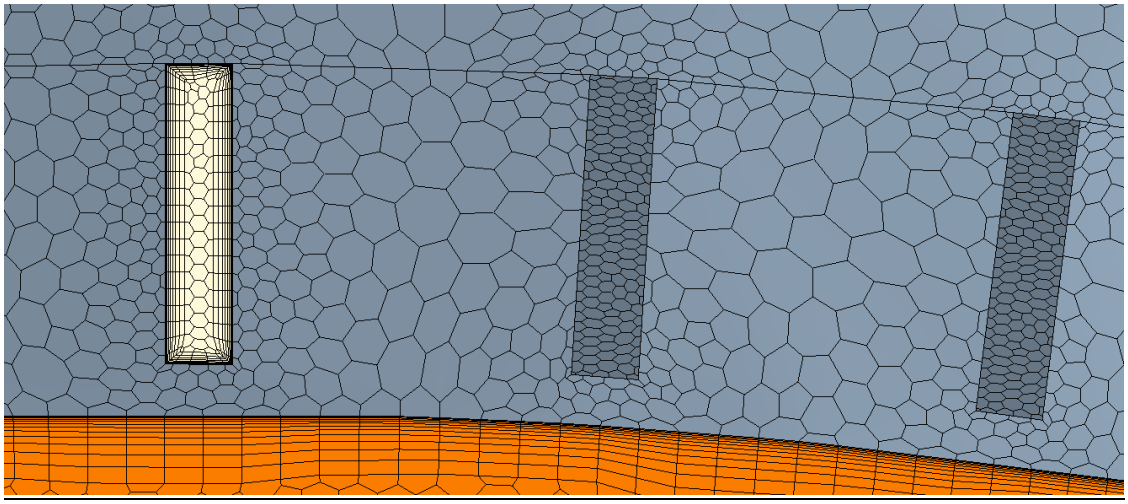

Figure 37: One channel mesh method

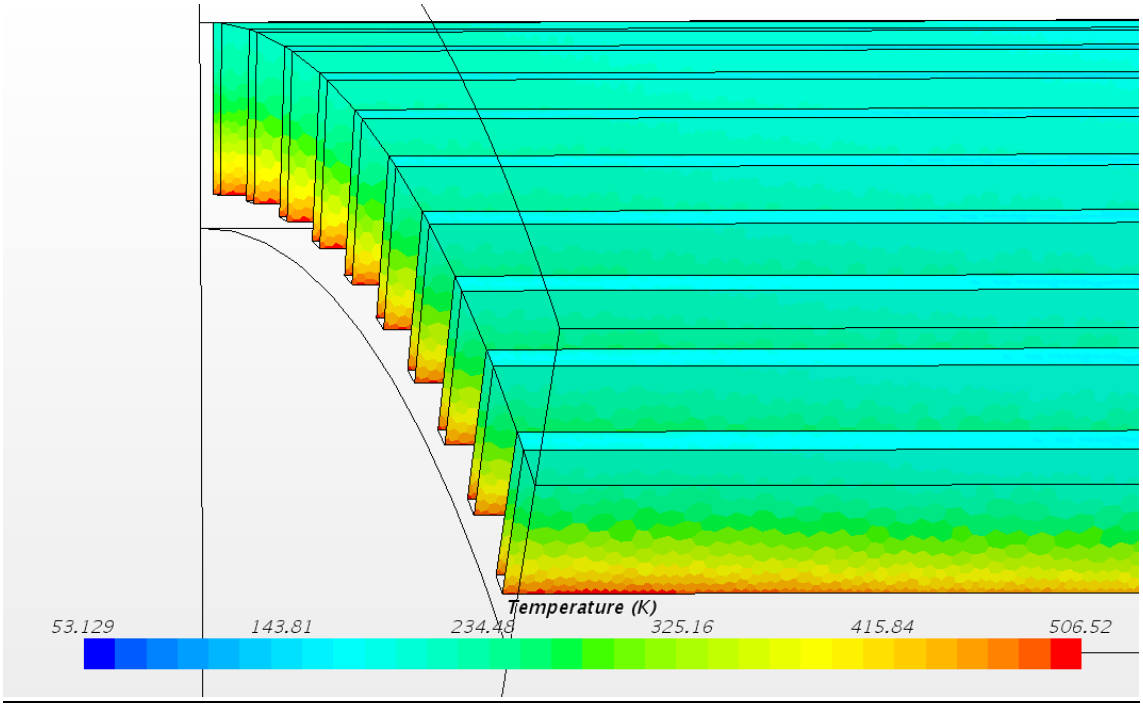

Figure 38: Note how all temperature distributions are the same

The remainder of the baseline design, the liner, jacket, and hot gas, were left at general mesh properties previously articulated. The liner cell count was 840,888; the jacket cell count was 371,489; and the hot gas cell count was 707,431.

Governing Equations

The governing equations remain the same as the general ones explained previously, however the species transport model was slightly different.

Table 12: Reduced Complexity Mass Fractions for H2/O2 Reaction

Species	**Mass Fraction**
H	0.00246
H_2	0.05205
OH	0.04070
O_2	0.00313
H_2O	0.90166

Since the results of the injector simulations showed that properties remain the same downstream of the inlet regardless of the inlet conditions, the injector was not included in the hot gas model in configuration 2. It was still important to include the species transport model and turbulence-chemistry interactions. However, modelling 8 species at once is computationally expensive, and since the sector included channels with high cell count, it was determined that using the simplified version of the inlet mass fractions and inlet flame temperature documented by Amato et al. was necessary [24]. This assumption has been verified as accurate. Amato omitted the following species from the transport model: O, HO_2, and H_2O_2.

Boundary Conditions

The baseline configuration had a varied mass flow rate from 0.0115kg/s to 0.023kg/s per channel. This equates to a total mass flow rate in a 360° nozzle of 1.15kg/s to 2.3kg/s. This was done in order to compare the 100 channel baseline to a design that uses half the cooling channels: using half the flow rate at 1.15kg/s for 100 channels would indicate the same amount of hydrogen flowing through 50 channels at the nominal flow rate of 2.3kg/s. Comparisons and reasoning will be explained further on.

In congruence with inlet temperatures, the hot gas inlet temperature was specified at 3750K. Channel inlet temperatures and pressures remained the same as the general boundary conditions.

Combined Internal Cooling and One Row of Film Cooling

Geometry

The film cooling holes themselves are cylindrical and inclined 30° from the nozzle centerline. The film holes have elliptical inlets and outlets due to this incline in order to remain flush with the nozzle wall. The inclined film holes were chosen because Goldstein et al. [33] found that inclined holes perform better in terms of film cooling effectiveness due to the lack of mixing between film and hot gas. The film hole is located 2.748 in (or approximately 2.75 in) upstream from the nozzle throat. This distance was chosen in order to achieve the goal of reducing the peak temperature to 613K: the temperature approaches 613K at this point in the 100 channel baseline configuration. The film holes were not located at the throat since the global peak temperature would not be reduced, as film cooling effectiveness approaches 0 after a

significant length. The objective is global temperature reduction, and so keeping the film hole nearer the throat is the best choice.

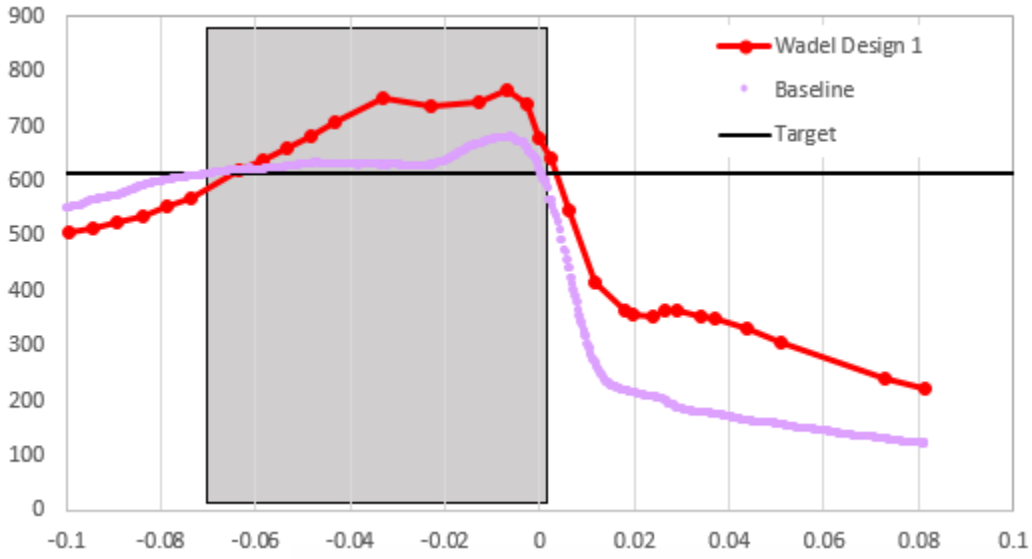

Figure 39: Region of Interest Using Target Temperature

Injecting a 300K film is predicted to lower the temperature so it remains below the desired peak temperature goal of 613K.

Film Cooling Effectiveness

Film cooling effectiveness, Eqn. (57), is characterized by the reduction in temperature of the hot gas-side wall in comparison to adiabatic wall temperature and freestream temperature.

$$\eta = \frac{T_\infty - T_{aw}}{T_\infty - T_{c,exit}} \tag{57}$$

where T_∞ is the freestream hot gas temperature, T_{aw} is the adiabatic wall temperature without film cooling, and $T_{c,exit}$is the coolant temperature at the film hole exit. An η of 1 describes perfect cooling effectiveness, when an η of 0 describes no temperature reduction.

Using film cooling effectiveness correlation correlations by Baldauf et al. [60], film cooling effectiveness was predicted to decrease gradually to 0.1 as distance increased to 30D down the nozzle wall.

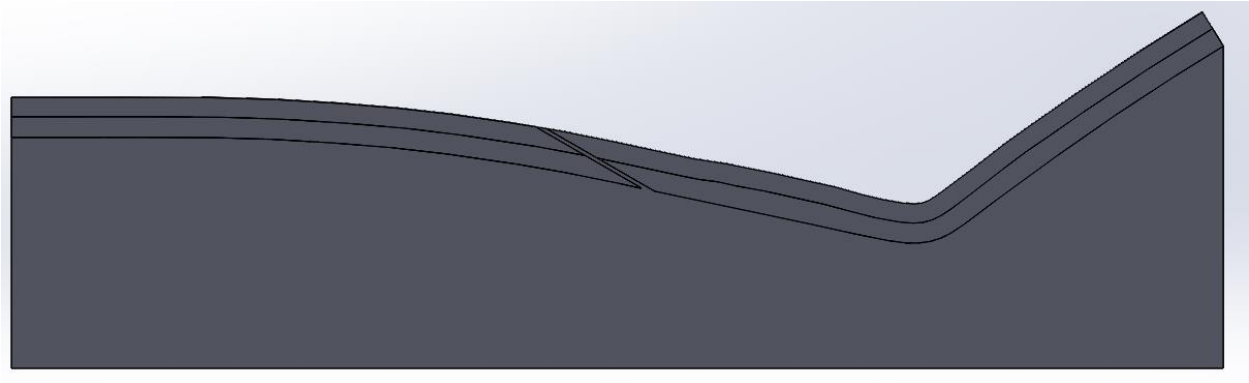

Figure 40: Slice representation of film hole placement

The number of film holes was determined by assessing the nature of film cooling and noting that, if only 10 or 20 film holes were applied across the entire circumference of the nozzle, minimal cooling would be achieved. 50 film holes were included as a conservative design in order to ensure the effects of film cooling would be apparent. In order to fit 50 film cooling holes around the circumference of the nozzle, it was necessary to remove cooling channels. The space between cooling 100 channels would not be enough to realistically implement film cooling holes in-between; a minimum wall thickness must be maintained to retain the structural integrity of the thrust chamber. After removing 50 cooling channels, the space between channels allowed for a film hole up to 1.5mm in diameter. The minimum size was 0.5mm (considering manufacturing limitations on the smallest hole that can be drilled); and so a median of 1mm was chosen in order to allow for ample space between the channels and film holes, which ensures ease in manufacturing and an improvement in structural

integrity. These parameters (1 mm hole diameter placed at X=-2.75 in and angled 30° to the nozzle centerline) amounts to a film hole length-to-diameter ratio (L/D) of 33.5.

Mesh Continua

The cooling channels and film holes are the most detailed in order to best capture the cooling characteristics. The cooling channel mesh models and conditions mirror that of the second configuration of 10 channels, the only difference being the number of channels themselves.

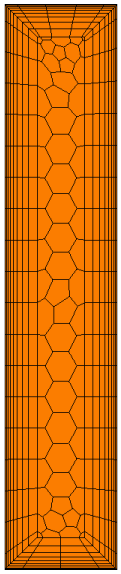

Figure 41: Channel Inlet Mesh Representation

Film Holes

The film holes are modelled to be just as dense as the cooling channels, with at least three cells spanning the diameter of each film hole. Six prism layers are included within the film holes at a thickness 1% the base size. The surface size was custom and set to 1% of the base size, with a target size of 5%. At the location of the film entrance into the hot gas, the prism

layers along the nozzle hot gas wall are interrupted. This causes the prism layers to rapidly decrease approaching the film hole and rapidly increase downstream of the film hole. This can negatively affect the accuracy of the heat transfer model around the film hole, and so it is important to ensure that cell density remains high at the film entrance. Furthermore, it is important to keep the prism layer thickness after the film hole relatively high to include the entire film within it.

Liner

The liner mesh continuum mirrors that of the 10 channel mesh, however there are more cells due to the subtraction of cooling channels. It was important to ensure that skewness angle was kept to a minimum around the film holes. The skewness was a source of difficulty, as the small diameter of the film hole coupled with its elliptical geometry required significantly increased cell density around the film hole.

Jacket

The jacket is very similar to previous meshes. However, the jacket mesh had to be altered significantly around the five film holes in order to properly model the heat transfer characteristics and minimize skewness, as described for the liner. The film holes are meshed with a fine grid, and so the surrounding surface of the jacket had to match accordingly. The jacket minimum size was reduced to 5%, with a target size of 100%. This allowed for minimally skewed cells around the lip of the film hole inlet.

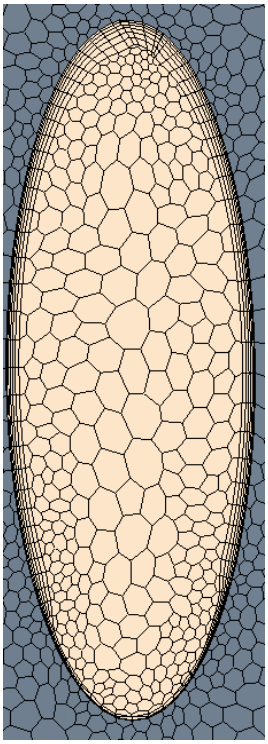

Figure 42: Film hole mesh representation

Hot Gas

The hot gas mesh continuum is identical to that of the baseline. The film hole mesh is represented in Figure 43 using a slice that cuts through one film hole. The increased cell density within the film hole itself can be seen here.

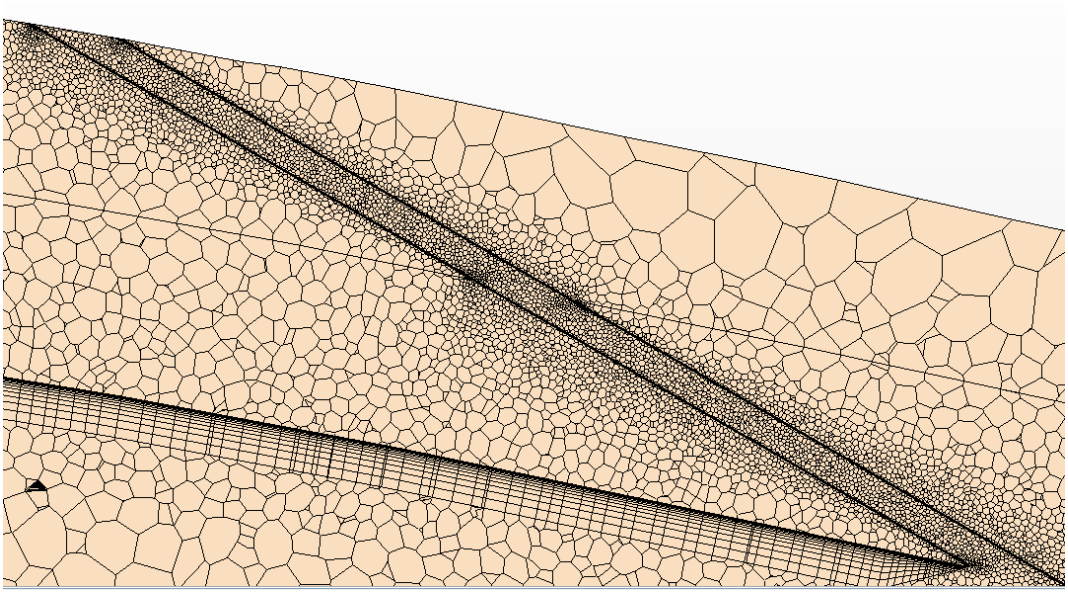

Figure 43: Channel Inlet and Film Slice Mesh Representation

Figure 44 is the same slice but encompassing the entire nozzle. Figure 45 depicts the outer mesh of the entire sector, and is colored to represent the different boundaries: tan denotes inlet, yellow represents symmetry plane, and grey denotes wall. Orange denotes an outlet, as depicted in Figure 41.

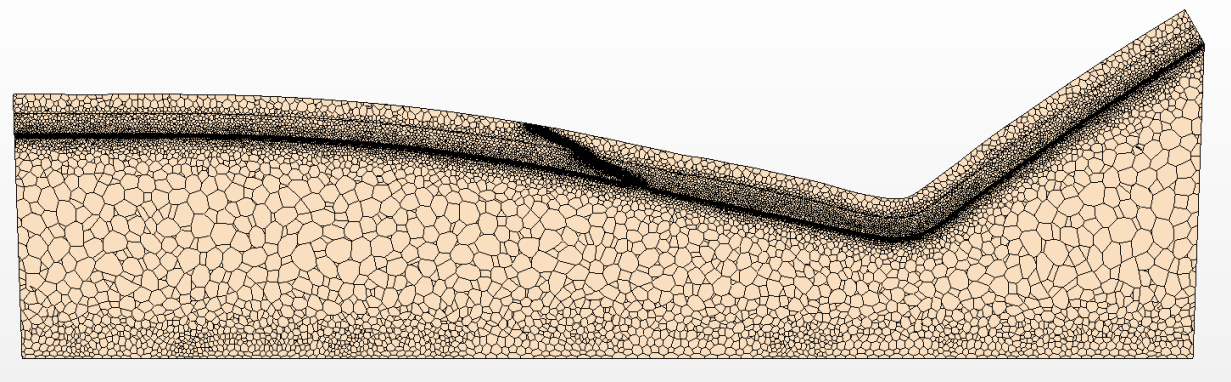

Figure 44: Slice mesh representation of film configuration

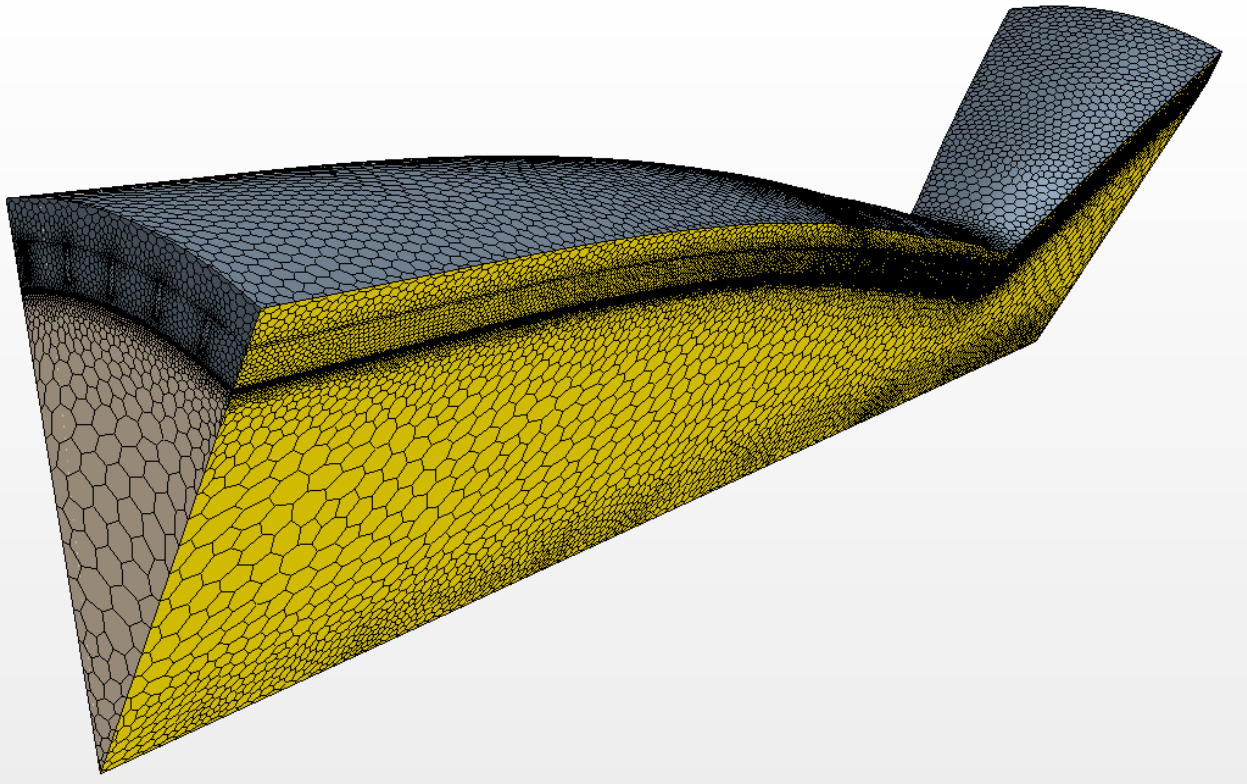

Figure 45: Full mesh of film setup

36° Full Assembly with 50 Channels

In order to isolate the effects of reducing the cooling channels from 100 channels to 50 channels, it was necessary to repeat the baseline design with half the channels. The mesh and governing equations remain the same, however per channel mass flow rate will be varied from 0.023kg/s to 0.046kg/s per channel, which equates to a total channel mass flow rate variation from 1.15kg/s to 2.3kg/s. This compares similar total masses of hydrogen flowing through the channels in both the 100 channel configuration and 50 channel configuration. Channel cell count is 425,870, liner cell count is 444,913, jacket cell count is 210,210, and hot gas cell count is 454,365.

RESULTS: BASELINE AND FILM COOLING DESIGN

Each configuration was run until convergence. Convergence was determined to be when temperature ceased varying more than 0.1K per 50 iterations, which amounted to approximately 1000-2000 iterations. Roughly 100 iterations could be performed per hour on a desktop with a i7 950 quad-core CPU so that each simulation was roughly 100 compute hours. Each configuration was also run at several boundary conditions where mass flow rate and blowing ratio were varied where applicable. The results for each configuration were then compared with each other after appropriate optimization analysis and troubleshooting.

Baseline: 36° 100 Channels (100CC)

The 100 channel baseline configuration was compared to Wadel's results of their first design, the 100-100-100 HARCC cooling channel geometry. There are 100 channels total within the nozzle wall, and 10 channels included in the 36° sector used for analysis. The original coolant mass flow rate was 2.3kg/s total, or 0.023kg/s per cooling channel. The temperature results of the baseline design are shown in Figure 46.

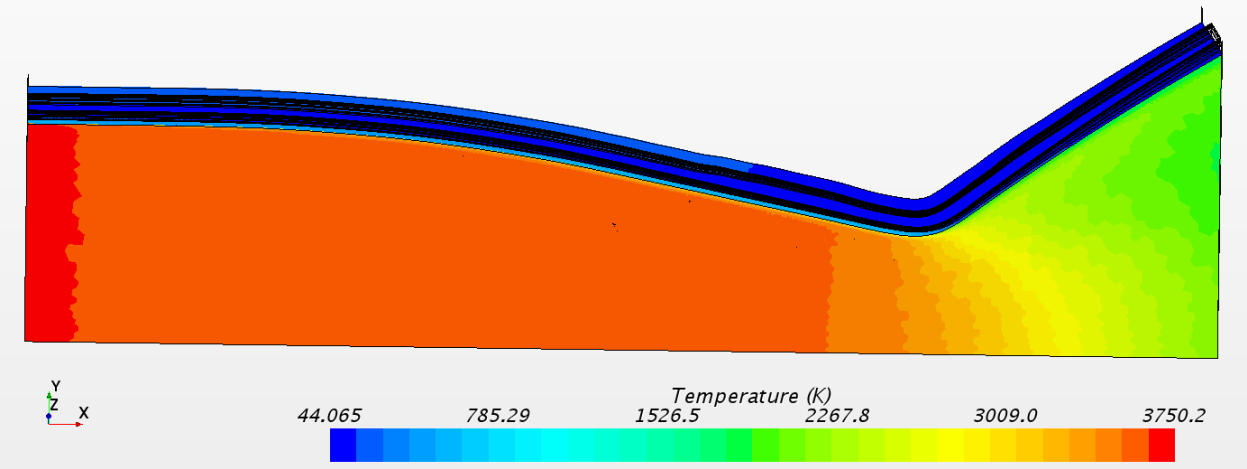

Figure 46: Temperature Distribution of 10 Channel Setup

Benchmarking

The baseline configuration is benchmarked against the Design 1 of Wadel et al. in Figure 47.

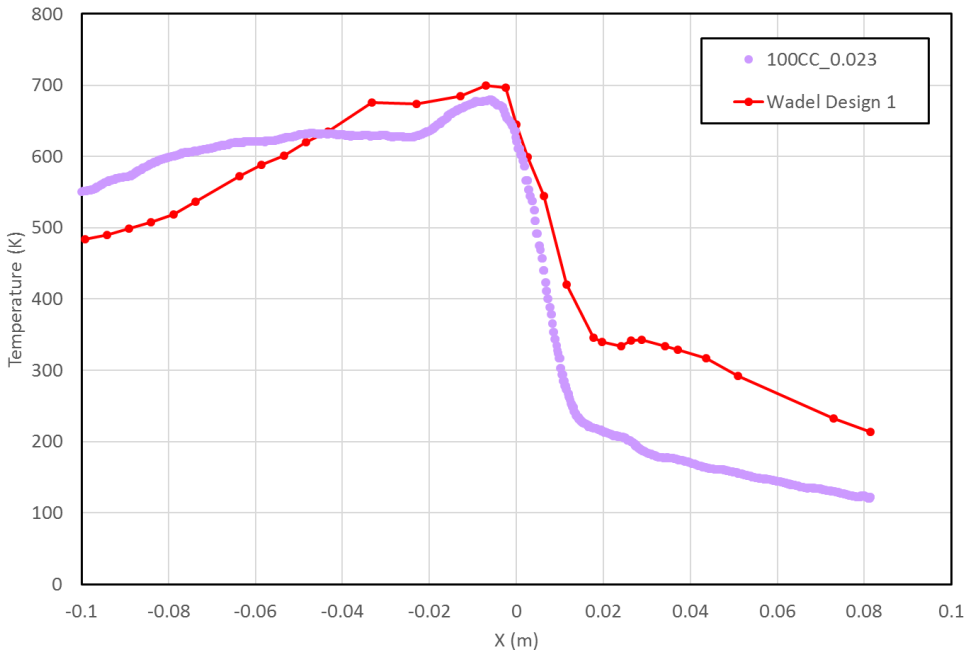

Figure 47: Benchmark vs Baseline Hot Gas Wall Temperature Profile

As illustrated, there is some variation approaching the throat and downstream of the throat. This is because the inlet temperature was specified at 3750K for the current study; the inlet temperature was not articulated in Wadel's publication. Inlet mass fractions were also not mentioned. The drop in diffuser temperature is most likely due to variation in the properties of the gases present. It is not mentioned how Wadel et al. attained their properties for hydrogen and oxygen, but for this analysis, REFPROP was used for properties. The version of REFPROP used is from 2011, which is years after Wadel et al. completed their analysis, and so they could not have used the same properties.

Results

Temperature distribution is as expected, with a temperature relatively uniform throughout the nozzle until the throat, where the peak temperature is observed. After the throat, due to the area change and Mach number increase, the temperature decreases. As explained before, temperature distribution before X = -0.1m is neglected due to the question in accuracy. Using the Quentmeyer correlation, the Nf for a total mass flow rate of 2.3kg/s is 586 cycles, using a maximum Tgw of 680K.

Y+

The y+ is a non-dimensional distance to the nearest wall scaled by inner coordinates. The scaling for the distance is actually the inner velocity scale (the friction velocity). Having low values of y+ for wall adjacent cells is vital to for simulations of wall-bounded flows because of the need to predict the correct wall shear stress. For computational grids with a small enough y+, the wall shear stress in turbulent flows can be computed from the so-called law of the wall (a semi-empirical law), avoiding the need to use wall-functions (additional models for the wall shear stress). Salim & Cheah [61] have discussed meshing strategies with regards to y+ requirements. The concept of wall y+ is generally only discussed in simulations of turbulent flows, as the wall shear stress in laminar flows is straightforward to determine.

The wall y+ for the baseline case at 0.023kg/s per channel mass flow is plotted versus channel length in Figure 48. The minimum, maximum, and average y+ for each channel wall and the hot gas side wall are tabulated in Table 13. The maximum the hot gas wall y+ was 157, minimum y+ was 6, with an average of 52. Hot gas side wall y+ is generally between 30 and 130.

Although meshes with lower wall y+ values can more accurately predict the wall shear stress for broader class of flows and are low y+ values are generally preferred, the y+ values in this work are not too high (y+<500) and are low enough to provide reasonable results. The rocket thermal evaluation code, which uses Dittus-Boelter correlations with curvature correction factors, has matched fairly well with experimental data. Hence, it is presumed that as long as the y+ is low enough to predict reasonable values for the wall shear tress, that the heat transfer performance of the cooling channels should be reasonably captured as well.

Some of the wall y+ values are between 10 and 30, which is within the buffer region of the boundary layer. In the buffer region, neither the linear law of the wall nor the log law of the wall is valid. Cells in this y+ range suffer from less accurate predictions of the wall shear stress.

A more important concern is the effect of the mesh quality on the turbulence models. Two layer models blend a one-equation approach with a two-equation k-epsilon model. The one equation approach by Wolfshtein [62] solves the transport equation for the turbulent kinetic energy but computes the dissipation rate algebraically. The one-equation approach is superior to the two transport equations near walls. Far from walls, the two transport equations for the turbulent kinetic energy and dissipation rate are better. Star-CCM uses the wall-proximity indicator of Jongen [63] to delineate the low y+ and high y+ regions, and then blends the two approaches together. The blending tends towards the one equation approach near walls and towards the two transport equation approach in the far-field.

Having cells of intermediate sizes is not so problematic because the Two-Layer All y+ treatment is being used in Star-CCM+, which contains blending functions so that intermediate meshes may be used that are not globally < 10 or > 30. The influence is also mainly local, the flow in the far field, far away from walls, is not significantly affected. The most important factor is to ensure that the mesh is globally less than a targeted y+ value. Figure 48 and Table 13 show wall y+ for the 0.023kg/s per channel case.

Table 13: Maximum, Minimum, and Average y+ for Baseline Case

	Minimum y+	Maximum y+	Average y+
Bottom	15	165	45
Side	19	265	125
Top	52	213	132
GW	6	157	52

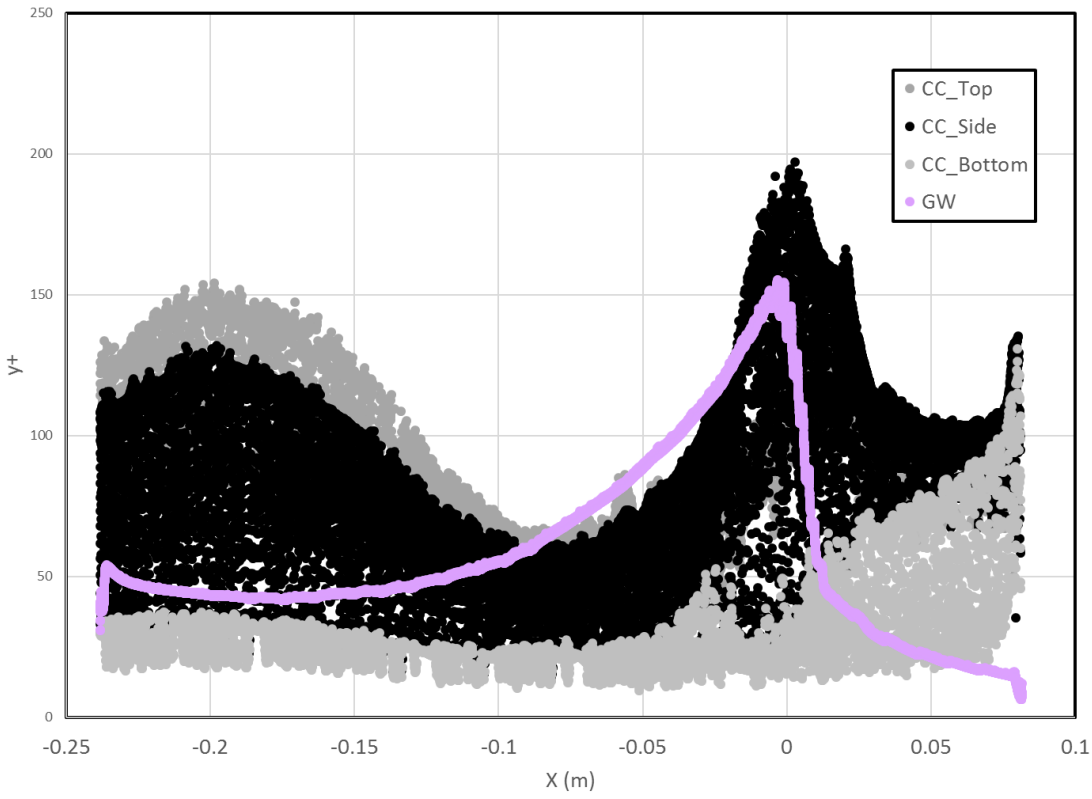

Figure 48: Wall y+ of Channel Walls and Hot Gas Side Wall

On the liner wall, the wall y+ rises from the inlet gradually towards the throat and decreases after the throat, whereas the flow is accelerating throughout the entire length of the nozzle. Because of the wall curvature in the contracting part of the nozzle, the boundary layer is compressed by the oncoming flow, reducing the boundary layer thickness and increasing the wall shear stress dramatically; this phenomenon results in the wall y+ behavior seen in Figure 48. The wall y+ reaches a maximum just before the throat, approximately at the inflection point of the nozzle. After the throat, the boundary layer relaxes and is able to re-thicken, hence the y+ returns to lower levels after the throat.

It can be shown, for incompressible flow in constant area ducts, that the friction velocity is linearly related to the bulk channel velocity, as in Eqn. (58). See the section on Friction Velocity in [64] for the derivation of this result in the proper context.

$$u_\tau = u_b \sqrt{\frac{f}{8}} \tag{58}$$

For high enough Reynolds numbers, the friction factor of ducts tends towards a constant. Using these two results, one can quickly estimate the y+ at other channel flow-rates. When the flow rate is halved, the wall y+ will be approximately half. When the flow rate is doubled, the wall y+ will be approximately double. Hence, it is not necessary to measure the wall y+ for all cases simulated. The mass flow rate in the thrust chamber was fixed for all cases. The only changes to the wall y+ are for cases without film cooling from non-linearities due to slight temperature changes. The addition of film cooling disrupts the wall boundary layer and the local wall shear stress. However, the maximum wall y+ for the film cooled nozzle was 154,

with an average of 50, which is nearly the same as the configuration without any film. Hence, the near wall mesh resolution is roughly the same for the simulations with film and without film.

The addition of turbulators also dramatically affects the wall y+ because of the increased friction factor in turbulated channels. The maximum wall y+ on the top wall was 83, which is lower than the non-turbulated cases even though the wall shear stress is higher. The prism layers were much thinner for the turbulated cases in order to have grid points smaller than the size of the ribs; the thinner prism layers helped to reduce the maximum wall y+ somewhat. On the side walls, the maximum wall y+ was 185. On the bottom wall (neglecting the y+ on the rib features), the maximum wall y+ was 69. The maximum wall y+ was 185 on the ribs, much higher than the non-ribbed areas. The average wall y+ values were much lower than the maximum values. The top wall averaged 45, side walls averaged, 38, the non-ribbed portions of the bottom wall averaged 7 between ribs and 16 upstream and downstream of the ribbed section. On the ribs, the average wall y+ was 17.3. Extra caution was necessary to ensure the mesh resolution as still adequate after the turbulators were applied, but the resulting mesh should be able to capture the most important features of the rib-induced flow in the cooling channels.

36° Film Cooling at 2.75in before throat (50CCF)

The main objective of this thesis is to determine whether film cooling can effectively cool the rocket nozzle. In order to determine this, it is necessary to vary some of the film conditions to determine what design cools most effectively. Several simulations were run with variations in both blowing ratio and channel mass flow rate. Figure 49 is a plot of the temperature on a plane slice through the domain for a case where the coolant flow rate through each channel was 0.023 kg/s, equivalent to a sum of 1.15 kg/s through 50 channels. The temperature profile with a total coolant flow of 2.3 kg/s of hydrogen is depicted in Figure 50. The same profile is depicted with a total coolant flowrate of 1.16kg/s in Figure 49.

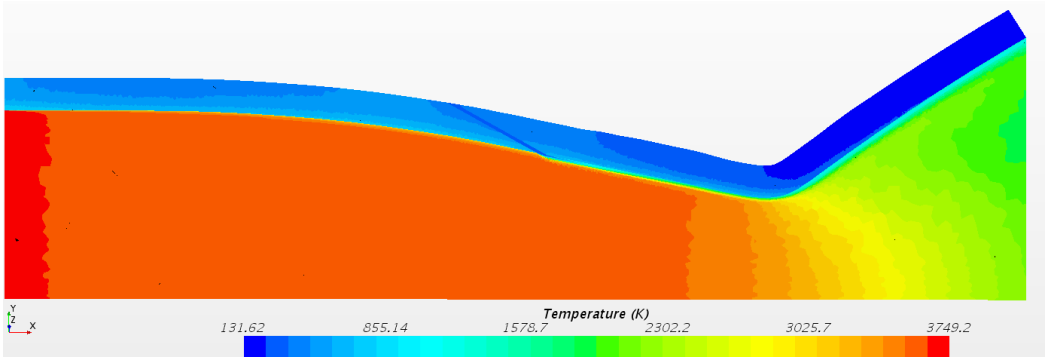

Figure 49: Configuration 3, channel $\dot{m}_{tot}$ = 1.15kg/s

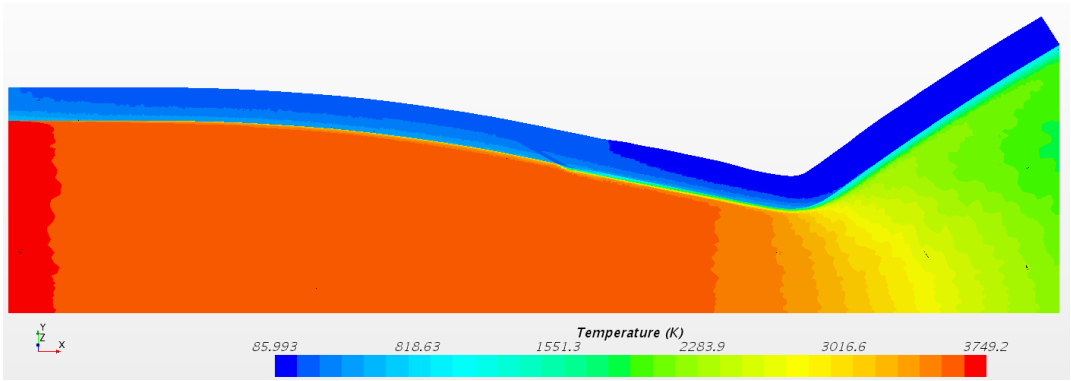

Figure 50: Configuration 3, channel $\dot{m}_{tot}$ = 2.3kg/s

Varied Blowing Ratio

First, blowing ratio was varied with a per channel mass flow rate of 0.023kg/s per channel, which amounts to a total hydrogen flow in the cooling channels of 1.15kg/s. The blowing ratio was varied from 0.053 to 2.892, which equates to film mass flow rates of 0.0001kg/s to 0.0055kg/s. The blowing ratio was increased with 8 even increments. Blowing ratio can significantly change the performance of film cooling. A blowing ratio that is too high will cause flow separation and reduce effectiveness. A blowing ratio that is too low will still provide a thermal and species boundary layer, however it will be smaller and less effective. Figure 51 and Figure 52 show the results of varying blowing ratio, depicted in two separate graphs for ease of understanding. The graphs were split at a blowing ratio of 1, which is included on both charts.

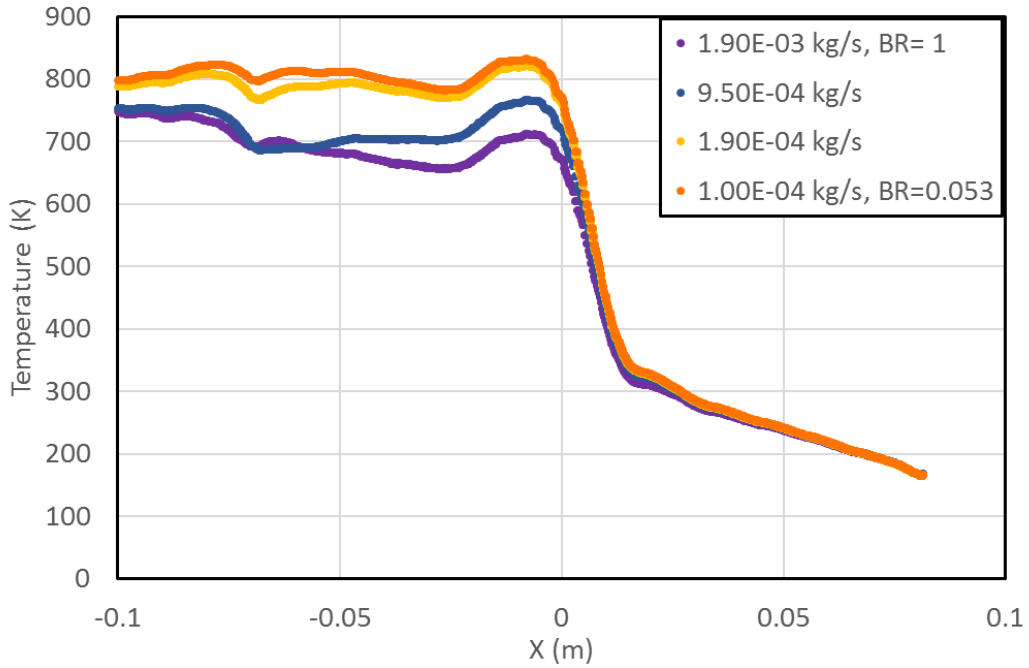

Figure 51: Liner Temperature Recorded at 0 Degrees, Varying Film Mass Flow from 1e-4kg/s to 1.9e-3kg/s at Channel Mass Flow Rate of 0.023kg/s

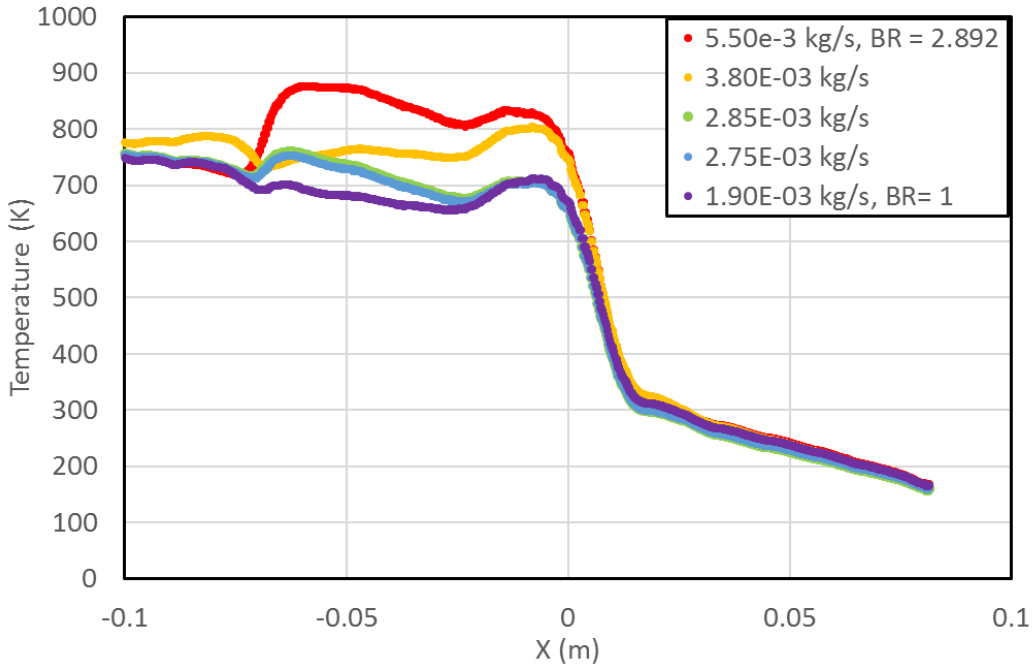

Figure 52: Liner Temperature Recorded at 0 Degrees, Varying Film Mass Flow from 1.9e-3kg/s to 5.50e-3kg/s at Channel Mass Flow Rate of 0.023kg/s

The graphs show a clear trend in the film effectiveness. As blowing ratio approaches 1, T_{gw}decreases, which is indicative of an increase in film cooling effectiveness. However, as blowing ratio is increased above 1 up to 2.892, the temperature profile shows an increase in T_{gw}. The increase shows that the film is separating from the wall and mixing with the freestream flow, which in turn increases T_{gw} and therefore decreases film cooling effectiveness. While this study does not concentrate on the efficiency of the nozzle combustion, it is important to note that mixing the cold H_2 gas with the hot combustion gas will decrease efficiency of the nozzle itself (by decreasing the overall oxidizer-to-fuel ratio). Looking at the T_{gw} profiles, the ideal blowing ratio is 1, which equates to a per film hole mass flow rate of 0.0019 kg/s.

Varied Channel Mass Flow Rate

The results of combined internal cooling and film cooling at a blowing ratio of 1 with a per channel mass flow rate at the baseline 0.023kg/s yields a peak Tgw of 712K. This does not meet the goal temperature of 613K. However, there is room for improvement regarding the channels themselves. Since the total channel mass flow rate is only 1.15kg/s (at a per channel mass flow rate of 0.023kg/s), there is an additional 1.15kg/s of hydrogen that is not in use in this design. Therefore, it is possible to increase the per channel mass flow rate from 0.023kg/s to 0.046kg/s, which will result in a total mass flow rate of 2.3kg/s in all 50 channels. Mass flow rate was varied as such in 5 even increments, and the liner wall temperatures are pictured at angles 0° (Figure 53) and 3.6° (Figure 54).

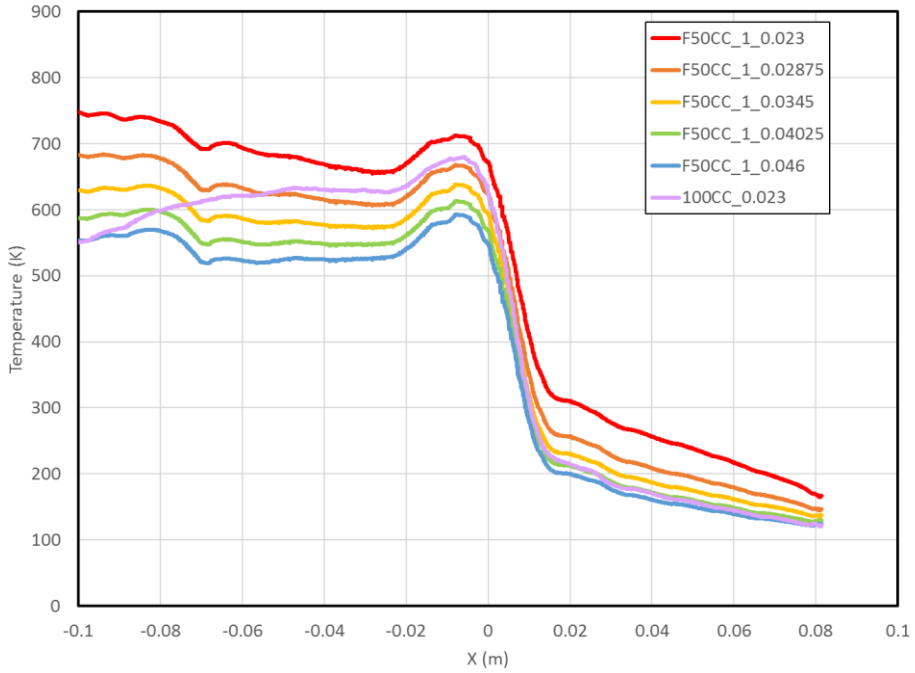

Figure 53: Liner 0°, Channel Mass Flow Varied (kg/s)

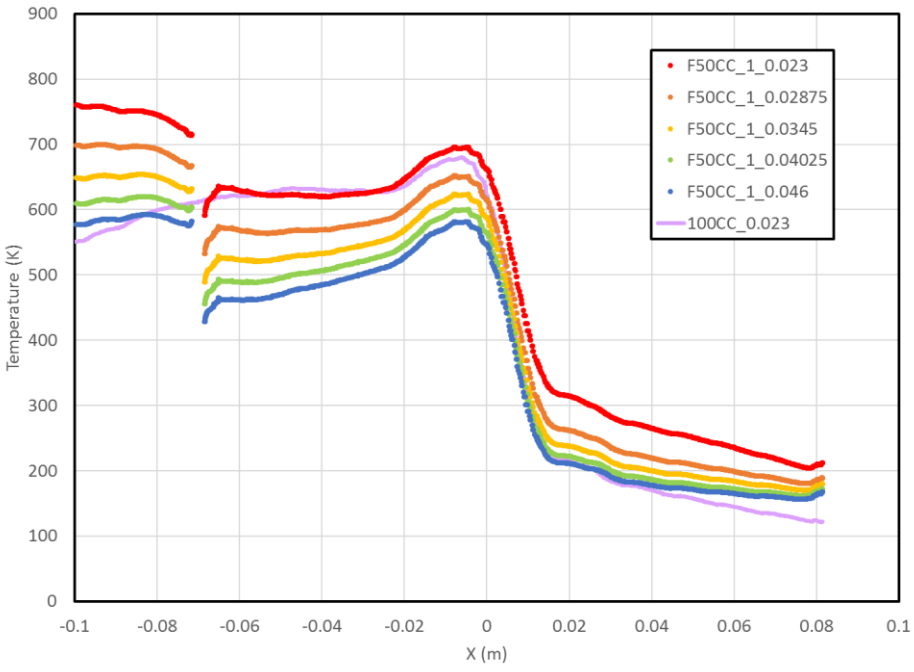

Figure 54: Liner 3.6°, Channel Mass Flow Varied (kg/s)

The maximum T_{gw} and number of cycles until failure are plotted vs flow rate of both the channels and film holes in Table 14. The blowing ratio for each case was also estimated using the properties obtained from the simulation and are tabulated in Table 14. The density ratio was approximately constant for all cases (DR=1.88).9

Table 14: Tgw Max Calculated Nf for Film Configuration Variations

	Film Flowrate (kg/s)	Blowing Ratio	Coolant Flowrate (kg/s)	Max T_{gw} (K)	Nf (cycles)
Variations of Blowing Ratio	0.0001	0.053	0.023	832	219
	0.00019	0.1	0.023	822	232
	0.00038	0.2	0.023	804	259
	0.00095	0.5	0.023	767	326
	0.0019	1	0.023	713	466
	0.00275	1.435	0.023	753	357
	0.00285	1.5	0.023	759	342
	0.0038	2	0.023	808	252
	0.0055	2.89	0.023	876	170
Flow Rate Variations of Coolant	0.0019	1	0.02875	668	639
	0.0019	**1**	**0.0345**	**638**	**798**
	0.0019	1	0.0403	613	971
	0.0019	1	0.046	593	1145

Analysis

After determining the best film blowing ratio, the best channel mass flow rate had to be determined. It is noted that the film blowing ratio of 1 and coolant flow rate of .046 kg/s is the "best" case in terms of minimum peak Tgw. However, with added mass flow comes added pumping power due to the added pressure drop across the cooling channel. Pumping power varies with mass flow rate in a cubic relation. If pumping power is increased drastically, a larger turbopump supplying the coolant would be required, which is added weight to the rocket engine. Added weight is a significant consequence when dealing with rocketry. Therefore, it is necessary to choose the best case with both pumping power and T_{gw} in mind. Looking back to the baseline configuration, the peak T_{gw} was 680K. The case using a per channel mass flow rate of 0.02875kg/s has a peak T_{gw} of 668K, which only cools the nozzle by an extra 12 K. The case with a per channel mass flow rate of 0.0345kg/s reaches a peak T_{gw} of 638 K, which is a reduction of 40K. Taking into account the fact that this configuration uses a total hydrogen mass flow rate (including both channels and film) of 1.82 kg/s compared to a total hydrogen mass flow rate of 2.3 kg/s for the baseline configuration, the best case is the film case with a channel mass flow rate of 0.0345kg/s.

50 Channels vs 100 Channels

In order to isolate and study the effects of reducing the number of channels by half, the 50 channels were simulated on their own at various flow rates without film cooling holes. The study was completed with the same variation in per channel mass flow rate (from 0.023kg/s to

0.046kg/s) as used for the film cooling configuration. The results of this channel flow rate variation are pictured in Figure 55.

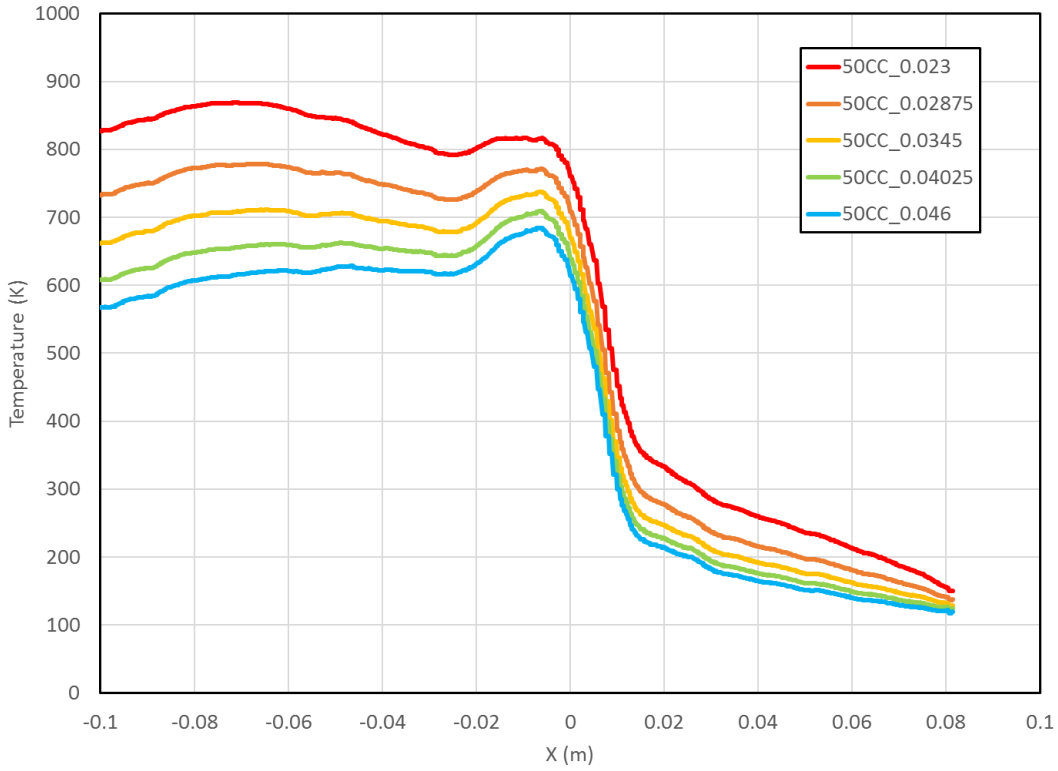

Figure 55: Temperature Profile of Nozzle with 50 Channels

As expected, temperature decreases with increased mass flow rate. $\dot{m}$ = 0.046kg/s, or double the original mass flow rate, shows a reduction in nozzle throat temperature of approximately 181K. The peak temperature for the $\dot{m}$ = 0.023kg/s case is at a different point than the $\dot{m}$ = 0.046 kg/s case. For $\dot{m}$ = 0.023 kg/s, the peak temperature is located at X = -0.074 m, while it exists at the throat of the nozzle for $\dot{m}$ = 0.046 kg/s.

In order to compare half the cooling channels to the baseline 100 channels, the baseline coolant flow rate was also varied at the same total mass flow rates, pictured in Figure 56. The

coolant mass flow rate was varied in the 100 channel design by decreasing from 2.3 kg/s to 1.15 kg/s in 5 even increments. This equates to a per channel mass flow rate reduction from 0.023 kg/s to 0.0115 kg/s.

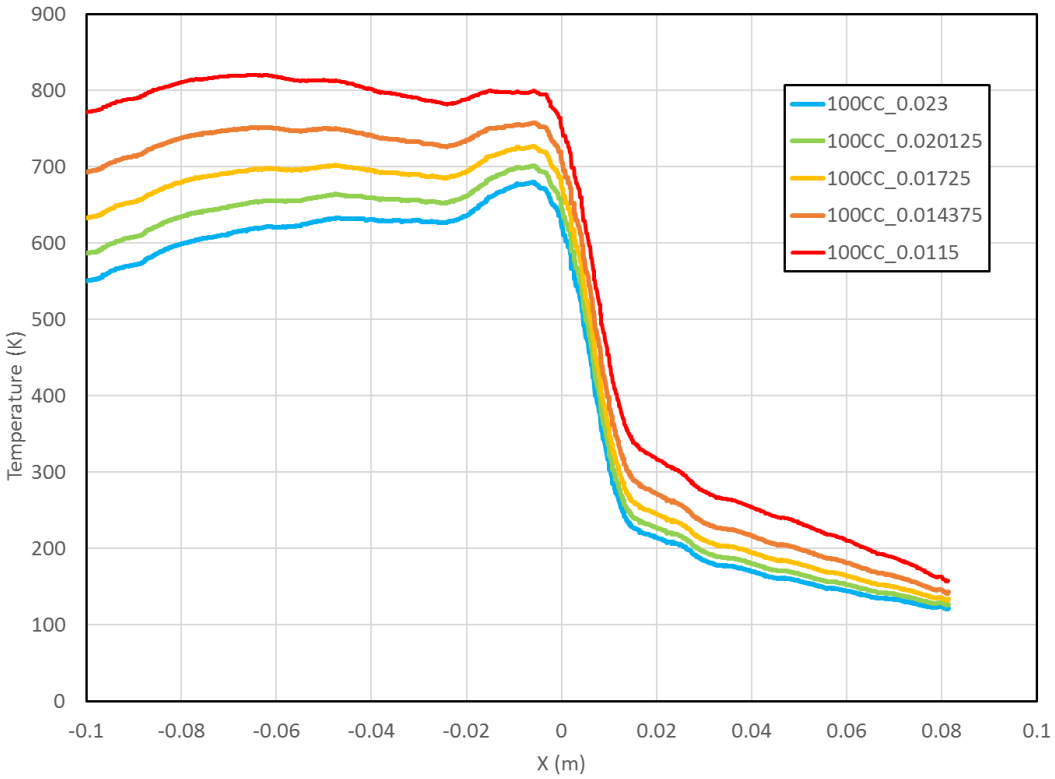

Figure 56: Liner Wall Temperature Distribution, 100 Channels Varied Mass Flow (kg/s)

Overall temperature distribution increases with decreased mass flow rate. The baseline configuration, with a total channel mass flow rate of 2.3kg/s, shows the lowest Tgw. The reduction in hydrogen mass flow through the cooling channels leads to a decrease in cooling performance, as expected.

Comparing the temperature distributions at the same total mass flow rates, it appears that the temperature profile trends of both the 100 channel and 50 channel configurations are

similar. In order to better analyze this trend, both designs were plotted on the same graph, Figure 57.

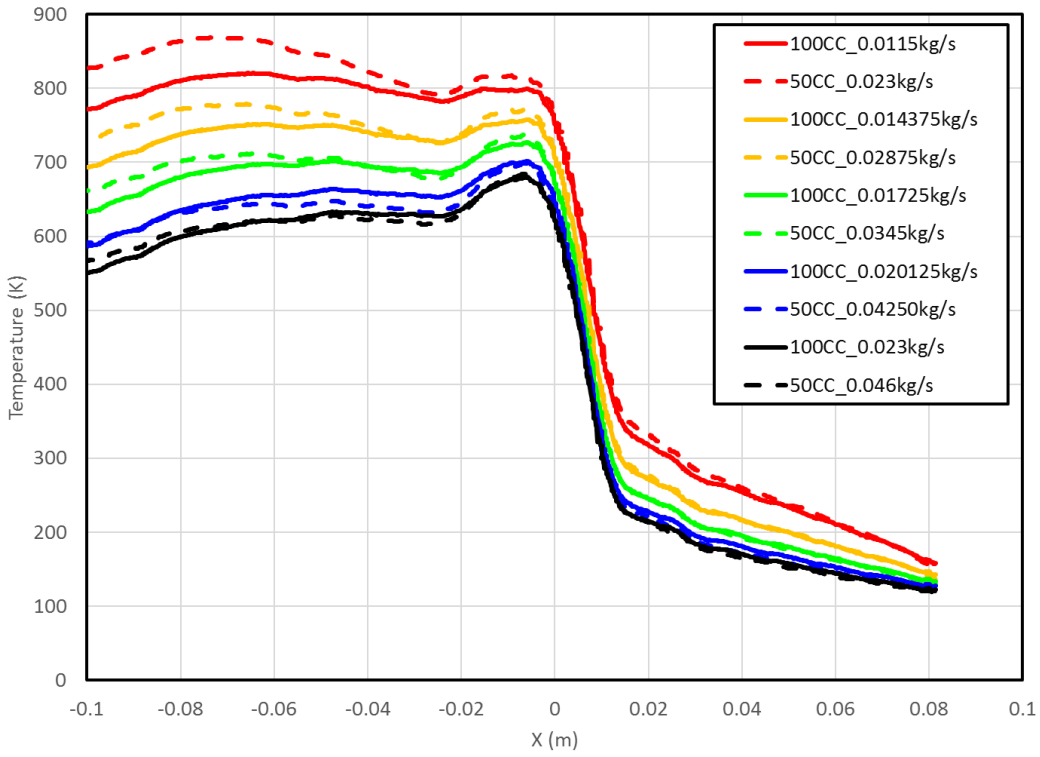

Figure 57: 100 Channel and 50 Channel Designs with Comparable Varying Mass Flow Rates

Figure 57 shows that, at the same total hydrogen mass flow rate, both the 100 channel and the 50 channel designs exhibit the relatively the same temperature profile trends. Since cooling effectiveness is relatively similar at the same total mass flow rates, it seems that the cooling resulting from regenerative cooling depends more on the mass flow rate rather than the number of channels. It is important to note that the geometry of the channels was not varied for this comparison: if a rocket nozzle were to use 50 channels for regenerative cooling, it is presumed that in a realistic situation, the channels would be better optimized for the 50

channel cooling configuration. This comparison shows the effect of varying the total mass flow rate and its dependency on number of channels of the same geometry.

Effects of Increased Channel Mass Flow and Blocked Channels

Naraghi et al. [65] have modelled the effects of a blocked channel using the Rocket Thermal Evaluation code; they modified an earlier version of RTE to calculate the temperature distribution for two half-ribs. The motivation for their study was to look into the influence of a single blocked channel onto the immediately adjacent channel. However, if periodicity is applied to their result, then an interesting comparison can be made. The results of Naraghi et al. can be interpreted as a rocket nozzle with half the coolant channels with no flow, similar to the necessary removal of half the coolant channels in the designs of the current work. Naraghi et al. noted that the additional heat load onto the unblocked cooing channel causes an increase in channel pressure drop, and the flowrate of this affected channel would have to decrease in order to have a pressure drop consistent with the remaining channels. The increased pressure drop effect is observed in the current work; the pressure drop is greater in a thrust chamber with 50 cooling channels at the same per channel mass flow rate as a thrust chamber with 100 channel. Since channel blockage effects were not the purpose of running simulations with 50 cooling channels, the matched pressure drop approach was not used and identical mass flows were used for the thrust chambers with 50 channels as with 100 channels.

Another notable difference is that, with the current approach, half the coolant channels have been removed and filled with copper whereas Naraghi et al. evaluated the cooling performance without filling in the channels, leaving voids. Filling the voids with copper material

adds additional conduction pathways for heat to be conducted through the liner; this effect was not considered by Naraghi et al. Since Naraghi et al. were trying to evaluate the performance penalty of an unintended channel blockage, their approach was sensible. With the current case however, the removal of 50 coolant channels was done intentionally in order to make room for the film cooling holes.

Pressure Drop: 100 Channels vs 50 Channels

Pressure drop at comparable total mass flow rates for both configurations was evaluated and recorded in Table 15. Pressure drop increases by 3.37MPa for the total mass flow rate of 2.3kg/s, and by 1.36MPa for the total mass flow rate of 1.15kg/s. The increased pressure drop is the result of two effects. Increasing the per channel mass flow rate increases the bulk velocity, which in turn increases losses due to friction. The increased heat load causes the fluid density to decrease more rapidly, which increases the velocity. This effect is apparent when comparing the total flow rate of 1.15kg/s for 50 channels vs 2.3kg/s for 100 channels. The increased heat load effect is why that, at these different flow rates for different number of channels, the 50 channel case has a higher pressure drop than the 100 channel case even though the per channel mass flow rate is the same at 0.023kg/s.

Table 15: Pressure drop of 100 Channels vs 50 Channels at Comparable Mass Flow Rates

Number of Channels	**Total Mass Flow Rate (kg/s)**	**ΔP (MPa)**
100	2.3	1.35
50	2.3	4.72
100	1.15	0.55
50	1.15	1.91

TURBULATORS IN COOLING CHANNELS

While a decrease in max Tgw from the baseline configuration of 680K to 638K using the combined regenerative and film cooling design is an improvement of 6% in max Tgw (and in increase of 36% using the Nf correlation), the best case film cooling configuration did not meet the goal temperature of 613K. However, this is not an optimized case–there is still room for improvement. One of the ways that cooling effectiveness can be improved is by adding turbulators to the cooling channels themselves.

The difference in temperature between the coolant at the top of the channel and the coolant at the bottom of the channel is large. By turbulating the flow, this hot and cold coolant can be mixed, reducing the temperature of the coolant by the hot gas side wall and thereby increasing heat transfer. There are several ways to turbulated the flow, but this design will use rib turbulators.

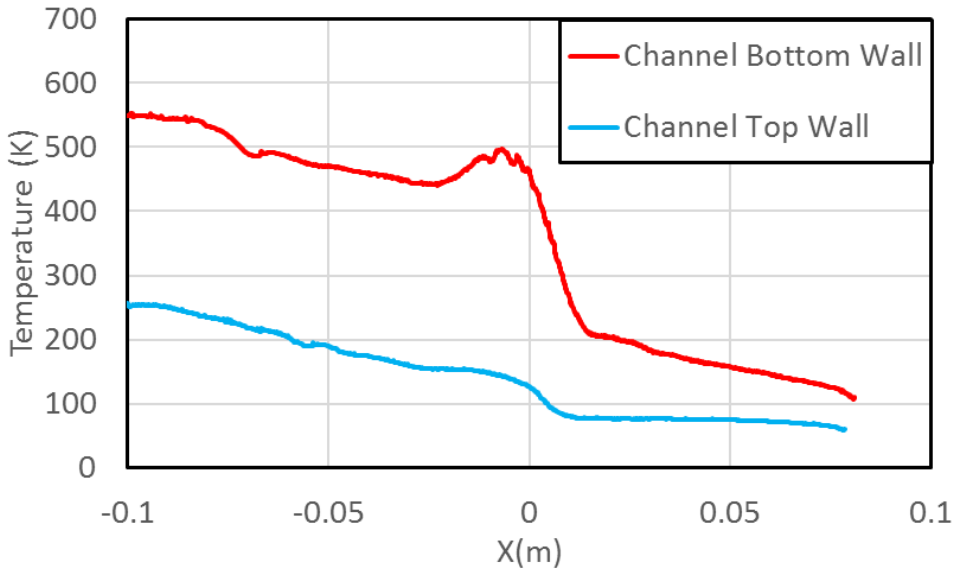

Figure 58: Channel Temperature Profile, Top Wall vs Bottom Wall

The rib turbulators design used in this thesis is based on a geometry utilized by Tran et al. [66], a representative design for gas turbine blades. The rib pitch to height ratio (p/e) was 10, and the channel height to rib height ratio (H/e) was 10. The channel height was equal to the rib pitch.

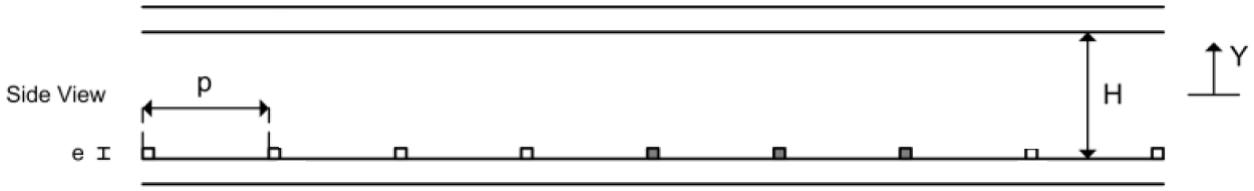

Figure 59: Schematic of Rib Turbulators [49]

The ribs are square, located on the bottom wall of the channel and oriented orthogonal to the flow. Tran et al. studied ribs in a constant area channel. In this thesis, the channel height is not constant and the channels themselves are curved. The channel curvature effects were not considered when determining rib placement. In order to determine the rib height, the local channel height was determined at each rib location, which requires marching and iterating.

Placement of Turbulators

Turbulators can be designed using only marching if it is known where the first rib will be placed. For this thesis, the first rib needed to be located just before the throat in order to cool the maximum hot gas-side wall temperatures. In this thesis, the second rib was placed arbitrarily at the throat, and the first rib is placed one rib pitch upstream from the throat rib. The rib position and rib height were then iterated to determine the exact location of the first rib. This iteration process can be bypassed if the location of the first rib is known. In order to determine the location of ribs in a nozzle, one must first choose a relative pitch, p/e, and

relative rib height, e/Dh (or e/Dh). The selection of these factors is normally a part of an optimization process in order to determine the best setup for each case. With these parameters, starting at the starting location of the ribs, the local channel height should be found and the respective local rib height find using the following procedure. The relative pitch of 10 will be used for the equations. The relative rib height is given by Eqn. (59). Equation (59) can be rearranged into a more directly useful form, Eqn. (60), to calculate the rib height directly from the local channel height. The relative rib pitch is usually shown as Eqn. (61), but it can also be rearranged into Eqn. (62).

$$\frac{e}{H} = 0.1 \tag{59}$$

$$e = 0.1H \tag{60}$$

$$\frac{p}{e} = 10 \tag{61}$$

$$p_1 = 10e_1 \tag{62}$$

If X_1 is the coordinate location of the 1st turbulators. Determine the channel height at X_1 from the known geometry of the cooling channel. From the channel height, Eqn. (60) is used to determine the rib height at that location. Then, the rib pitch is determined from Eqn. (62) which allows the location of the subsequent rib to be determined from Eqn. (63).

$$X_2 = X_1 + p_1 \tag{63}$$

This procedure is repeated for all subsequent ribs to determine the rib heights and spacing between the remaining ribs. This method can also be applied for any values of relative pitch and relative rib height. These parameters can also be varied within a design (a locally

varying relative rib height and relative rib pitch). In this study, a constant relative height and relative pitch were used. For the design studied in this thesis, ribs were placed up to the location of the film holes, which amounted to 16 ribs total. The parameters calculated are tabulated in Table 16. A visual representation of the ribs in the simulation itself is displayed in Figure 60 and Figure 61.

Table 16: Locations and Dimensions of Each Rib (in)

Rib	X	H	e	P
1	0.174	0.1739	0.0174	0.1740
2	0.000	0.1739	0.0174	0.1740
3	-0.174	0.1739	0.0174	0.1740
4	-0.348	0.1739	0.0174	0.1740
5	-0.522	0.1751	0.0175	0.1750
6	-0.697	0.1841	0.0184	0.1840
7	-0.881	0.1935	0.0194	0.1940
8	-1.075	0.1961	0.0196	0.1960
9	-1.271	0.1980	0.0198	0.1980
10	-1.469	0.1990	0.0199	0.1990
11	-1.668	0.1999	0.0200	0.2000
12	-1.868	0.1960	0.0196	0.1960
13	-2.064	0.1953	0.0195	0.1950
14	-2.259	0.1819	0.0182	0.1820
15	-2.441	0.1786	0.0179	0.1790
16	-2.620	0.1786	0.0179	0.1790

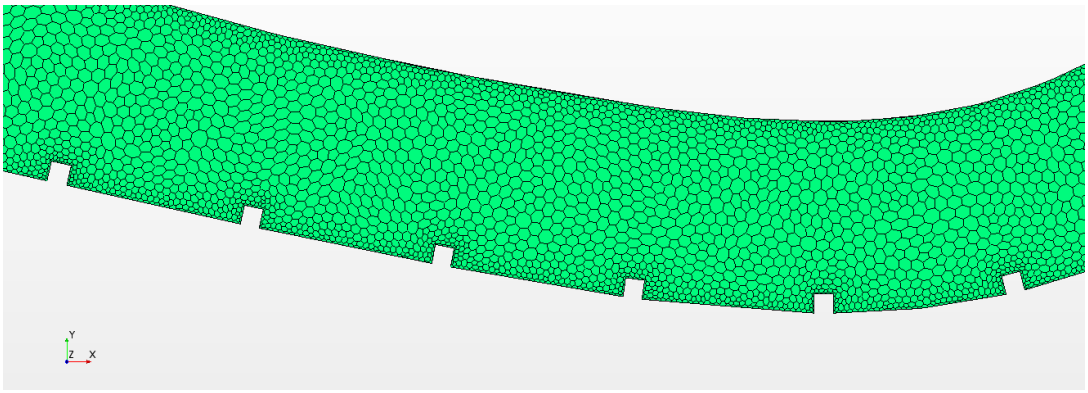

Figure 60: Channel Mesh including Turbulators (flow runs from right to left)

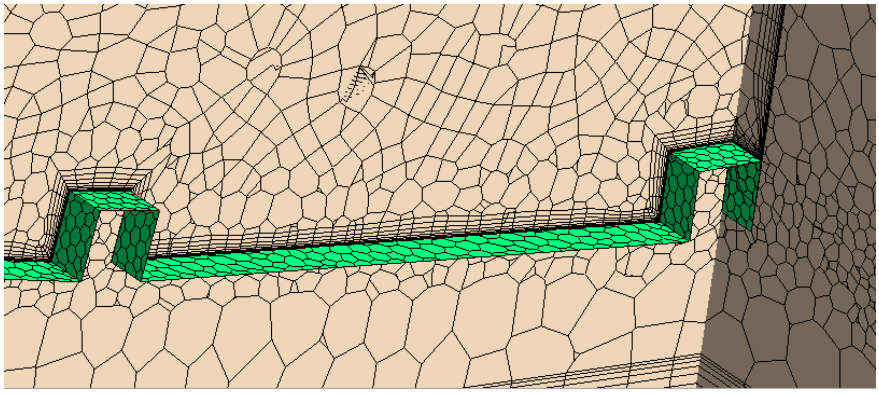

Figure 61: Slice of Channel and Liner mesh to Show Mesh and Geometry of Turbulators

Turbulators in 100CC (100CCT)

The turbulated channel design was first implemented on the baseline configuration of 100CC. The mass flow rate was varied from 0.0115kg/s per channel to 0.023kg/s per channel, as per previous mass flow variations. The liner temperature profile is pictured in Figure 62. These results are compared with the baseline configuration and the film configuration at the same per channel mass flow rate in Figure 63.

.

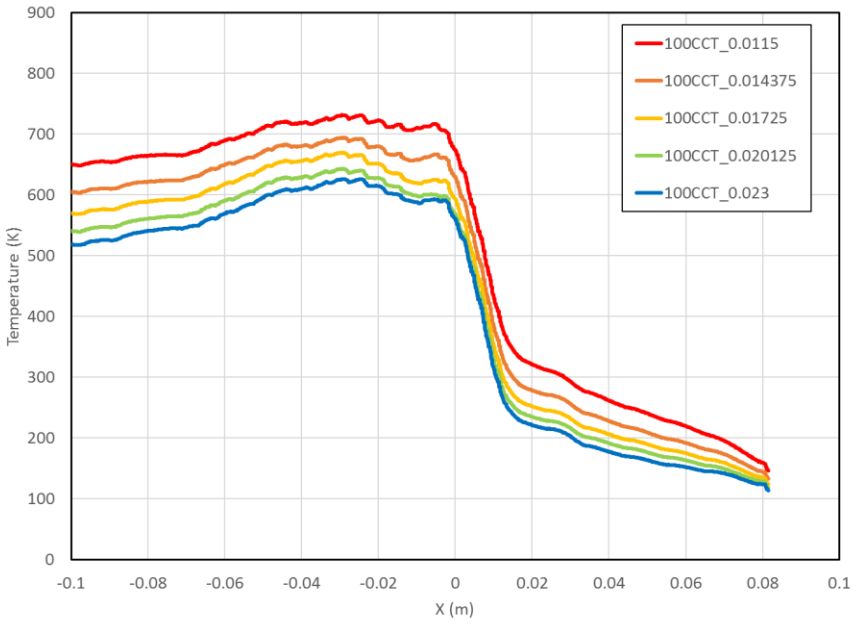

Figure 62: Liner Wall Temperature Profile of 100CCT with Varied Channel Mass Flow

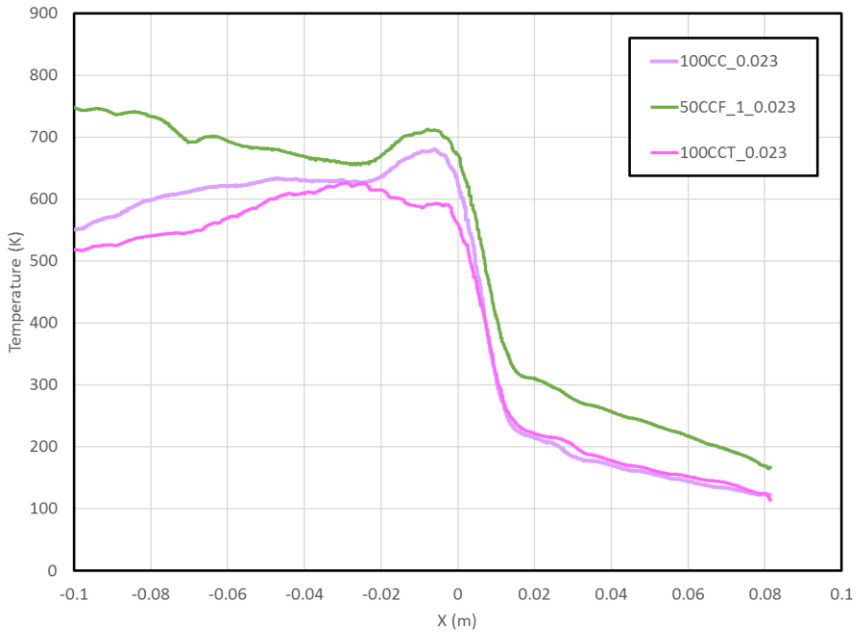

Figure 63: 100CC Turbulated vs the Baseline and the Film Cooling Design at the Same Per Channel Flow Rates

This temperature profile shows that the turbulated high aspect ratio cooling channels at comparable mass flow rates performs better than both the baseline and the film cooling (with 50 channels) design. The peak temperature was reduced to 626K, and moved from the nozzle throat to the point further upstream the thrust chamber. 100CCT did not perform better past the throat, which is expected since there are no turbulators at the diverging section of the nozzle. 100CCT improved the cooling effectiveness greatly from the throat at X=0 to the channel outlet.

It should be noted that, with comparable per channel mass flow rates, the film cooling design results in a total mass flow rate of 1.82kg/s, as opposed to the total mass flow rate of 2.3kg/s for the baseline and 100 turbulated channel designs.

Film and Turbulators (100CCFT)

The turbulated cooling channel design was then implemented to the film cooling design. The ribs are located at the same region of the cooling channels, however there are 50 channels instead of 100 channels. The nozzle configuration consisting of internal cooling with added turbulators and film cooling was run at channel mass flow rates of 0.023 kg/s to 0.046 kg/s. The pressure drops for higher mass flow rates were much higher, and these simulations had a greater tendency to diverge. Because of this, intermediate iterations had pressure drops upwards of 20 MPa before the solution converged, and so the property tables for hydrogen had to be extended up to 21MPa to improve the stability of the simulation. The liner wall temperature distributions for these combined turbulated and film cooled cases is compared with the baseline design, depicted in Figure 64.

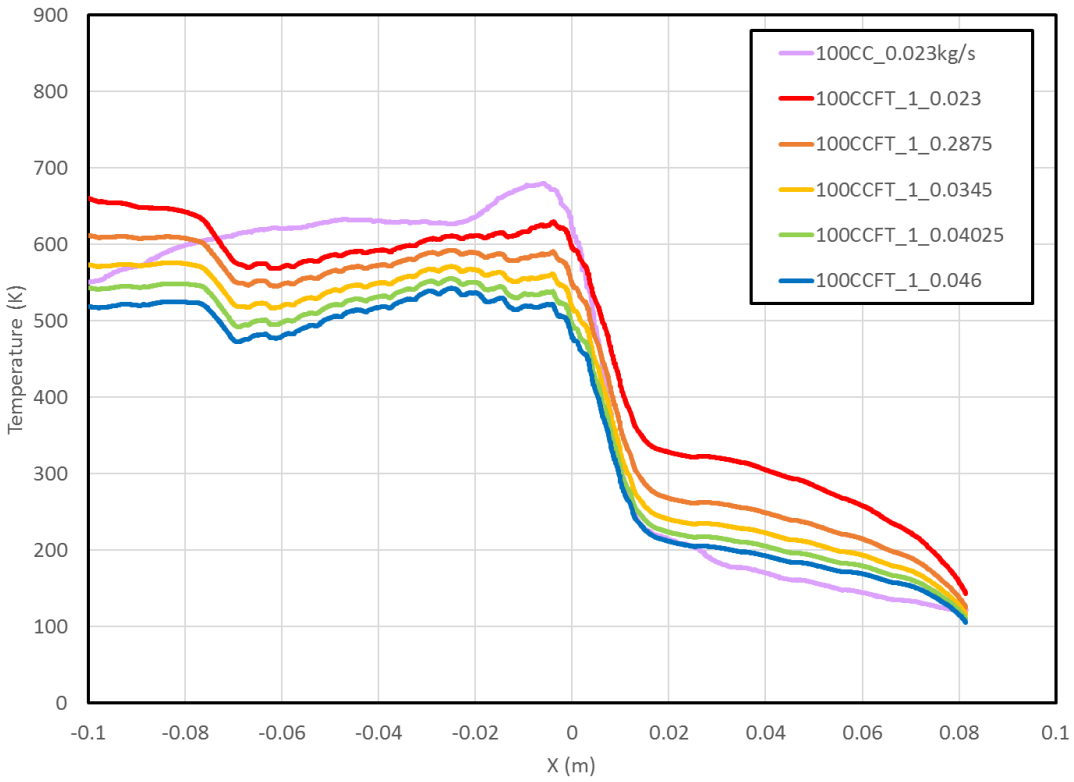

Figure 64: 50CCFT at Varying Channel Mass Flows

Even though there were only 50 channels, all of the 50CCFT cases performed better than the baseline case. With a coolant flow of 0.023 kg/s per channel, the maximum Tgw was 630K, with a corresponding estimated Nf of 849. When the coolant flow is increased to 0.046kg/s, the maximum Tgw is reduced even further to 543K, corresponding to an Nf of 1761.

Results show that temperature was reduced at -0.07>X>0 m. This reduction is because the film cooling begins at approximately X=-0.07m (2.75in), which drives down the liner wall temperature. Turbulators help keep the temperature further reduced where they are located, from X=-2.62in to X=0.174in. The temperature is higher at the diverging point of the nozzle

since there are only 50 channels instead of the full 100 channels at the same baseline per channel mass flow rate. The lack of channels upstream also explains the higher temperature preceding the turbulated cooling channel flow and film cooling. With a per-channel flow rate of 0.023kg/s for 50CCFT, this design uses half the coolant for regenerative cooling channels compared to the baseline configuration, while improving cooling effectiveness compared to the baseline significantly.

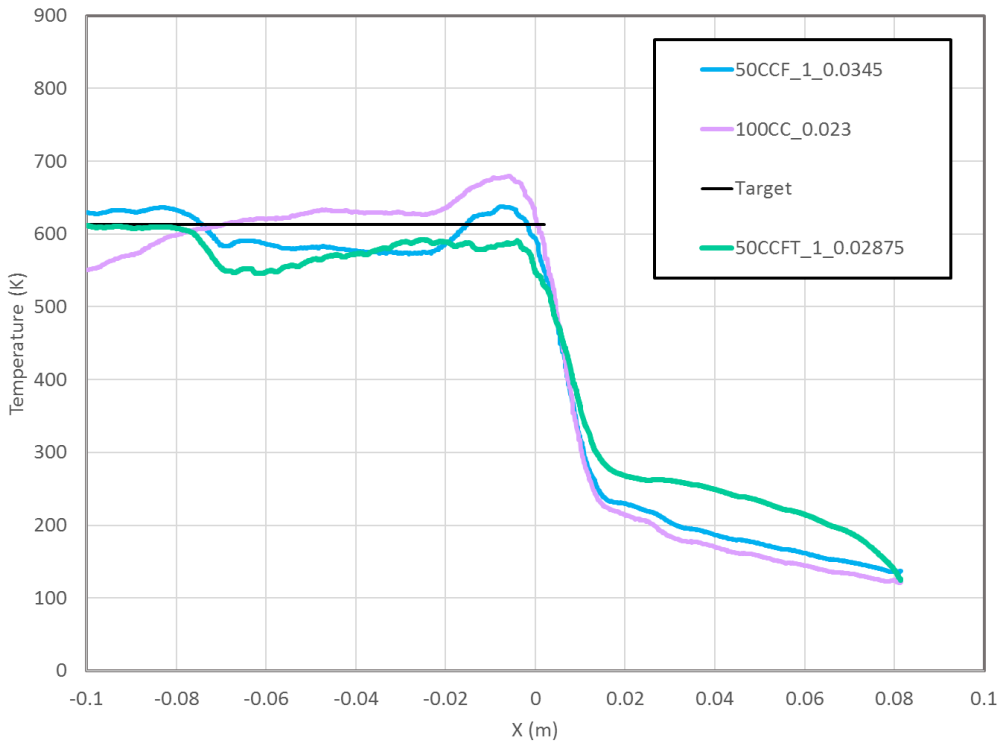

Figure 65: 50CCFT at Per Channel Mass Flow of 0.02875kg/s Compared to Film Best Case and Baseline

It is important to note that using film cooling alone, the temperature could not be cooled lower than the baseline liner temperature at the same flow rate. However, once turbulators are added to the cooling channels, this configuration can indeed cool the nozzle better than the baseline configuration with half the total flowrate in the cooling channels. The cooling

performance of 50CCFT increases with increased per channel mass flow rate, and at 0.02875kg/s per channel, the design reduces the wall temperature 592, which finally meets the cooling target of this thesis. Further increases in the channel flow-rate led to an overcooled nozzle and it was not necessary to increase the flowrate beyond 0.02875 kg/s. This is in contrast with the film cooled configuration, where the coolant flow had to be increased to 0.0345 kg/s to maintain similar performance to the baseline case, whereas the 50CCFT configuration already exceeds the performance of the baseline case even at a flow-rate of 0.023 kg/s. This design at this per channel mass flow rate, while using less total mass flow rate than both the baseline and the film cooling configuration, cools the nozzle better, meaning this cooling configuration is more efficient. The sharp temperature increase at the throat seen in other cooling designs does not occur because the enhanced heat transfer from the added turbulators is cooling this region. However, this improvement does come with an increase in pressure drop and an increase in manufacturing complexity.

DISCUSSION

Comparison

In order to ensure that each simulation can be measured against one another accurately, properties measured at the centerline of the nozzle were compared. These properties should remain the same despite different cooling methods, as the influence of both film cooling and internal cooling is primarily on the wall and s not reach the center of the nozzle. Static temperature (Figure 68), total temperature (Figure 66), and Mach number (Figure 67) were compared alongside the optimal film sim, 100 channel simulation, 50 channel simulation, and injector simulation.

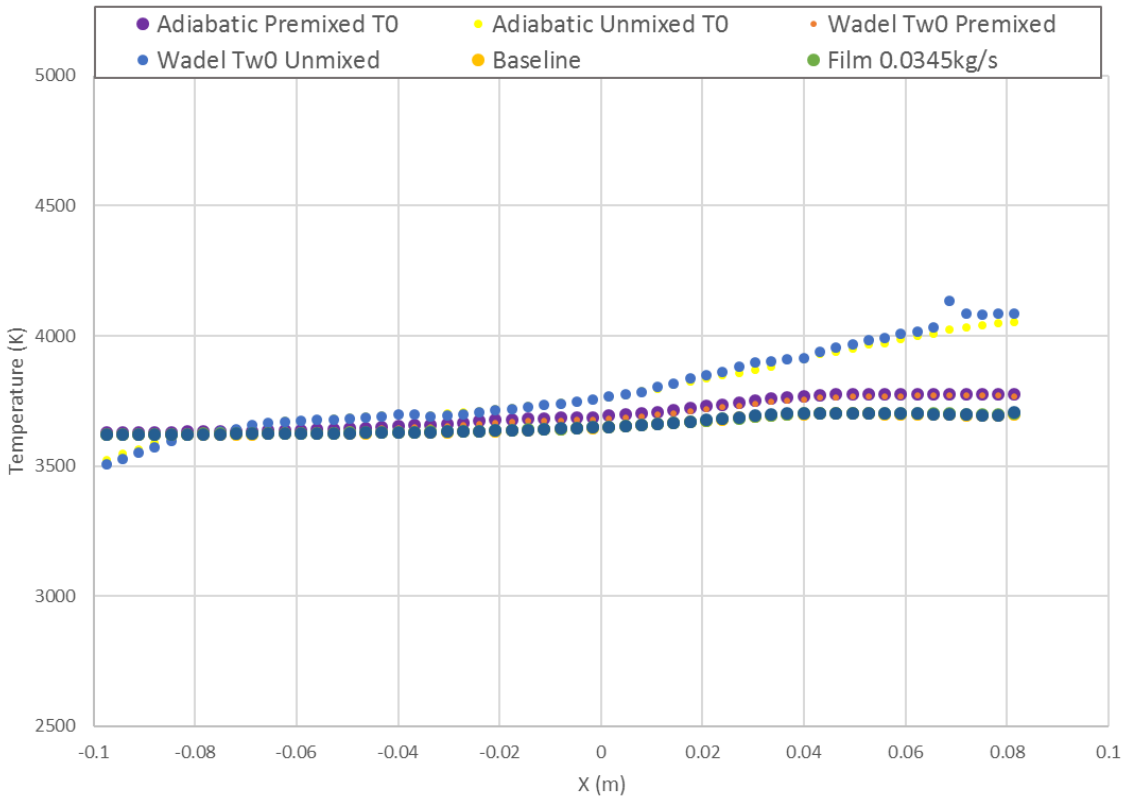

Figure 66: Centerline Total Temperature Comparison

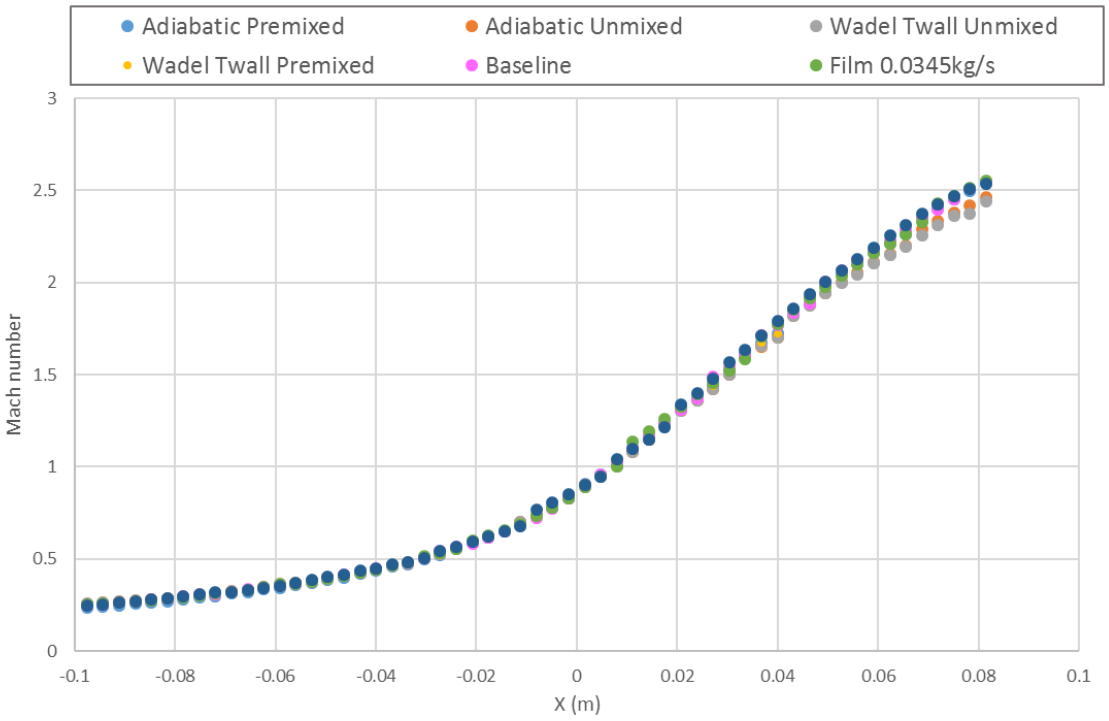

Figure 67: Mach Number Comparison

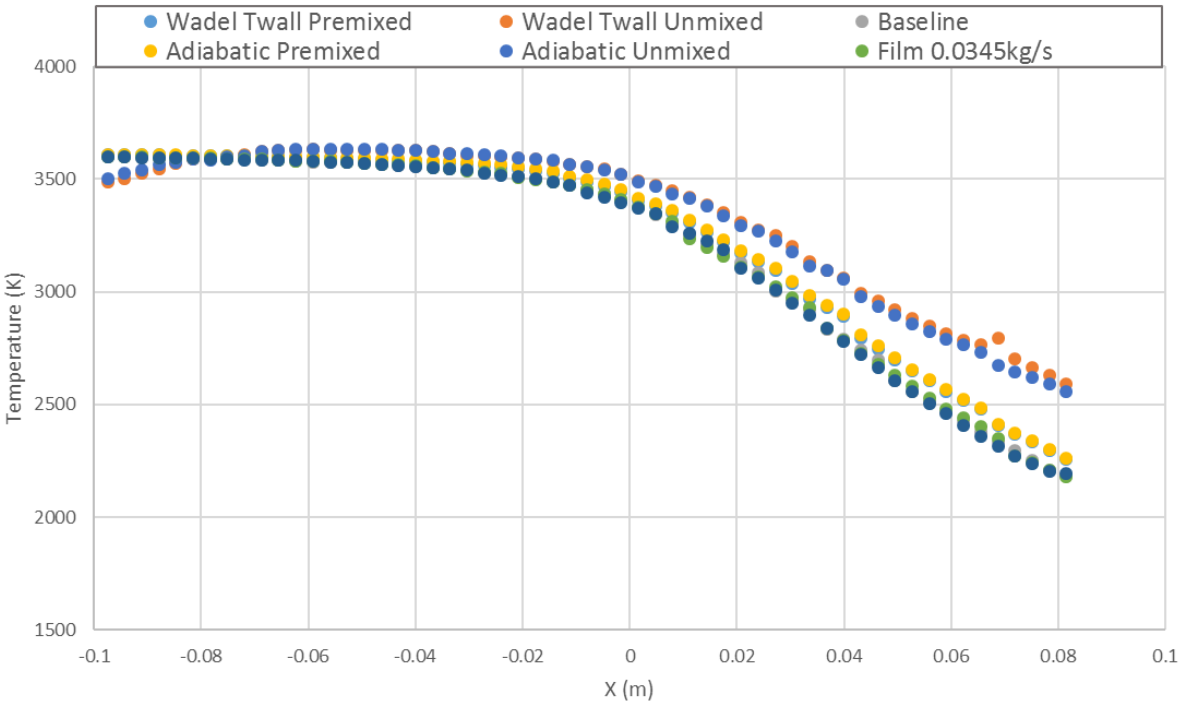

Figure 68: Centerline Static Temperature Comparison

From these charts, it is confirmed that the different cooling designs are comparable from X=-0.1 onward, therefore the thrust is similar, and the effectiveness of each cooling configuration can be compared.

Baseline Channel Flow Rate Cases

First, configurations were compared with the same mass flow rate for each at the nominal per channel mass flow rate of 0.023kg/s, shown in Figure 69.

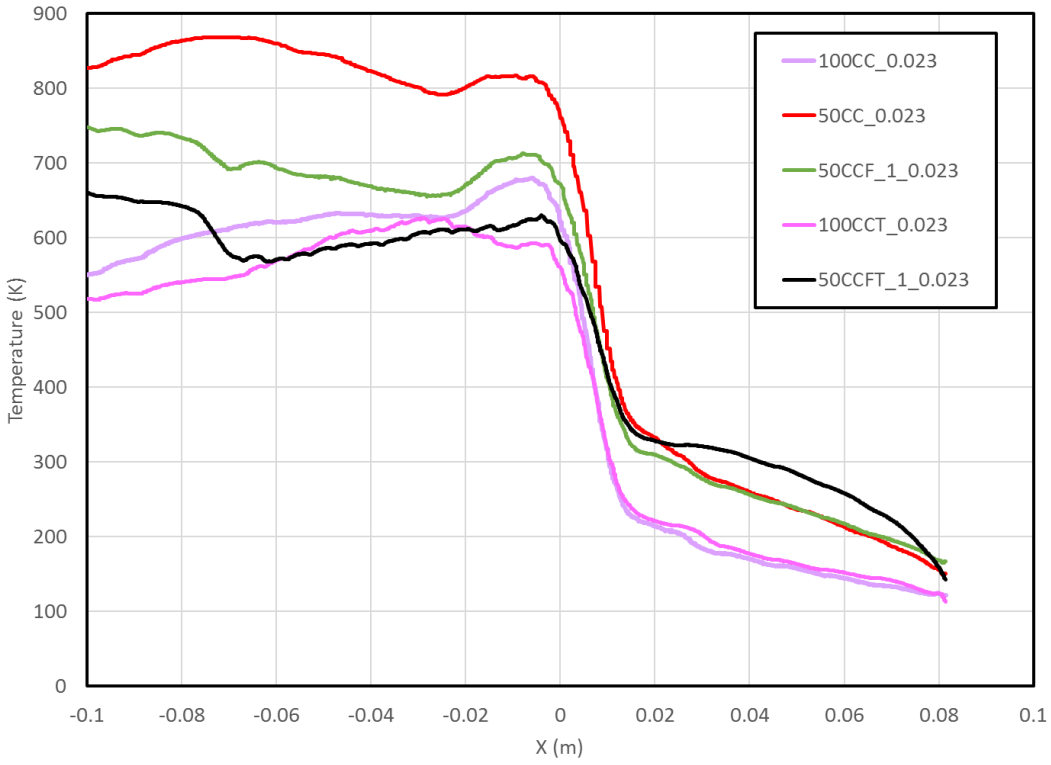

Figure 69: Designs Compared at 0.023kg/s Per Channel Mass Flow Rate

According to this representation, it seems that the turbulated designs produce the most improved cooling configuration. Film cooling at the same per channel mass flow rate does not cool better than the baseline configuration. While the film cooling configuration does improve cooling upstream of the throat, it does not improve cooling at the throat since the film is too far

upstream to affect the throat significantly. 50 channels on their own with no added film cooling or turbulators cools the worst. However, it is important to remember that at the same channel mass flow rate, the designs with 50 channels are utilizing half the total coolant compared to 100 channel configurations. 100CCT, while having a higher pressure drop for 100 channels, applies better local cooling near the throat when compared with the baseline design. However, this design is not as effective between -0.05m<X<-0.025m. Since this design uses 100 channels, the channel mass flow rate does not need to be varied in order to produce better cooling if one can afford the pressure drop across the channel.

50CCFT, combining the turbulated design with the film cooling design, combines the advantages of both designs by utilizing broad cooling upstream from film holes and targeted cooling at the throat from the turbulated channels. While turbulators produce mostly local cooling, this local cooling can be expanded by adding multiple ribs (such as the 16 turbulators used in this study). Of all the configurations examined with 50 channels, only with 50CCFT does the cooling configuration cool better than the baseline without needing to alter channel mass flow rates and. This conclusion shows that there is a way to improve cooling further and still use less coolant using combined film cooling and turbulated channels. Improving cooling effectiveness with less coolant is important to consider when applying advanced cooling configurations to thrust chambers with extremely high heat loads where the size of the rocket nozzle is limited by the amount of coolant available. Using combined film cooling and turbulated cooling channels paves the way for larger rockets to be used for launching larger payloads into space.

Comparable Total Flow Rate Cases

Pictured below are the configurations at the same total channel mass flow rate of 1.15kg/s:

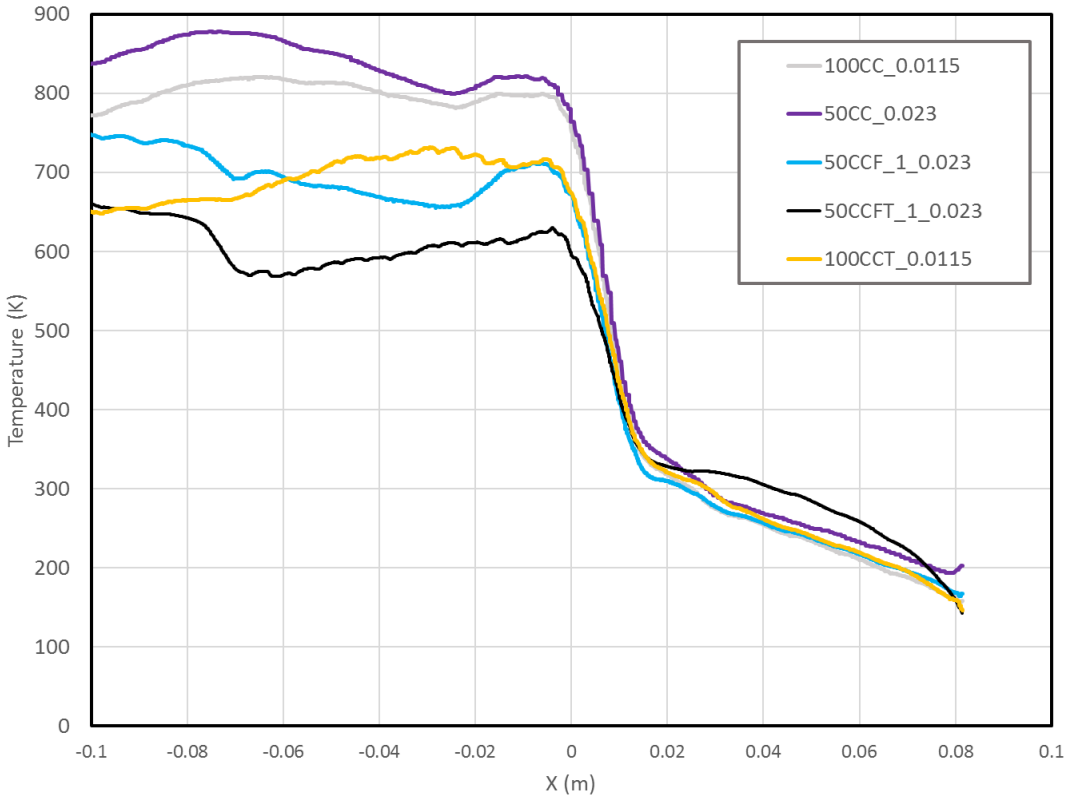

Figure 70: Hot Gas Side Wall Temperature Comparison, Comparable Mass Flow Rates

Figure 70 shows that, with comparable mass flow rates of 1.15kg/s, the modified cooling configurations including film cooling and turbulators all outperform the baseline configuration of 100 channels (or 50 channels at 1.15kg/s total mass flow rate). If there is need for less coolant in a rocket nozzle, the advanced designs proposed in this thesis could improve cooling using far less coolant.

Best Cases

Results for the best case for each configuration were plotted against one another to compare T_{gw}temperature profiles in Figure 71. The temperature profile for 100 cooling channels at the original flow rate is also plotted to be able to compare results to the baseline. Recall that the designs with 50 cooling channels had to also overcome the cooling deficit of reduced number of cooling channels and total coolant flow rate.

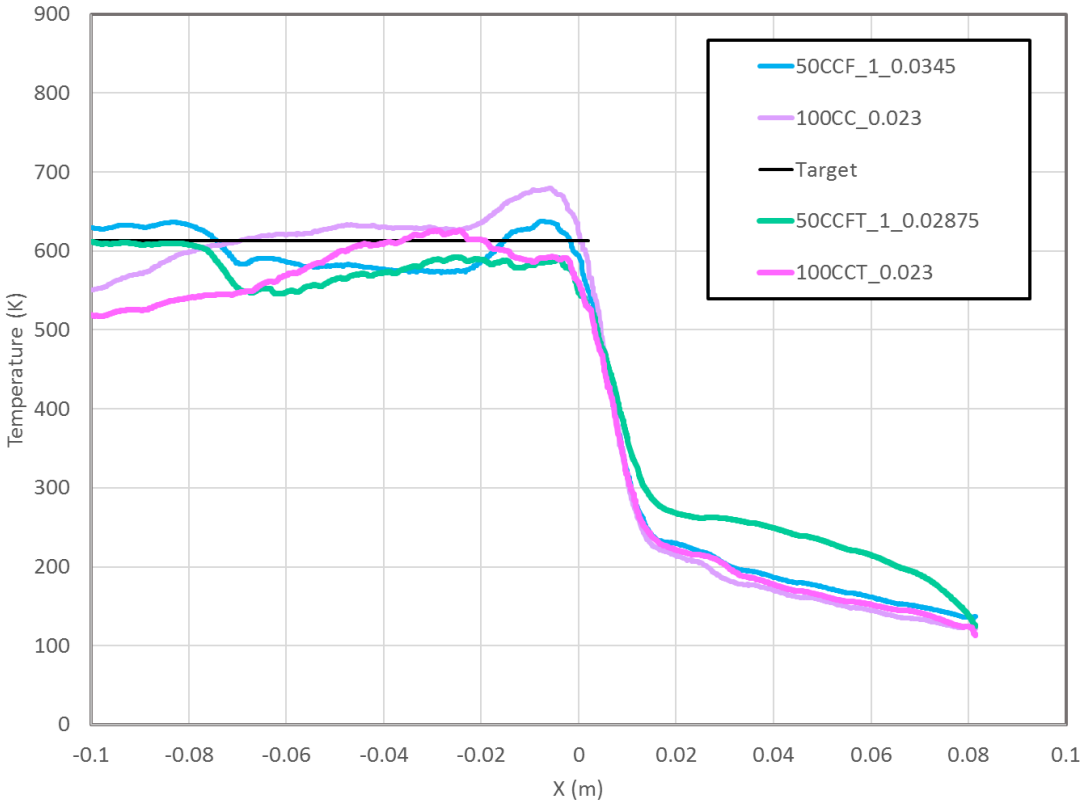

Figure 71: Design Best Cases

The cases in Figure 71 include the film cooling design at a per channel mass flow rate of 0.0345kg/s, or a total mass flow rate including film cooling of 1.82kg/s, 100CCT at a total mass

flow rate of 2.3kg/s, and 50CCFT at a total mass flow rate of 1.5325kg/s. Compared to the baseline, all advanced cooling designs reduced the Tgw. 50CCF proposes a design that does not require the complex machining required by turbulated designs. 100CCT is a design that allows for the inclusion of all 100 channels while improving cooling with turbulators that do not alter the geometry of the nozzle. 50CCFT is a combination of both, offering the cooling benefits of both turbulators and film cooling.

The maximum Tgw were calculated and tabulated for all best case designs in Table 17. Nf was also included to show how a reduction in Tgw can drastically increase the life of the nozzle. The 50CCFT configuration met the cooling target of 613K by reducing the temperature to 592K. Considering the target Tgw, this is actually over-cooled, and so further modifications can be made by reducing cooling mass flow if needed. The configuration with film cooling but no added turbulators and the configuration with turbulators but no film both were able to reduce the maximum Tgw compared to the baseline case, but neither were able to exceed the 613K target.

Table 17: Tgw and Nf for Best Cases

Configuration	Tgw,max	Nf
100CC	680	586
50CC	638	798
100CCT	626	876
50CCFT	592	1149

Pressure Drop

For the configurations simulated, the cooling channel pressure drop is plotted versus per channel mass flow rate in Figure 72 and versus overall flow rate in Figure 73. Varying the film blowing ratio does not significantly affect the pressure drop across channels. However, the addition of film cooling does marginally decrease the pressure drop seen in the channels. This decrease is due to the reduced thermal loading on the regenerative cooling channels. Adding turbulators increases the pressure drop, which is due to both the increased thermal loading and viscous losses, since the enhanced mixing gives way to more viscous losses. In order to have similar cooling performance to the 100 channel configuration, the 50 channel design must have increased mass flow, which is why the pressure drop is on the upper-right portion of Figure 72.

Analyzing the pressure drop at the same per channel mass flow rate of 0.023kg/s can help with assessing the effect of thermal loading on the pressure drop. 100 channels at this per channel mass flow rate has the lowest pressure drop, and the 50 channel design has a significantly higher pressure drop, which is lowered slightly with the introduction of film cooling. The addition of turbulators to the 100 channel design increases pressure drop via thermal loading and friction factor. Combining the effects of turbulators with the 50 channel configuration (50CCFT) yields the highest pressure drop due to the combination of the effects from the turbulators and low number of cooling channels. Figure 72 helps to visualize the detailed physics of various effects. If one is considering the overall performance of the nozzle, it may be more helpful to compare the pressure drops for total coolant mass flow rates, as in Figure 73.

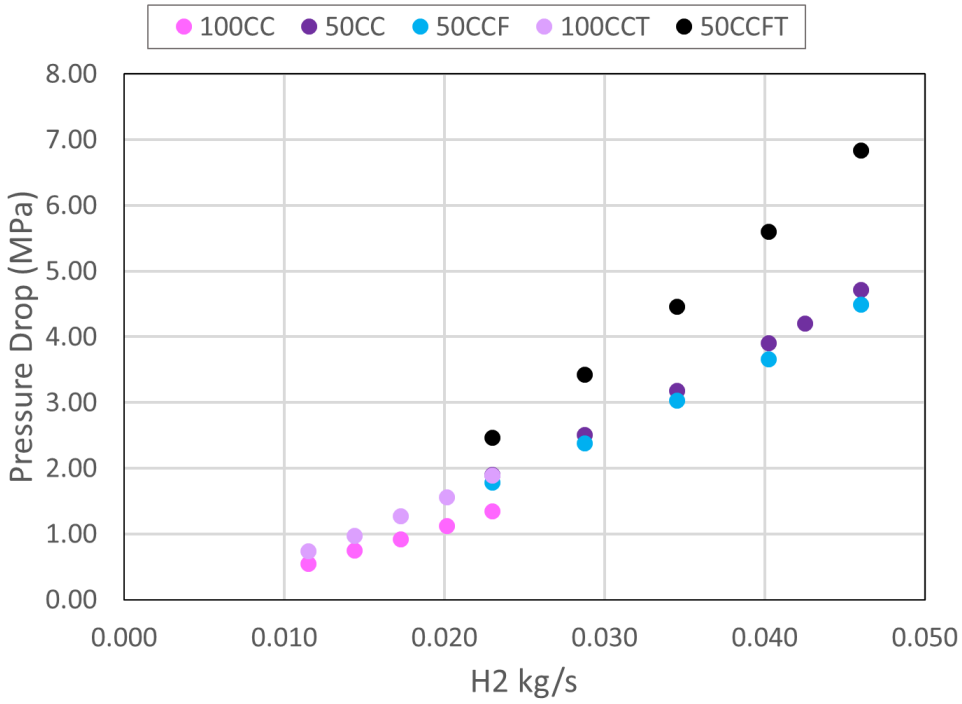

Figure 72: Pressure Drop for Relevant Cases at Varying Channel Mass Flow Rates

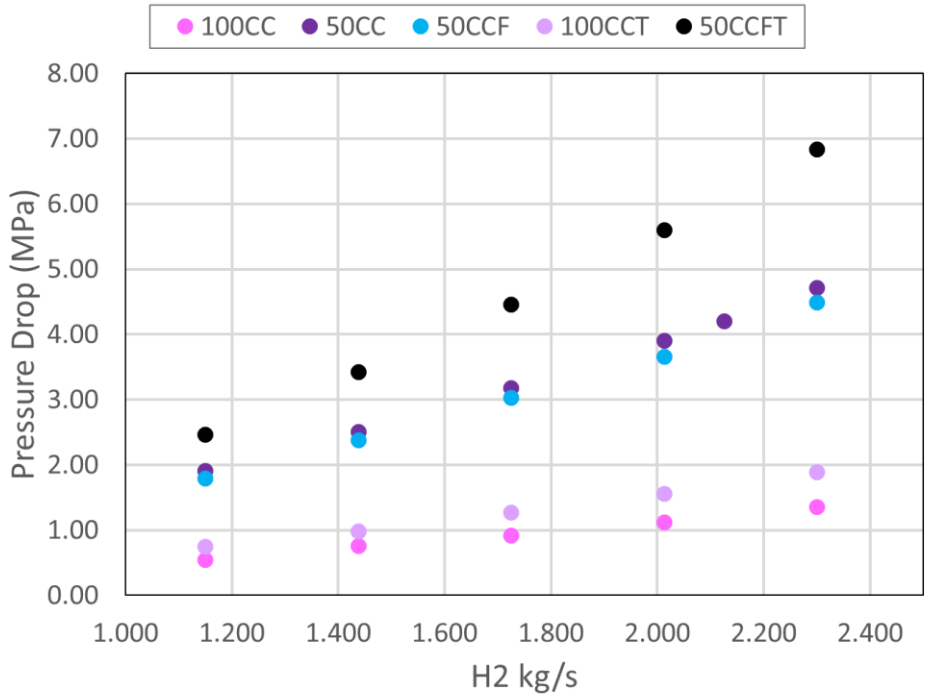

Figure 73: Pressure Drop with respect to Total Mass Flow Rates

The pressure drop per channel was calculated for each configuration at various channel mass flow rates and relevant cases are tabulated in Table 18. Pressure drop inevitably increases with increased mass flow. The maximum pressure drop is seen for 50 channels at 0.046kg/s per channel mass flow rate at 4.72MPa.

Table 18: Pressure Drop Per Channel

Design	Total Channel Mass Flow Rate (kg/s)	ΔP (MPa)	ΔP Increase from Baseline (MPa)
100CC	2.3	1.35	0
100CC	1.15	0.55	-0.8
50CC	2.3	4.72	3.37
50CC	1.15	1.91	0.56
50CCF	1.175	3.04	1.69
100CCT	2.3	1.89	0.54
50CCFT	1.15	2.47	1.12

Objective Cooling

The effectiveness of a cooling scheme is fairly simple to assess. Different regenerative cooling schemes can easily be compared by an overall-average heat transfer coefficient (or Nusselt number). For film cooling, an extremely useful metric is the film cooling effectiveness, Eqn. (64).

$$\eta = \frac{T_\infty - T_{aw}}{T_\infty - T_{c,exit}} \tag{64}$$

The effectiveness is zero when the wall is equal to the hot gas freestream temperature (or recovery temperature, depending on interpretation) and unity when the wall temperature is equal to the film coolant temperature. Thus, film cooling effectiveness is a measure of how close the wall temperature is to the film temperature versus the hot gas recovery temperature.

Additional metrics (some derived from thermodynamic principles) can include the penalty needed to achieve the added cooling effectiveness. An example is the thermal performance, Eqn. (65), often used in internal cooling. The thermal performance is the ratio of heat transfer improvement to ratio of pumping power expended. The thermal performance belongs to a broader class of Performance Evaluation Criteria (PEC), which is discussed in detail by Webb [67].

$$TP = \frac{Nu/Nu_0}{\sqrt[3]{f/f_0}} \tag{65}$$

These effectiveness and performance metrics, however, are insufficient for design studies because they do not incorporate design constraints and objectives into their definition, which is especially important for design optimization studies. When a design needs to be engineered to meet a specific target within certain constraints, the constraints can easily be established as the bounds of the optimization process. The more difficult problem is how to evaluate how well a particular design succeeds in meeting a particular cooling target.

The task of the engineer is to design a nozzle able to survive a specific number of cycles to failure (via limiting the maximum Tgw to less than a specific target, 613K in this thesis). A design engineer is not necessarily interested in a cooling design which maximizes cooling (i.e. minimizes Tgw), although it is understood that maximizing the cooling is a reasonable approach to achieving this goal. This process is outlined in a hypothetical situation in Figure 74. The red curve denotes the liner wall temperature for some given baseline. The dashed blue curve is the targeted wall temperature that the design engineer would like to achieve. This target can be an

arbitrary curve but is depicted as a trapezoid to demonstrate different desired targets in different regions. The target may not be completely below the baseline, as the baseline may already exceed the targeted conditions in certain regions. There may also be multiple tiered cooling targets corresponding to different cost-thresholds for a modular design study. For example, if a low enough temperature can be maintained throughout the liner (Tgw < 800 K), copper can be used as the liner material without needing to resort to more expensive nickel-based superalloys. However, if this temperature threshold is not feasible (or is not cost-effective), then a higher temperature threshold may be established (corresponding to the allowable material temperature limit of Nickel or Inconel instead of OFHC Copper). Designs that are feasible with copper form one module or design sub-space that can be distinctly explored from other Nickel or Inconel modules. Hence, the design objective is rarely to maximize cooling effectiveness, but to maximize it within certain constraints.

Three curves are drawn in Figure 74 for three different cooling methods that have various outcomes. Method 1 and Method 2 both have the same maximum Tgw, but these maxima occur in different regions, which is a good representation of the situation between the film cooled nozzle versus the turbulated nozzle studied in this thesis. Notice that neither Method 1 nor Method 2 is able to attain the desired cooling target. It is appreciated that Method 1 has a significantly greater region that is at a much lower wall temperature than Method 2. However, since both have the same maximum value for Tgw, both would have the same estimated number of cycles to failure, which suggest that both are equally performing designs. A designer who is analyzing many vastly different designs needs comparable metrics

for different configurations that quickly assesses how well a cooling scheme succeeded in achieving the objective, even though the target was not met. This assessment is needed because the designer needs to gauge how much more effort is needed to finally accomplish the task and meet the cooling objective.

Method 3 is yet another cooling scheme that has a lower maximum Tgw, but its distribution is such that it fails to meet the cooling target in the central region and exceeds the cooling target in the outer regions. An important feature of Method 3 is that the outer regions are over-cooled. Over-cooling is generally not economical; the extra cooling does not help to achieve the cooling target and adds unnecessary cost to a design. These issues are one of the drawbacks of relying on only cooling effectiveness and performance parameters in design optimization studies. Consider an extreme case where the baseline already exceeds the cooling target everywhere. Maximizing the effectiveness further enhances the cooling, but the enhanced design is not necessary because the design target has already been met.

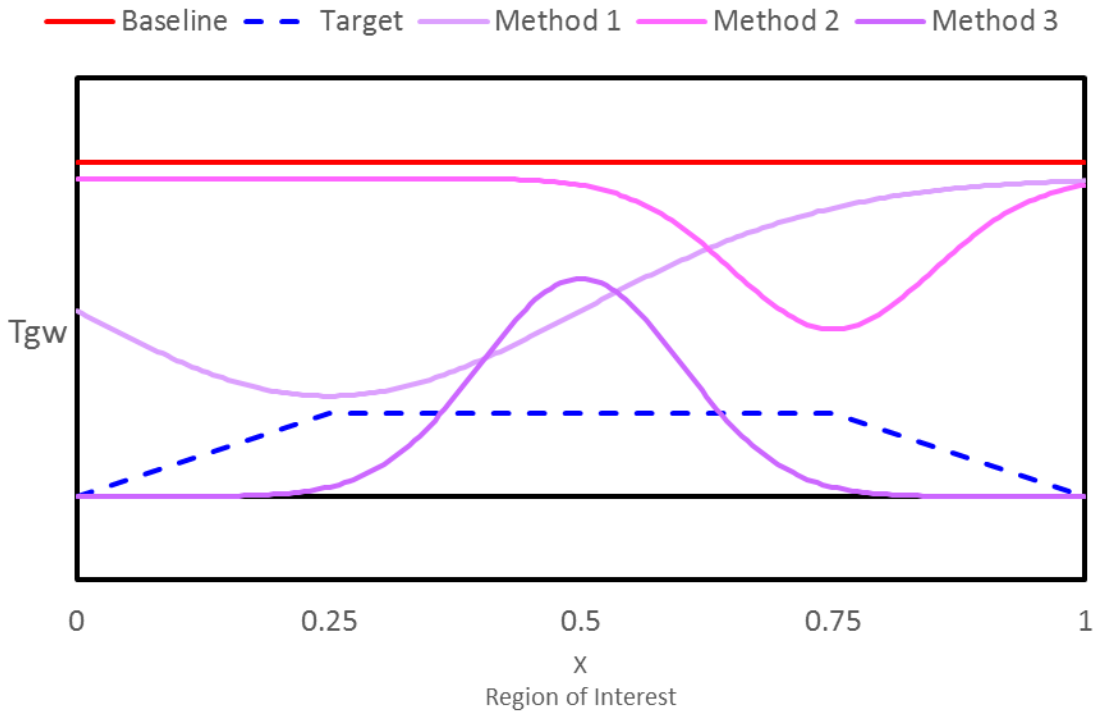

Figure 74: Example Cooling Scenario

Therefore, we define such an objective function as the local difference between the liner temperature and the original baseline temperature whenever the new liner temperature is greater than the targeted temperature (and zero when the new liner temperature is less than the targeted temperature). This definition also assumes that the baseline is greater than the target. The definition is easily amendable for situations when the baseline exceeds the target but this case is unremarkable since the design could have been left unaltered.

$$\Phi = \begin{cases} T_{gw} > T_{target} & T_{baseline} - T_{gw} \\ T_{gw} \leq T_{target} & T_{baseline} - T_{target} \end{cases} \quad (66)$$

This objective function is essentially a measure of how much the liner wall temperature has decreased from the baseline case. With this definition however, the objective function can never exceed the maximum difference between the baseline temperature and the targeted temperature (over-cooling is not measured). On the other hand, this objective function still punishes under-cooling (since the objective function becomes negative whenever the new liner temperature is worse than the baseline temperature). For the hypothetical cases plotted in Figure 74, the equivalent objective function is plotted in Figure 75. The baseline value of the objective function is the red curve (now at zero, indicating a neutral design that is no better or worse) and the maximum permissible value is plotted in the blue dashed curve. The desired cooling target should be identical to the blue dashed curve for the method to be a complete success. Keep in mind that the objective function can become negative, a completely undesirable situation.

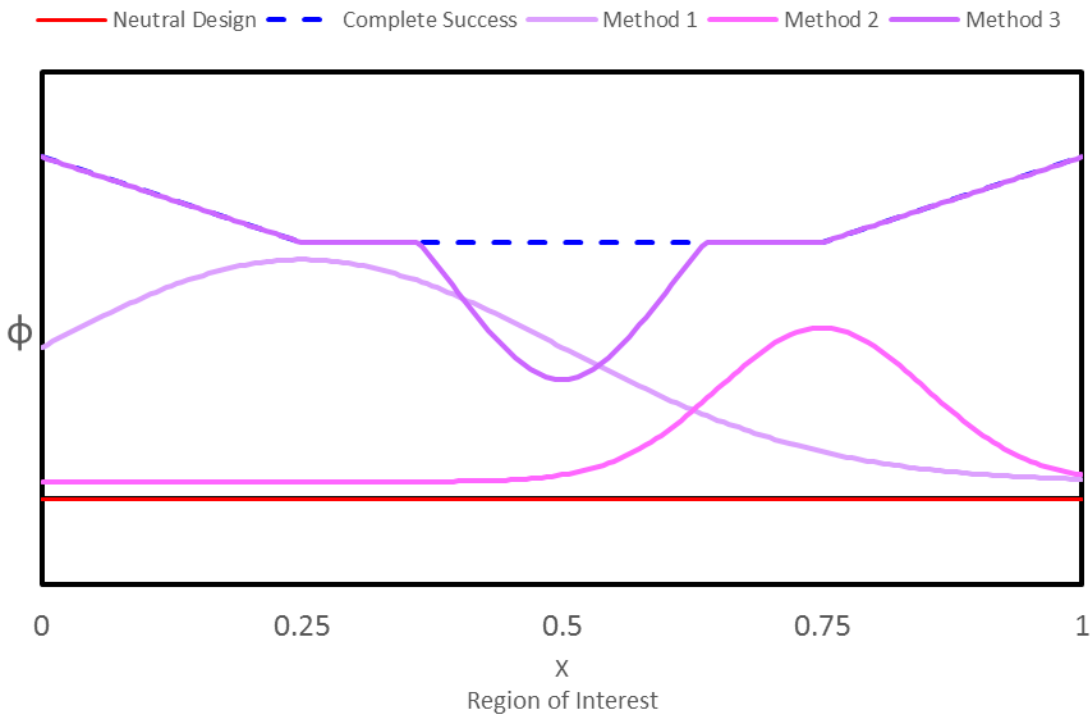

Figure 75: Cooling Objective

A utility normalization of this objective function is performed by dividing the objective function by the value that would achieve complete success, Eqn. (67). This normalized successiveness function is akin to effectiveness in film cooling. The successiveness for same cases are plotted in Figure 76.

$$\Sigma = \frac{\phi}{\phi_{max}} = \frac{\phi}{T_{baseline} - T_{target}} \tag{67}$$

The successiveness is unity ($\Sigma = 1$) when the cooling target has been met, and zero when the cooling is as-good as the baseline case ($\Sigma = 0$).

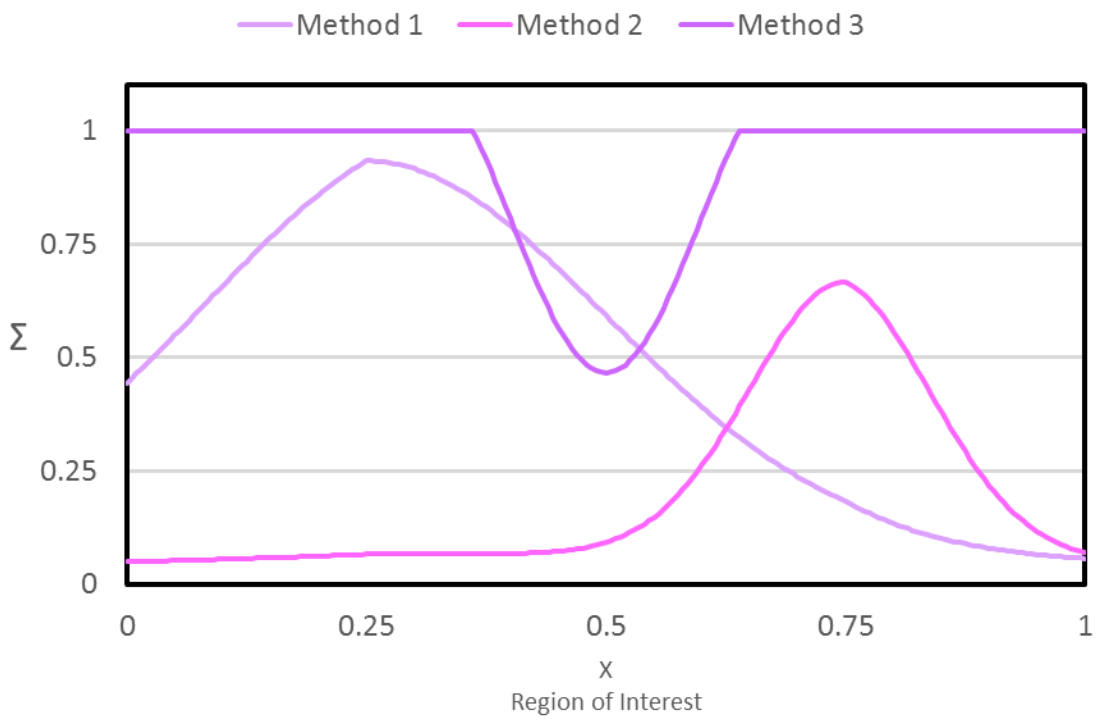

Figure 76: Example Cooling Successiveness

For Method 1, the objective function is greatest for X<0.5, is generally greater than Method 2, but is not able to reach the cooling target (does not attain a successiveness of 1). Method 3 on the other hand, succeeds in achieving the cooling target for X<0.36 and X>0.64. Thus, a designer who is analyzing these configurations is able to assess that the region where targeted cooling effort needs to be applied is in the region from 0.36<X<0.64 for Method 3. In the context of this thesis, turbulators could be applied to only this region as a possible remedy, not requiring a reconfiguration of the overall cooling schemes. More work is needed however, for Method 1 and Method 2.

The successiveness can be integrated over a region (either along a curve as in the figures, or over a surface area). When considering cooling success, the desire is not to assess the average success rate (because that would ignore the cooling target). Since Σ has a maximum value of 1; the maximum possible integrated Σ is simply the area of the region of interest. Hence, the integral of successiveness should be normalized by the area of the region, Eqn. (67)(67), which has the form of an area-averaged Σ.

$$\bar{\bar{\Sigma}} = \frac{1}{S}\iint_{S} \Sigma dS \tag{68}$$

When the cooling target has been completely achieved, $\bar{\bar{\Sigma}} = 1$; otherwise, $\bar{\bar{\Sigma}} < 1$. Unlike an averaged film cooling effectiveness (which does not indicate how well the cooling meets an objective), the complete success criteria is intuitive for the successiveness.

Successiveness Results

The newly introduced area-averaged successiveness was calculated for all the configurations studied over the region of interest (-2.75in<X<0in). The successiveness for configurations without any film cooling are tabulated in Table 19. These configurations include the baseline configuration with 100 high aspect ratio cooling channels, the configuration with half the channels removed, and the configuration with 100 cooling channels with the added turbulators.

The successiveness for configurations with film cooling are tabulated in Table 20. The only configurations with film cooling are with 50 channels without turbulators and 50 channels

with turbulators. Recall however, that blowing ratio and coolant flowrate sweeps were performed while determining which blowing ratio was most effective for film cooling.

For the baseline configuration, the successiveness is 0 for the baseline case when the per channel flowrate is 0.023 kg/s. When the channel flow is reduced, the coolant performance degrades (Tgw increases) and the successiveness is negative. As the channel flow is reduced further, the successiveness becomes increasingly negative.

For the 50 channel configuration, the successiveness is always negative because these cases were always inferior to the 100 channels. At the same total coolant flowrate (or per channel flow of 0.046 kg/s for the 50 channel configuration), the successiveness is only slightly negative (-0.08) because the performance is most similar to the original baseline case.

When turbulators are applied, the successiveness is positive for the per channel flow rate of 0.023kg/s. The successiveness becomes positive as the turbulators have superior cooling to the baseline non-turbulated cases. Even at a per channel flowrate of 0.020125kg/s, the turbulated case still has enhanced cooling compared to the baseline case (the successiveness is 0.48). When the coolant flow is reduced to 0.01725kg/s, the successiveness is negative, indicating that the turbulated case with reduced coolant flowrate is no longer adequate. At 0.023kg/s, the successiveness is 0.88. The successiveness is less than 1.00 because the maximum Tgw is not reduced to less than the target of 613K everywhere. However, a designer can look at the successiveness and quickly determine that roughly 88% of task has been achieved. The designer can the examine the detailed temperature profile for these cases to determine which regions need additional cooling and how much.

Table 19: Successiveness for Configurations Without Film Cooling

	Coolant Flowrate (kg/s)	**Max T_{gw} (K)**	**Nf (cycles)**	$\overline{\overline{\Sigma}}$
100CC	0.023	680	586	0
	0.020125	701	504	-5.04
	0.01725	727	423	-11.31
	0.014375	758	345	-19.24
	0.0115	820	234	-29.39
50CC	0.046	684	568	-0.08
	0.04025	699	513	-3.50
	0.0345	738	394	-13.46
	0.02875	779	302	-23.37
	0.023	868	178	-36.58
100CCT	0.023	626	876	0.88
	0.020125	643	770	0.48
	0.01725	670	631	-0.48
	0.014375	695	528	-2.97
	0.0115	731	410	-7.48

For the configurations with film cooling but not turbulators, the successiveness was negative for all cases except when the blowing ratio was 1. The reason for this occurrence of course, is that the blowing ratio was first varied to determine the best blowing ratio. Only after deciding on the best blowing ratio was the channel flow rate increased to match the baseline cooling performance. For the case with a blowing ratio of 1 and channel flow rate of 0.02875kg/s, the liner wall temperature was marginally lower than the baseline case in most areas. However, there was a small area near what the film was injected where the liner temperature was worse than the baseline case. Hence, although the maximum Tgw for the 0.02875kg/s case was better than the baseline, the successiveness was negative. The current definition of successiveness severely punishes designs that perform worse than the baseline case when the baseline is nearly at the cooling target. In other words, the successiveness becomes strongly negative when the performance is worse in any regions that did not need much improvement to achieve the cooling target. The reason for this severity is inherent in Eqn. (67), division by a small difference amplifies the resulting penalty. The successiveness was constructed in this fashion to make designs robust (to avoid marginal cases that carry a high risk). If designers are seeking a more forgiving criterion, it requires reformulating Eqn. (67). Alternatively, the cooling target can be made stricter in the problematic regions. This approach seems to be more sensible, since an improved cooling method is usually evaluated in terms of temperature differences. Yet another solution is contract the region of interest to only the regions where the baseline does not need to be improved.

When the channel flow had to be increased to 0.0345 kg/s for the film cooled nozzle, the wall temperatures were better than the baseline case nearly everywhere, so that there was not the same penalty that occurred for the 0.02875 kg/s case. Hence, the successiveness for the 0.0345 kg/s case is not only positive, but also much closer to unity (0.94).

When turbulators are combined with the film cooled nozzle, the successiveness is nearly unity for all cases (0.97 for the 0.023 kg/s flow-rate). The high successiveness is a strong indicator that the cooling target is nearly satisfied everywhere, which is indeed the case when one examines the detailed temperature distributions. An important feature however, is that the highest successiveness is 0.99 and does not exceed one. For flow rates of 0.02875 kg/s and greater, the maximum Tgw was less than the targeted 613 K. The nozzle is overcooled for these higher flow-rates. The successiveness was carefully designed to not give any weight to over-cooling so that the successiveness does not exceed 1. In this way, designers can quickly avoid spending effort to further improve these configurations since the metering metric, the successiveness, does not measure it at all.

Hence, it has been demonstrated by example how a combination of Tgw and successiveness may be used to rapidly compare and evaluate the performance of various cooling configurations without having to resort to a detailed discrimination of the local temperature distributions for all the cases.

Table 20: Successiveness for Configurations With Film Cooling

Configuration			Film Flowrate (kg/s)	Blowing Ratio	Coolant Flowrate (kg/s)	Max T_{gw} (K)	Nf (cycles)	$\overline{\overline{\Sigma}}$
50CCF	Blowing Ratio	Variations of	0.0001	0.053	0.023	832	219	-21.04
			0.00019	0.1	0.023	822	232	-16.46
			0.00038	0.2	0.023	804	259	-12.10
			0.00095	0.5	0.023	767	326	-11.53
			0.0019	1	0.023	713	466	-7.66
			0.00275	1.435	0.023	753	357	-11.53
			0.00285	1.5	0.023	759	342	-12.10
			0.0038	2	0.023	808	252	-16.46
			0.0055	2.89	0.023	876	170	-22.41
	Coolant Flow Rate	Variations of	0.0019	1	0.02875	668	639	-0.79
			0.0019	1	0.0345	638	798	0.94
			0.0019	1	0.0403	613	971	0.99
			0.0019	1	0.046	593	1145	0.99
50CCFT	Coolant Flow Rate	Variations of	0.0019	1	0.023	630	849	0.97
			0.0019	1	0.02875	592	1149	0.99
			0.0019	1	0.0345	573	1371	0.99
			0.0019	1	0.04025	555	1572	0.99
			0.0019	1	0.046	543	1761	0.99

Possible Future Work

Each design has its own merits with respect to overall flow rate, per channel flow rate, pressure drop, and cooling effectiveness. None of the cases are the optimal case; the best case overall depends on the needs of the rocket engine design in question. While the combined film and regenerative cooling proved to increase cooling effectiveness with decreased total flow rate, it came at a cost with an increase in pressure drop to 3.04MPa. Overall, the results show that film cooling combined with regenerative cooling in a thrust chamber is possible and effective, and improvements can be made based on optimization and the addition of other cooling methods such as turbulators.

Further improvements can be made to the designs proposed, as it is not an optimal design. In this thesis, the cooling channels were left unaltered in order to have a direct comparison with the baseline case. With the current design, the 50CCF design may not be the optimal design, even when including discrete film cooling. Optimizing the cooling channel geometry that would be used with combined regenerative and film cooling could further increase the effectiveness of the regenerative cooling and therefore reduce the amount of coolant needed, bringing pressure drop down to more favorable levels. Cooling channels can be further improved past the high aspect ratio geometry. For example, the inclusion of bifurcated or stepped channels would also increase cooling effectiveness. Bifurcated or stepped channels are normally located at the throat of the nozzle to enhance cooling effectiveness at the highest hot gas-side wall temperatures experienced by the nozzle. These advanced regenerative cooling designs could be combinable with the proposed film cooling design, as the film cooling holes

are located upstream of where bifurcated or stepped channels normally exist. This combined design should be verified and tested.

As demonstrated in this thesis, the inclusion of turbulators within the regenerative cooling channels can increase the cooling channel effectiveness. Turbulators do not interfere with the film cooling hole placement and are also compatible with a stepped or bifurcated channel design. Optimizing the turbulator design would be a useful avenue to pursue (determining the optimal relative pitch and turbulator heights that maximizes the heat transfer with the least pressure drop penalty). Since this thesis showed that combining turbulated cooling channels with discrete film cooling holes is possible, optimizing this combined design is another possibility. The sole work of Hossain et al. [68] placed orthogonal ribs on the bottom wall of the cooling channel closest to the liner. There is potential for further work in implementing rib turbulators along other walls of the cooling channel, and improving the design of such turbulators. It has already been demonstrated and is widely known that angled ribs have superior performance to orthogonal ribs. It is also important to note that turbulating the coolant in channels increases the pressure drop across the channel, so in order to combat this it may be necessary to alter the geometry of the cooling channels in order to optimize the geometry for reduced pressure drop. Possible ways to do this include increasing the size of the cooling channels at the throat. For a long fin with a constant cross-sectional area and an adiabatic tip, the fin effectiveness is described by Eqn. (69), and fin effectiveness is given by Eqn. (70). The characteristic parameter m is defined in Eqn. (71). Widening the coolant channel decreases the cross-sectional area of the fin and increases the fin efficiency as well as reducing

pressure drop. With added turbulators, the heat transfer coefficient would increase which would in turn increase the fin efficiency of the landwidths between channels.

$$\varepsilon_f = \sqrt{\frac{kP}{hA_c}} \tag{69}$$

$$\eta_f = \frac{\tanh mL}{mL} \tag{70}$$

$$m^2 = \frac{hP}{kA_c} \tag{71}$$

The film holes themselves could be optimized to produce better film cooling effectiveness. The discrete film hole design used in this thesis is not optimized for a rocket nozzle; while it does use several factors that improve the design with respect to a conventional, non-optimized design (such as inclined film holes and a blowing ratio that yields maximum film cooling effectiveness), there is still significant potential in optimization of both the geometry and flow characteristics. There is increased interest in shaped film holes, or film holes that are not cylindrical. Nguyen et al. [69] investigated the change in cooling effectiveness between cylindrical and conical-shaped film cooling holes. Conical holes have an increasing radius up to injection into the mainstream flow. This geometry increases film cooling effectiveness, as the coolant flow is able to inject into the flow at an angle closer to the hot gas-side wall plane, increasing uniformity of the film itself and keeping the film close to the hot gas-side wall. Nguyen et al. found that these conical-shaped film holes increase cooling effectiveness significantly. Since conical film holes are commonly seen as a product of the manufacturing technique used for discrete film holes, this sort of geometry could be implemented in a rocket

nozzle relatively easily. Further work should look into the effects of shaped film holes in a thrust chamber environment.

Film hole geometry can also be improved using anti-vortex film cooling designs. These film cooling designs combat the counter-rotating vortexes that can form at high blowing ratios, which decrease film effectiveness since they mix hot gases with the coolant. Repko et al. [70] investigated the effects of mainstream turbulence on the anti-vortex film hole design using CFD and found that an increase in the turbulence intensity affects the film effectiveness in a positive manner, while the turbulent length scale has little to no effect on the film effectiveness. Anti-cortex film cooling designs may be beneficial for film cooling designs in rocket nozzles, since the current work showed that a blowing ratio of 1 is most effective in cooling, which is a relatively high blowing ratio.

This thesis looks into including only one row of film cooling. Multi-row film cooling has proven to be effective in other environments such as turbomachinery. Mayle and Camarata [71] assessed the film effectiveness of multi-hole film cooling while varying pitch/diameter ratios and blowing ratios. Multiple rows of film cooling are staggered so that two film holes do not cover the same area. This will in turn increase film effectiveness as there is then a larger surface effected by a larger amount of film holes, however the interaction between different film hole jets is more pronounced. Ligrani et al. [72, 73] investigated the effects of full-coverage film cooling. Film coverage film cooling creates a layer of coolant by utilizing a large amount of film holes across a surface rather than just one row. Ligrani et al. varied film hole inclination angle, contraction ratio, and blowing ratio of full coverage film cooling. They also analyzed the

effects of a sparser full coverage film cooling design. Introducing multiple rows of film cooling around the circumference of the nozzle may be beneficial and should be assessed.

Finally, cooling effectiveness can be improved by utilizing thermal barrier coatings. Thermal barrier coatings can be combined with film cooling. Kistenmacher et al. [74] looked into the interaction between trench film cooling with TBC. Trench film cooling indicates that the film coolant is injected from the film hole at a surface lower than the surface being cooled. Trenches can result when applying TBC that thickens the surface being cooled, while keeping the surface at which the film coolant is injected at the original thickness. Work by Lu et al. [29] shows that trenched film holes have increased film cooling effectiveness, and so TBC are useful in both acting as a thermal barrier and increasing film effectiveness. Kistenmacher et al. [74] analyzed the difference in heat transfer characteristics for two designs: one that accounted for manufacturing imperfections and one that depicted the “ideal” setup of trench film cooling with TBC. They found that the heat transfer characteristics remain similar for both designs except at very low blowing ratios.

GRID CONVERGENCE STUDY

Numerical uncertainty for computational fluid dynamics simulations is best articulated through a grid convergence study. Patrick Roache articulated methods of error estimation and uncertainty calculations for numerical solutions. The grid convergence index (GCI) is a 2nd-order method that measures uncertainty by monitoring the change in a specific quantity after changing the cell density in a simulation. If the solution of the quantity changes drastically, then it is implied that the solution is mesh-dependent, and therefore is not accurate [75]. The GCI is computed using the following equations:

$$h_i = \frac{1}{N_i^{\frac{1}{3}}} \tag{72}$$

$$r_{21} = \frac{h_2}{h_1} \tag{73}$$

$$\varepsilon_{21} = |\varphi_2 - \varphi_1| \tag{74}$$

$$p = \left| \ln \left| \frac{\varepsilon_{32}}{\varepsilon_{21}} \right| + \ln\left(\frac{{r_{21}}^p - 1}{{r_{32}}^p - 1}\right) \right| \tag{75}$$

$$ea_{21} = \left| \frac{\varphi_1 - \varphi_2}{\varphi_1} \right| \tag{76}$$

$$GCI_{21} = \frac{FS * ea_{21}}{{r_{21}}^p - 1} \tag{77}$$

Where h_i is calculated from the total number of cells and the dimension (which is 3 in this case). For this specific set of equations, cases 2 and 1 are considered, where the number of cells increased from case 1 to case 2. r_{21} is the refinement ratio based on h from the cell count for

the first and second case, ε_{21} is the change between 1 and 2. The variable p is iterated for the apparent order, and ea_{21} is the approximate relative error of 1 and 2. GCI is then finally calculated using a factor of safety of 1.25.

Since over 30 simulations were performed for this investigation, it was not practical to calculate a grid convergence index for every simulation. This is also unnecessary, as many of the simulations are identical save for boundary conditions. It is most important to calculate CGI for the film cooling simulation, as this is the configuration being tested. Mesh cell count was increased, with the original simulation containing the least amount of cells. The simulations were named M1, M2, M3, and M4 with respect to increasing cell count. A coarser mesh M0 was also included. The cell count and base size of each grid is listed in Table 21.

Table 21: Grid Convergence Mesh Refinement Cell Count and Base Size

Simulation	Cell Count	Base Size
M0	2,379,301	0.25in
M1	2,926,342	0.2in
M2	4,353,096	0.15in
M3	5,879,609	0.125in
M4	8,669,372	0.100in

M4 cell density is approximately 3x as dense as M1. The cell count was altered by decreasing the previous mesh base size by 0.05in. The simulations were then all run until convergence. GCI was calculated by comparing Nf; the calculated Nf are listed in Table 22 and

GCI are in Table 23. However, temperature profiles were also plotted to view the effect of cell density on the overall temperature profile, Figure 77 .

Table 22: Grid Convergence Nf Results

Configuration	Nf
M0	628
M1	798
M2	804
M3	781
M4	684

Table 23: Grid Convergence Index Results

Cell Counts Included	GCI 21	GCI 32
M3, M2, M1	5.1762%	0.0179%
M4, M2, M1	3.7944%	0.0195%

The grid convergence index reaches a maximum of approximately 5%, meaning that the error of the results dependent on the mesh is estimated to be 5%. This number is relatively small, but should be taken into account when assessing the accuracy of these results. Looking at Figure 77, it is apparent that the temperature profile trends in each simulation are relatively the same; however, there is variation in terms of the temperatures as quantities.

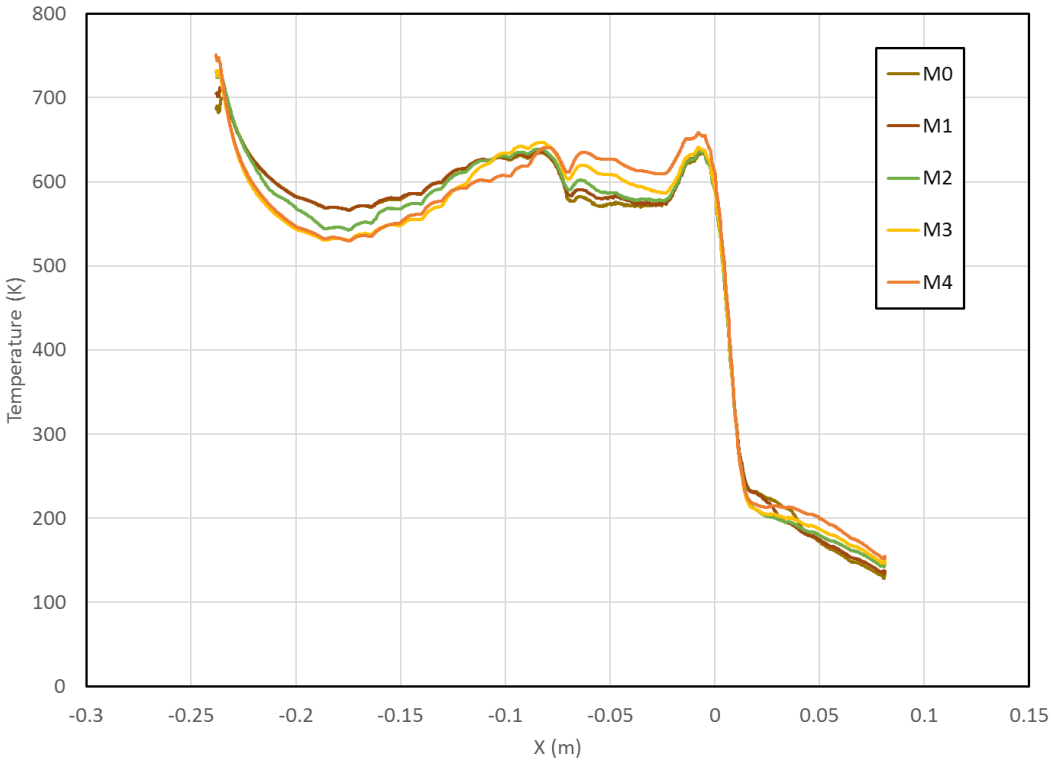

Figure 77: Liner Wall Temperature Distribution with Cell Refinement Comparison

This shows that the error using Nf vs the variation in temperature profile trends are different, yet since Nf is the factor used to determine the effectiveness of each cooling configuration, the overall mesh dependence is relatively low.

CONCLUSIONS

In this thesis, several configurations were tested in order to determine the effectiveness of combined internal and film cooling. Results were based on the change in maximum hot gas side wall temperature from the baseline. Max hot gas side wall temperature can be used to estimate number of cycles to failure. It was shown that at certain film blowing ratios and channel mass flow rates, combined regenerative and film cooling can increase the life of the nozzle. The best case design with a blowing ratio of 1.9e-4 and a total mass flow rate of 1.82kg/s showed an increase in estimated Nf from 586 to 798, and a reduction in maximum Tgw from 680K to 638K. When adding turbulators to the cooling channels, there was significant improvement to the cooling performance. Combining film cooling with turbulated cooling channels reduced Tgw below the target temperature of 613K at certain channel mass flow rates. This improvement in cooling effectiveness, however, comes with significant consequences. There is an increase in pumping power needed for increasing the per channel mass flow rate, which is represented by the increase in pressure drop for designs that required an increase in per channel coolant flow rate.

This thesis showed that it is feasible to model a rocket nozzle with more than one cooling channel in 3-dimensional space, something that was previously asserted as too difficult or computationally expensive to use for analysis. Using this design could improve CFD analysis for many axisymmetric designs that require a 3D space for accurate results. This thesis is focused on feasibility, and optimization of the cooling configurations presented is possible and provides many avenues of improvement for these designs.

REFERENCES

[1] G. P. Sutton, "History of Liquid Propellant Rocket Engines in the United States," *Journal of Propulsion and Power,* vol. 19, pp. 978-1007, 2003/11/01 2003.

[2] F. Steven and R. Shamim, *Remembering the Giants: Apollo Rocket Propulsion Development*: NASA History Division, 2009.

[3] D. H. Huang and D. K. Huzel, "Design of Liquid Propellant Rocket Engines," NASA, Washington, DC NASA-SP-125, Jan 01, 1971 1971.

[4] G. V. R. Rao, "Exhaust Nozzle Contour for Optimum Thrust," *Journal of Jet Propulsion,* vol. 28, pp. 377-382, 1958/06/01 1958.

[5] E. M. Landsbaum, "Contour Nozzles," *ARS Journal,* vol. 30, pp. 244-250, 1960/03/01 1960.

[6] R. Stark and C. Génin, "Experimental Study on Rocket Nozzle Side Load Reduction," *Journal of Propulsion and Power,* vol. 28, pp. 307-311, 2012/03/01 2012.

[7] S. B. Verma, R. Stark, and O. Haidn, "Effect of Ambient Pressure Fluctuations on Dual-Bell Transition Behavior," *Journal of Propulsion and Power,* vol. 30, pp. 1192-1198, 2014/09/01 2014.

[8] C. Génin and R. Stark, "Side Loads in Subscale Dual Bell Nozzles," *Journal of Propulsion and Power,* vol. 27, pp. 828-837, 2011/07/01 2011.

[9] C. Génin, A. Gernoth, and R. Stark, "Experimental and Numerical Study of Heat Flux in Dual Bell Nozzles," *Journal of Propulsion and Power,* vol. 29, pp. 21-26, 2013/01/01 2012.

[10] S. Dirk, G. Chloe, K. Sebastian, and H. Volker, "A Numerical Model for Nozzle Flow Application under LOX/CH4 Hot Flow Conditions," in *52nd AIAA/SAE/ASEE Joint Propulsion Conference*, ed: American Institute of Aeronautics and Astronautics, 2016.

[11] H. S. Ralf and G. Chloe, "Scaling Effects on Side Load Generation in Subscale Rocket Nozzles," in *52nd AIAA/SAE/ASEE Joint Propulsion Conference*, ed: American Institute of Aeronautics and Astronautics, 2016.

[12] K. Davis, E. Fortner, M. Heard, H. McCallum, and H. Putzke, "Experimental and Computational Investigation of a Dual-Bell Nozzle," in *53rd AIAA Aerospace Sciences Meeting*, ed: American Institute of Aeronautics and Astronautics, 2015.

[13] R. Stark and C. Génin, "Hot Flow Testing of a Film Cooled Dual Bell Nozzle," in *47th AIAA/ASME/SAE/ASEE Joint Propulsion Conference & Exhibit*, ed: American Institute of Aeronautics and Astronautics, 2011.

[14] C. Nürnberger-Génin and R. Stark, "Experimental Study on Flow Transition in Dual Bell Nozzles," *Journal of Propulsion and Power,* vol. 26, pp. 497-502, 2010/05/01 2010.

[15] S. B. Verma, R. Stark, and O. Haidn, "Reynolds Number Influence on Dual-Bell Transition Phenomena," *Journal of Propulsion and Power,* vol. 29, pp. 602-609, 2013/05/01 2013.

[16] M. F. Wadel, "Comparison of High Aspect Ratio Cooling Channel Designs for a Rocket Combustion Chamber With Development of an Optimized Design," Lewis Research Center, Cleveland, Ohio, NASA TM 1998-206313, 1998.

[17] Q. R, "Experimental fatigue life investigation of cylindrical thrust chambers," in *13th Propulsion Conference*, ed: American Institute of Aeronautics and Astronautics, 1977.

[18] R. Bilstein, *Stages to Saturn: A Technological History of the Apollo/Saturn Launch Vehicle*: DIANE Publishing, 1999.

[19] G. S. Gill and W. H. Nurick, "Liquid rocket engine injectors," Mar 01, 1976 1976.

[20] Y.-D. Kang and B. Sun, "Numerical Simulation of Liquid Rocket Engine Thrust Chamber Regenerative Cooling," *Journal of Thermophysics and Heat Transfer,* vol. 25, pp. 155-164, 2011.

[21] V. G. Bazarov and V. Yang, "Liquid-Propellant Rocket Engine Injector Dynamics," *Journal of Propulsion and Power,* vol. 14, pp. 797-806, 1998/09/01 1998.

[22] M. P. Burke, M. Chaos, Y. Ju, F. L. Dryer, and S. J. Klippenstein, "Comprehensive H2/O2 kinetic model for high-pressure combustion," *International Journal of Chemical Kinetics,* vol. 44, pp. 444-474, 2012.

[23] J. Li, Z. Zhao, A. Kazakov, and F. L. Dryer, "An updated comprehensive kinetic model of hydrogen combustion," *International Journal of Chemical Kinetics,* vol. 36, pp. 566-575, 2004.

[24] N. A. Amato, J. C. Leylegian, and M. H. Naraghi, "CFD Analysis of Film Cooling and Heat Transfer in a Bipropellant Rocket Nozzle, Incorporating Chemically Reacting Flow," in *52nd AIAA/SAE/ASEE Joint Propulsion Conference*, ed: American Institute of Aeronautics and Astronautics, 2016.

[25] C. D. Coulbert, "Selecting cooling techniques for liquid rockets for spacecraft," *Journal of Spacecraft and Rockets,* vol. 1, pp. 129-139, 1964/03/01 1964.

[26] M. F. Taylor, "Heat-transfer predictions in the cooling passages of nuclear rocket nozzles," *Journal of Spacecraft and Rockets,* vol. 5, pp. 1353-1355, 1968/11/01 1968.

[27] H. G. Price, "Cooling of High-Pressure Rocket Thrust Chambers with Liquid Oxygen," *Journal of Spacecraft and Rockets,* vol. 18, pp. 338-343, 1981/07/01 1981.

[28] M. F. Wadel, R. J. Quentmeyer, and M. L. Meyer, "A Rocket Engine Design for Validating the High Aspect Ratio Cooling Channel Concept," *Advanced earth-to orbit propulsion technology,* vol. 2, pp. 145-150, 1994.

[29] Y. Lu, A. Dhungel, S. V. Ekkad, and R. S. Bunker, "Effect of Trench Width and Depth on Film Cooling From Cylindrical Holes Embedded in Trenches," *Journal of Turbomachinery,* vol. 131, pp. 011003-011003, 2008.

[30] R. Quentmeyer, H. Kasper, and J. Kazaroff, "Investigation of the effect of ceramic coatings on rocket thrust chamber life," in *14th Joint Propulsion Conference*, ed: American Institute of Aeronautics and Astronautics, 1978.

[31] A. Bucchi, C. Bruno, and A. Congiunti, "Transpiration Cooling Performance in LOX/Methane Liquid-Fuel Rocket Engines," *Journal of Spacecraft and Rockets,* vol. 42, pp. 476-486, 2005/05/01 2005.

[32] M. J. Brunner, "Active cooling heat protection," *Journal of Spacecraft and Rockets,* vol. 6, pp. 661-666, 1969/06/01 1969.

[33] R. J. Goldstein, E. R. G. Eckert, and J. W. Ramsey, "Film Cooling With Injection Through Holes: Adiabatic Wall Temperatures Downstream of a Circular Hole," *Journal of Engineering for Power,* vol. 90, pp. 384-393, 1968.

[34] S. Park, E. Y. Jung, S. H. Kim, H.-S. Sohn, and H. H. Cho, "Enhancement of Film Cooling Effectiveness Using Backward Injection Holes," in *ASME Turbo Expo 2015: Turbine Technical Conference and Exposition*, Montreal, Quebec, Canada, 2015, p. V05BT12A047.

[35] R. J. Goldstein, E. R. G. Eckert, and D. J. Wilson, "Film Cooling With Normal Injection Into a Supersonic Flow," *Journal of Engineering for Industry,* vol. 90, pp. 584-588, 1968.

[36] M. Hombsch and H. Olivier, "Film Cooling in Laminar and Turbulent Supersonic Flows," *Journal of Spacecraft and Rockets,* vol. 50, pp. 742-753, 2013/07/01 2013.

[37] R. Arnold, D. Suslov, and O. J. Haidn, "Film Cooling of Accelerated Flow in a Subscale Combustion Chamber," *Journal of Propulsion and Power,* vol. 25, pp. 443-451, 2009/03/01 2009.

[38] R. Arnold, D. Suslov, and O. Haidn, "Circumferential Film Cooling Effectiveness in a LOX/H2 Subscale Combustion Chamber," *Journal of Propulsion and Power,* vol. 25, pp. 760-770, 2009/05/01 2009.

[39] R. S. Bunker and J. C. Bailey, "Film Cooling Discharge Coefficient Measurements in a Turbulated Passage With Internal Crossflow," *Journal of Turbomachinery,* vol. 123, pp. 774-780, 2001.

[40] D. F. Dipprey and R. H. Sabersky, "Heat and momentum transfer in smooth and rough tubes at various prandtl numbers," *International Journal of Heat and Mass Transfer,* vol. 6, pp. 329-353, 1963.

[41] J. C. Han, L. R. Glicksman, and W. M. Rohsenow, "An investigation of heat transfer and friction for rib-roughened surfaces," *International Journal of Heat and Mass Transfer,* vol. 21, pp. 1143-1156, 8// 1978.

[42] R. L. Webb, E. R. G. Eckert, and R. J. Goldstein, "Heat transfer and friction in tubes with repeated-rib roughness," *International Journal of Heat and Mass Transfer,* vol. 14, pp. 601-617, 4// 1971.

[43] R. L. Webb, E. R. G. Eckert, and R. J. Goldstein, "Generalized heat transfer and friction correlations for tubes with repeated-rib roughness," *International Journal of Heat and Mass Transfer,* vol. 15, pp. 180-184, 1// 1972.

[44] D. L. Gee and R. L. Webb, "Forced convection heat transfer in helically rib-roughened tubes," *International Journal of Heat and Mass Transfer,* vol. 23, pp. 1127-1136, 8// 1980.

[45] P. R. Chandra, C. R. Alexander, and J. C. Han, "Heat Transfer and Friction Behaviors in Rectangular Channels with Varying numbers of Ribbed Walls," *International Journal of Heat and Mass Transfer,* vol. 46, pp. 481-495, 2003.

[46] A. P. Rallabandi, H. Yang, and J.-C. Han, "Heat Transfer and Pressure Drop Correlations for Square Channels With 45 Deg Ribs at High Reynolds Numbers," *Journal of Heat Transfer,* vol. 131, pp. 071703-071703, 2009.

[47] J. C. Han, "Heat Transfer and Friction in Channels With Two Opposite Rib-Roughened Walls," *Journal of Heat Transfer,* vol. 106, pp. 774-781, 1984.

[48] J. Nikuradse, *Laws of flow in rough pipes*, 1933.

[49] Jahed Hossain, Lucky V. Tran, C. Cassandra, V. Shashi, and J. S. Kapat, "Numerical Study of Enhancement of Regenerative Cooling Using Ribs," presented at the 49th AIAA/ASME/SAE/ASEE Joint Propulsion Conference, 2013.

[50] B. Kendall, S. Dave, and W. Gordon, "A regeneratively cooled thrust chamber for the Fastrac engine," in *36th AIAA/ASME/SAE/ASEE Joint Propulsion Conference and Exhibit*, ed: American Institute of Aeronautics and Astronautics, 2000.

[51] W. Mary and M. Michael, "Validation of high aspect ratio cooling in a 89 kN (20,000 lbf) thrust combustion chamber," in *32nd Joint Propulsion Conference and Exhibit*, ed: American Institute of Aeronautics and Astronautics, 1996.

[52] P. Richard, "The many facets of the RL10 liquid rocket engine - A continuing success story," in *34th AIAA/ASME/SAE/ASEE Joint Propulsion Conference and Exhibit*, ed: American Institute of Aeronautics and Astronautics, 1998.

[53] P. Marco, N. Francesco, and O. Marcello, "Quasi-2D Modeling of High-Aspect-Ratio-Cooling-Channel Flows," in *49th AIAA/ASME/SAE/ASEE Joint Propulsion Conference*, ed: American Institute of Aeronautics and Astronautics, 2013.

[54] M. Pizzarelli, F. Nasuti, and M. Onofri, "Trade-off analysis of high-aspect-ratio-cooling-channels for rocket engines," *International Journal of Heat and Fluid Flow,* vol. 44, pp. 458-467, 12// 2013.

[55] P. Weihing, B. A. Younis, and B. Weigand, "Heat transfer enhancement in a ribbed channel: Development of turbulence closures," *International Journal of Heat and Mass Transfer,* vol. 76, pp. 509-522, 9// 2014.

[56] C. C. Clickner, J. W. Ekin, N. Cheggour, C. L. H. Thieme, Y. Qiao, Y. Y. Xie*, et al.*, "Mechanical properties of pure Ni and Ni-alloy substrate materials for Y–Ba–Cu–O coated superconductors," *Cryogenics,* vol. 46, pp. 432-438, 6// 2006.

[57] M. Lauer, M. Zellhuber, T. Sattelmayer, and C. J. Aul, "Determination of the Heat Release Distribution in Turbulent Flames by a Model Based Correction of OH* Chemiluminescence," *Journal of Engineering for Gas Turbines and Power,* vol. 133, pp. 121501-121501, 2011.

[58] M. Lauer and T. Sattelmayer, "On the Adequacy of Chemiluminescence as a Measure for Heat Release in Turbulent Flames With Mixture Gradients," *Journal of Engineering for Gas Turbines and Power,* vol. 132, pp. 061502-061502, 2010.

[59] M. Rajagopal, "Numerical Modeling of Regenerative Cooling System for Large Expansion Ratio Rocket Engines," *Journal of Thermal Science and Engineering Applications,* vol. 7, pp. 011012-011012, 2015.

[60] S. Baldauf, M. Scheurlen, A. Schulz, and S. Wittig, "Correlation of Film-Cooling Effectiveness From Thermographic Measurements at Enginelike Conditions," *Journal of Turbomachinery,* vol. 124, pp. 686-698, 2002.

[61] S. M. Salim and S. C. Cheah, "Wall y+ Strategy for Dealing with Wall-bounded Turbulent Flows," in *International MultiConference of Engineers and Computer Scientists*, Hong Kong, 2009.

[62] M. Wolfshtein, "The velocity and temperature distribution in one-dimensional flow with turbulence augmentation and pressure gradient," *International Journal of Heat and Mass Transfer,* vol. 12, pp. 301-318, 1969/03/01 1969.

[63] T. Jongen, "Simulation and modeling of turbulent incompressible fluid flows," EPFL, 1998.

[64] L. V. Tran, "Development of Full Surface Transient Thermochromic Liquid Crystal Technique for Internal Cooling Channels," M.S. M.S. Thesis, University of Central Florida, Orlando, FL, 2014.

[65] M. Naraghi, D. Mohr, and R. Quentmeyer, "Effect of a blocked channel on the wall temperature of a regeneratively cooled rocket thrust chamber," in *37th Joint Propulsion Conference and Exhibit*, ed: American Institute of Aeronautics and Astronautics, 2001.

[66] L. V. Tran, J. S. Kapat, A. L. Pham, Z. Little, D. , and P. K. Tran, "Heat Transfer Measurements Using the Hybrid Heat Transfer Technique With Thermally Adiabatic and Participating Ribs," in *ASME Turbo Expo 2013: Turbine Technical Conference and Exposition*, San Antonio, Texas, 2013.

[67] R. L. Webb, "Performance evaluation criteria for use of enhanced heat transfer surfaces in heat exchanger design," *International Journal of Heat and Mass Transfer,* vol. 24, pp. 715-726, 4// 1981.

[68] J. Hossain, L. V. Tran, C. Carpenter, S. B. Verma, and J. S. Kapat, "Numerical Study of Enhancement of Regenerative Cooling Using Ribs," presented at the 49th AIAA/ASME/SAE/ASEE Joint Propulsion Conference, 2013.

[69] C. Q. Nguyen, P. L. Johnson, B. C. Bernier, S. H. Ho, and J. S. Kapat, "Comparison of Film Effectiveness and Cooling Uniformity of Conical and Cylindrical-Shaped Film Hole With Coolant-

Exit Temperature Correction," *Journal of Thermal Science and Engineering Applications,* vol. 3, pp. 031011-031011, 2011.

[70] T. W. Repko, A. C. Nix, C. Uysal, and J. D. Heidmann, "Numerical Study on the Effects of Freestream Turbulence on Antivortex Film Cooling Design at High Blowing Ratio," *Journal of Thermal Science and Engineering Applications,* vol. 9, pp. 011013-011013, 2016.

[71] R. E. Mayle and F. J. Camarata, "Multihole Cooling Film Effectiveness and Heat Transfer," *Journal of Heat Transfer,* vol. 97, pp. 534-538, 1975.

[72] P. Ligrani, M. Goodro, M. Fox, and H.-K. Moon, "Full-Coverage Film Cooling: Film Effectiveness and Heat Transfer Coefficients for Dense Hole Arrays at Different Hole Angles, Contraction Ratios, and Blowing Ratios," *Journal of Heat Transfer,* vol. 135, pp. 031707-031707, 2013.

[73] P. Ligrani, M. Goodro, M. D. Fox, and H.-K. Moon, "Full-Coverage Film Cooling: Heat Transfer Coefficients and Film Effectiveness for a Sparse Hole Array at Different Blowing Ratios and Contraction Ratios," *Journal of Heat Transfer,* vol. 137, pp. 032201-032201, 2015.

[74] D. A. Kistenmacher, F. Todd Davidson, and D. G. Bogard, "Realistic Trench Film Cooling With a Thermal Barrier Coating and Deposition," *Journal of Turbomachinery,* vol. 136, pp. 091002-091002, 2014.

[75] P. J. Roache, *Fundamentals of verification and validation*: hermosa publ., 2009.